UNIVERSITAT ROVIRA I VIRGILI

Prussian blue derivatives as smart materials for technological Applications

Bárbara Rodríguez García

DOCTORAL THESIS

Prussian blue derivatives as smart materials for technological applications

Bárbara Rodríguez García

Supervised by

Dr. José Ramón Galán Mascarós

Institut Català d´Investigació Química (ICIQ)

Tarragona, July 2017

UNIVERSITAT
ROVIRA i VIRGILI

Prof. Dr. José Ramón Galán Mascarós, Group Leader of the Institute of Chemical Research of Catalonia (ICIQ) and Research Professor of the Catalan Institution for Research and Advances Studies (ICREA),

I STATE that the present study, entitled: **"Prussian blue derivatives as smart materials for technological applications"**, presented by Bárbara Rodríguez García for the award of the degree of Doctor, has been carried out under my supervision at the Institute of Chemical Research of Catalonia (ICIQ).

Tarragona, 30 March 2017

Doctoral Thesis Supervisor/s

Prof. Dr. José Ramón Galán Mascarós

The work performed in the present doctoral thesis has been possible thanks to the funding of:

A mi familia

A mi madre

*"Los científicos dicen que estamos hechos de átomos,
pero yo creo que estamos hechos de historias"*

-E. Galeano-

*"En la tierra hay suficiente para satisfacer las necesidades de todos,
pero no tanto como para satisfacer la avaricia de algunos"*

-M. Gandhi-

*"There's a crack, a crack in everything,
that's how the light gets in"*

-L. Cohen-

Acknowledgements

Y caminando, caminado, llegó el final de este largo viaje, y con él, la parte más difícil, recordar a quienes me han acompañado. Tengo tanto que agradecer y a tantas personas, que sólo espero no olvidarme de nadie.

En primer lugar, quiero dar las gracias a mi supervisor, el Prof. José Ramón Galán Mascarós, por haberme dado la oportunidad de participar en tantos proyectos estos años. He crecido muchísimo tanto personal como profesionalmente ha sido una experiencia maravillosa.

I would like to thanks Prof. Frederic Jaouen for giving me the opportunity to carry out part of my thesis in his lab during my stay at University of Montpellier. It has been one of the best experience in my life. Gracias a Álvaro por las reuniones de los jueves y los consejos. A Sonia y a Marta, por los brunches, las cañas, el cariño y por hacer que Francia no me parezca tan mala.

Gracias a mis compañeros de laboratorio, por la ayuda durante estos años. Ha sido un camino largo, pero con vosotros, se ha hecho ameno. En especial, a Franziska, genial y maravillosa, que nada ni nadie te pare. A Neus, por los consejos y el afterwork. Y a Jesús, por las risas, las conversaciones y las maestras, sin ellas la escritura habría sido mucho más dura, gracias compañero. A Xavi y León, ha sido un verdadero placer aprender cada día con vosotros, sois el alma de este centro.

Con admiración a los compañeros de Espineta, por los libros, las reflexiones y por permitirme participar en un proyecto tan maravilloso. A Sofi, llegaste casi al final, pero aun nos queda pista. A Laura y Giulia, mis cervantes favoritas, soy muy contenta de haberos conocido y espero que sigamos juntas mucho tiempo. A Paula, Lorena y Gonzalo, por los consejos entre vermús y las risas entre comidas, me habéis aportado muchísimo. A Miguel, Isra y Carmen, nada en Tarragona volvió a ser igual sin vosotros.

A Irene, por estar siempre al otro lado del Skype, por las visitas y el hospedaje estemos donde estemos, nunca me fallas, eres mi favorita. A mi clan madrileño, Kris y Clau, por aguantarme y quererme, por las horas al teléfono, por las noches de movida madrileña, y por todo lo que os quiero y os echo de menos.

A mi familia, soy muy afortunada de poder contar siempre con vuestro apoyo. A David, el mejor hermano mayor que nadie pueda tener, eres mi faro. A Guillermo y Encarnita, os echamos de menos. A mi hermano Ares, por ayudarme a no olvidar de dónde vengo. A mi abuelo Herminio, por enseñarme la ciencia más importante, la que no está en los libros. A mi padre, por enseñarme a mirar el planeta y la importancia del hacer.

Pero a quienes quiero dedicarles este trabajo con más cariño y admiración es a todas las mujeres de mi familia. Con vuestra humildad, trabajo y valentía, habéis hecho posible que sea quien soy y me habéis empujado hasta aquí, espero poder transmitir y mantener vivo vuestro legado de lucha y generosidad, sois mis heroínas. A mis abuelas, María y Aurora, vuestro ejemplo siempre me acompaña. A mi hermana, María, llegaste y se hizo la luz, mi mejor amiga y aliada, mi vida; lista y combativa, tuyo es el futuro, nunca caminarás sola. A Aurora, siempre al pie del cañón, como una madre indestructible; tu amor y tus consejos me guían en cada momento, todo esto también es tuyo. A mi madre, no pasa un solo día en el que no te eche de menos, me enseñaste a vivir con pasión y a valerme por mi misma, a ser siempre valiente; te quiero, eres parte de mí, y siempre te querré. A mi abuela Felicidad, tu nombre apenas describe el alcance de tu alegría y la maravilla de tu sonrisa, no existe nadie en el mundo con un corazón más grande que el tuyo, no sé qué habría sido de mi sin ti, luchadora incansable, ejemplo de vida y fortaleza; a ti, te lo debo todo.

A Julián, cuando menos lo esperaba, irrumpiste en mi vida. Y como un elefante que ocupa mucho espacio, la revolucionaste. Pensar, hacer, construir, leer y escribir, conversar, sentir, reír, caminar, ahora tienen mucho más sentido. Seamos realistas y hagamos, juntos, lo imposible.

Table of contents

List of Publications

List of publications related with this thesis:

- Goberna-Ferron, S.; Hernandez, W. Y.; Rodriguez-Garcia, B.; Galan-Mascaros, J. R. "*Light-driven water oxidation with metal hexacyanometallate heterogeneous catalysts*" <u>ACS catalysis,</u> **2014,** 4 1637–1641.

- Han, L.; Tang, P.; Reyes-Carmona, Á.; Rodríguez-García, B.; Torréns, M.; Morante, J. R.; Arbiol, J.; Galan-Mascaros, J. R.. "*Enhanced activity and acid pH stability of Prussian blue-type oxygen evolution electrocatalysts processed by chemical etching*" <u>Journal of the American Chemical Society</u>, **2016**, 138**,** 16037-16045.

- Promdet, P.; Rodriguez-Garcia, B.; Henry, A.; Nguyen, C.; Khuu, T.; Galan-Mascaros, J. R.; Sorasaenee, K.; "*Tuning Prussian blue coordination polymers as biocompatible contrast agents for X-ray computed tomography*" **2017**, *Submitted*

  Manuscripts in preparation:

- Rodríguez-García, B.; Reyes-Carmona, A.; Jiménez-Morales, I.; Blasco, M.; Zitolo, A.;Cavaliere,S.; Jones, D.; Galan-Mascaros, J. R.; Jaouen, J. (2017) "Cobalt hexacyanoferrate supported on Sb-doped SnO_2 a promising non-noble anode catalyst for PEM electrolyzers"

Abbreviations

ṽ	Wavenumber
ν	Vibrational frequency
χ	Magnetic susceptibility
η	Overpotencial
μ	Micro
μ-CT	Micro-computed tomography
A	Ampere
AC	Attenuation coefficient
AT	Attenuation
ATO	Antimony tin oxide
ATR	Autothermal reforming
a.u.	Arbitrary units
ChD	Circular Dichroism
ClER	Chlorine evolution reaction
CN$^-$	Cyanide ligand
CNPT	Normal condition of pressure and temperature
CV	Cycle Voltammetry
CoHFe	Cobalt hexacyanoferrate
DECT	Dual-energy computed tomography
DER	Dual-energy ratio
dien	1,2-diaminocyclohexane
DLS	Dynamic light scattering
e$^-$	Electron
E	Electric/redox potential
E˚	Standard redox potential
EDX	Electron dispersive X-ray
EIS	Electric impedance spectroscopy
Eq	Equation

eV	Electronvolt
FC	Field cold
FT	Fourier transform
FTO	Fluorine-doped tin oxide
GC	Glassy carbon electrode
h	Hours
H	Magnetic field
H$^+$	Proton
hv	Photon light
H$_C$	Coercive field
HER	Hydrogen evolution reaction
HOMO	Highest occupied molecular orbital
HS	High spin
HU	Hounsfield unit
IPB	Insoluble Prussian blue
IR	Infrared radiation
j	Current density
L	Ligand
L-pro	L isomer of proline aminoacid
LS	Low spin
LUMO	Lowest unoccupied molecular orbital
M	Magnetization or Molar
mA/cm^2	miliamper per centimeter square
MEAS	Membrane electrode assembly
min	Minute
M	Molar or metal
MJ Kg	Megajoules per kilogram
MMs	Molecular-based magnets
MnHFe	Manganese hexacyanoferrate
MnHCo	Manganese hexacyanocobaltate
MO	Molecular orbital

M_r	Remnant magnetization (hysteresis)
MRI	Magnetic resonance imaging
M_s	Magnetization at saturation
NFS	Nephrogenic systemic fibrosis
OCP	Open circuit potencial
Oe	Oersted
OER	Oxygen evolution reaction
P	Pressure
P_o	Reference pressure
PBA	Prussian blue analogue
PB	Prussian blue
PEM	Proton exchange membrane/ Polymer exchange membrane
PEMEL	Proton exchange membrane electrolysis
PEMFC	Proton exchange membrane fuel cell
pH	logaritme of proton concentration ($-\log [H^+]$)
P_i	Phosphate
POX	Partial oxidation
PW	Prussian white
PY	Prussian yellow
R	Ideal gas constant
RDE	Rotating disk electrode
RM	Remnant magnetization (as a function of temperature)
rpm	Revolutions per minute
s	Second
SEM	Scanning electron microscopy
SOEC	Solid oxide electrolyzer cell
SQUID	Superconducting quantum interference device
SR	Steam reforming
TBA	Tetrabutilamonium
T_c	Curie / Critical temperature
TEM	Transmission electron microscopy

TGA	Thermogravimetry analisys
TM	Transition metal
TMOS	Tetramethyl orthosilicate
T$_n$	Neel Temperature
U87-Luc	Glioblastoma U87 cancer cell
Uv-vis	Ultraviolet visible light
V	Volt
VCD	Vibrational circular dichroism
VHCr	Vanadium hexacyanochromate
WE	Water electrolysis
WOC	Water oxidation catalyst
XCA	X-ray contrast agent
XRD	X-ray diffraction
ZFC-FC	Zero-field cold / Field-cold

General Introduction

Chapter 1

1.1   The nature of the cyanide ligand

The study of coordination chemistry is essential for the research and development of novel, advanced materials. As a brief definition, this area of research aims at investigating compounds in which ligands are linked to a central ion, generally a transition metal. The nature of the ligand plays a crucial role in this field, as it influences the electronic structure and, therefore, physico-chemical properties and the applicability of the compound. It is also a powerful tool to design new materials through preparation and combination of a huge variety of building blocks, which can be chosen to tune and rationally design multifunctional materials.

In this sense, cyanide rises as one the most powerful ligands to build up new materials by a bottom-up synthetic approach, taking advantage of the intrinsic properties of the molecular building blocks. The cyanide ligand is characterized by a strong triple bond between the carbon and the nitrogen atom. The negatively charged CN^- anion is the conjugate base of hydrogen cyanide (HCN) and its molecular energy levels can be seen in Figure 1.1.1.
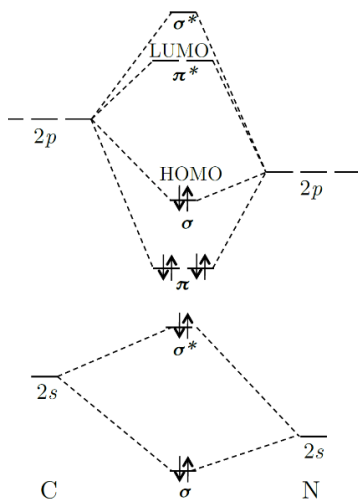
Figure 1.1.1 *Cyanide anion molecular orbitals.*

In the cyanide bond, the $2s$ orbitals, as well as the $2p_z$ orbitals, of both C and N, hybridize and form bonding (σ) and antibonding (σ^*) sigma orbitals along the CN axis, while the two orthogonal $2p_x$ and $2p_y$ orbitals contribute to π bonding. Hence, the resulting electronic configuration of cyanide anion is, according to Molecular Orbital (MO) theory:

$$(\sigma 1s)^2(\sigma^*1s)^2(\sigma 2s)^2(\sigma^*2s)^2(\sigma 2px)^2(\pi 2py)^2(\pi 2pz)^2$$
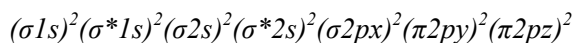
In the Lewis structure representation, as in Figure 1.1.2., the triple bond is represented as simply three lines, corresponding to the σ bond, and the two π-bonds. The electron lone pair, which is mainly localized on the nitrogen non-bonding sp orbital, represented by two dots. The nature of the strong, electron rich, triple bond makes the linear molecule very rigid and, moreover, allows certain electronic delocalization, which often are key to understand most of the physico-chemical properties of cyanide complexes.
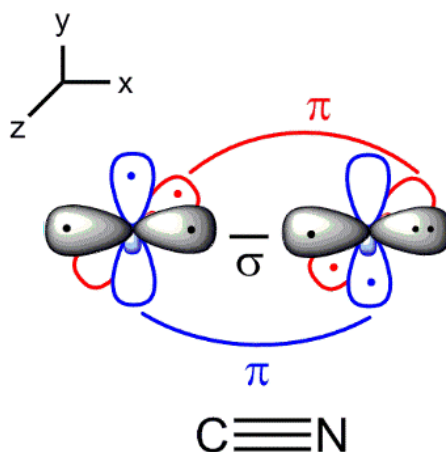
Figure 1.1.2 Orbital scheme and Lewis structure of a cyanide ligand triple bond

1.1.1 Metal-cyanide bonds

The family of cyano-complexes of transition metals is one of the most important in coordination chemistry. Due to its electronic configuration and orbital structure, the cyanide anion is one of the strongest ligands in the spectrochemical series. This means strong ligand field and strong trans-effect[1]. Generally, the carbon atom in the monodentate cyanide is the one linked to the metal ion. According to valence bond theory, a complex arises from the reaction between a ligand and a metal center by formation of a coordinative-covalent bond.

This bonding implies the hybridation between *(n-1)d*, *ns*, *np* and *nd* orbitals of the transition metal ion. For instance, in the $Fe(CN)_6^{-3}$ complex (octahedral) with $d^2 sp^3$ hybrid orbital (Figure 1.1.3).
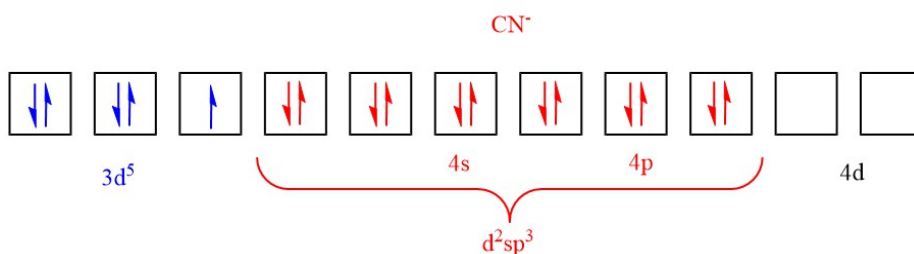
Figure 1.1.3 *Hybridation of $[Fe(CN)_6]^{-3}$*

In a metal-cyanide bond, there two types of overlap: (i) the cyanide anion acts as a Lewis base or σ-donor, giving its electron pair to an empty e_g (d_{x2-y2}/d_{z2}) metal orbitals which creates a σ-bond, as seen in Figure 1.1.4a; (ii) CN^- can act as a Lewis acid, or π-acceptor, taking electrons from a full t_{2g} $(d_{xy}/d_{xz}/d_{yz})$ metal orbital (Figure 1.1.4b). Both interactions, σ-binding and π-backbonding give rise to very stable M-CN bonds.
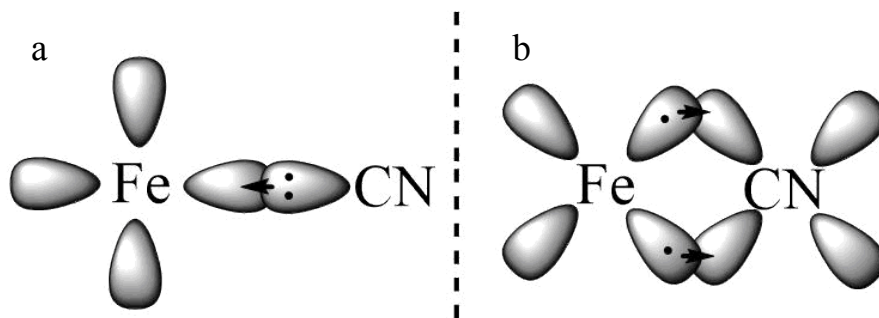
Figure 1.1.4 *Orbital overlap in an iron -cyanide bond. σ (a) and π (b)*

The C-N stretching frequency (v) in vibrational spectroscopy (IR) is directly related to the CN^- bond strength. In general, bond strength increases upon σ-donation, while decreases upon π retro-donation. In cyano complexes, the wavenumber ($\widetilde{v}$) is mainly related to three parameters:[2]

- Electronegativity: The smaller the electronegativity of the metal center, the lower the σ-donation from the ligand would be, and as a consequence, $v_{(CN)}$ is expected to be lower.

- Oxidation state: The higher the oxidation state, the stronger the σ-bonding, and the higher is $v_{(CN)}$.

- Coordination number of the metal: As the cyanide ligand is an anion, an increase in the coordination number of the metal center means a decrease of the positive charge on the metal and, thus, reduces the σ-bonding and shifts the $\widetilde{v}$ to a lower wavenumbers.

1.1.2 Types of cyano-metal complexes

As mentioned above, CN^- usually acts as a monodentate ligand, binding from its C-site. Cyano-metal complexes can be mixed (CN^- and a different ligand) or homoleptic (only CN^- ligand). Homoleptic cyanocomplexes have the general formula $[M^{b+}(CN)_x]^{(x-n)-}$, are anions , and exhibit a wide range of metal ligand ratios. The most common coordination structures are:

- Lineal: i.e. $[Ag(CN)_2]^-$
- Triangular: i.e. $[Cu(CN)_3]^{2-}_n$
- Tetrahedral: i.e. $[Zn(CN)_4]^{-2}$ and $[Cd(CN)_4]^{3-}$
- Square planar: i.e. $[Ni(CN)_4]^{2-}$
- Trigonal: i.e. $[Ni(CN)_5]^{3-}$
- Octahedral: i.e. $[Co(CN)_6]^{3-}$ and majority of hexacoordinate species $[M^{b+}(CN)_6]^{n-}$

A paradigmatic example is the octahedral iron cyanide, $[Fe(CN)_6]^{3-/4-}$, which can coexist in reduced ferro (Fe^{II}) and oxidized ferri (Fe^{III})-cyanide forms. Both forms have a low spin ground state because of the strong field ligand cyanide.

These cyanometallates being anionic, may also act as ligands towards a second metal cation, forming complexes where the cyanide ion acts as bidentate ligand. This happens, for example, in linear polymeric species, such as silver cyanide or gold cyanide. The strict linearity, and electron delocalization offered by the cyanide bridging ligand, favors strong electronic overlap between metal centers providing many possibilities towards the strategic building of electroactive frameworks and coordination polymers with numerous applications[3,4,5,6,7,8,9]. Amongst them, Prussian blue and its analogues exhibit a central role.

1.2   Prussian blue

1.2.1. History of Prussian blue

Prussian blue (PB), $Fe^{III}_4[Fe^{II}(CN)_6]_3$ xH_2O, which got its name "Prussian" from the fact that it was used to dye Prussian military uniforms, is regarded as the first found transition metal coordination compound. Its serendipitously discovery is attributed to Diesbach and Dippel, around 1706, as the first purely synthetic pigment. Its bright color, due to metal-metal intervalence Fe^{II}-Fe^{III} charge-transfer, its inexpensive preparation and its high resistance in ambient conditions made Prussian blue to be a huge commercial success. It rapidly became an artists' favorite pigment[10], Picasso, van Gogh or Hokusai would use it with devotion, even when other pigments were available. Diesbach and Dippel were identified as the original inventors, while working in the laboratory of Frisch, author of the first known publication about the pigment in the paper "Notitia Coerulei Berolinensis nuper inventi" in 1710. Frisch had the exclusivity of the pigment for several years, selling it by the ton to France, the Netherlands, Switzerland, Italy, Rusia, Armenia, etc. Caspar Neumann disclosed the secret preparation to John Woodward at the Royal Society in London in 1923, because of uncertain motives. After that, Prussian blue production began throughout Europe, although with different names, such as Paris blue, Berlin Blau, Milori Blue or Turnbull's blue. Soon afterwards, chemists rapidly discovered how the properties of such a wonderful pigment could be tuned by incorporation of additional metals, and in 1724 the first PB analog (PBA) was reported. By the beginning of the 20th century, over 100 preparation methods were already documented. Nowadays, PBs maintains still a huge role in the pigment industry, with current research devoted to nanoparticle-based inks for the primary colors.

Figure 1.2.1 *"Entombment of Christ" (Picture Gallery, Potsdam) by Pieter van der Werff. The oldest painting where PB has been identified, dated 1709. Prussian blue is used in the sky, and in Mary's veil (ref. 11)*

1.2.2. Crystal structure and composition

The Prussian blue crystal structure was a mystery until 1936, when Keggin and Miles postulated a model from powder X-ray diffraction patterns. This first model correctly disclosed the polymeric nature of this coordination polymer, but also included some wrong assumptions, such as the presence of randomly distributed Fe^{III} ions in interstitial positions to achieve electroneutrality.

Buser et al. obtained good quality PB single crystals for X-ray diffraction studies by slow diffusion of water vapor into a very diluted solution of the building blocks in concentrated hydrochloric acid. Their structural analysis[10] showed a deviation from the typically accepted model of face-centered cubic polynuclear transition-metal cyanides in the space group *Fm3m*. Observation of non-face-centered reflections suggested a primitive cubic cell, although some variations were found from comparison between different crystal batches.

The extremely small particle size and its apparently variable stoichiometry arising from analytical uncertainties, made very difficult the correct structural characterization of PB. Preparation method is fundamental for reproducibility, given their non-stoichiometric nature[12]. Analytical methods are complex due to their tendency to adsorb ions and to include zeolitic molecules in their porous structure. Exact composition is hardly well-determine, and properties depend on it. Therefore, sophisticated physical characterization is typically needed.

Although its non-stoichiometric nature the actual stoichiometry and structure is in between two limiting cases: the "insoluble" Prussian blue (IPB), $Fe^{III}_4[Fe^{II}(CN)_6]_3 \cdot xH_2O$ where x = 14-16; and the so-called "soluble" Prussian blue (SPB) $A^IFe^{III}[Fe^{II}(CN)_6] \cdot yH_2O$ where y = 1-5 and A is a monovalent cation such as alkaline or NH_4^+. Actually, both forms are highly insoluble. However, SPB gives the appearance of forming a solution in water because it is easily peptized as a blue colloidal solution, which passes through a filter and does not

form sediment. Prussian blue (density ca. 1.8 g/cm^3) is very light compared with similar iron salts (densities >3 g/cm^3).

Figure 1.2.2 depicts the structures of the two Prussian blue forms. SPB is a coordination polymer with face centered cubic structure, where octahedral metal cations occupy special positions, bridged by cyanide ligands. The tetrahedral sites left open by this rigid structure are available for interstitial solvent molecules, or counterions (A). In IPB, a quarter of the $[Fe^{II}(CN)_6]^{4-}$ units are missing to maintain electroneutrality, since no additional counterions are present. This packing arrangement leaves some cavities in the crystal lattice that are occupied by water molecules. In addition, the coordination sphere of each Fe^{III} center around the vacant site is completed by a water molecule. Therefore, the water molecules in the formula $Fe_4^{III}[Fe^{II}(CN)_6]_3 \cdot xH_2O$ can be divided into two types: coordinative and zeolitic.
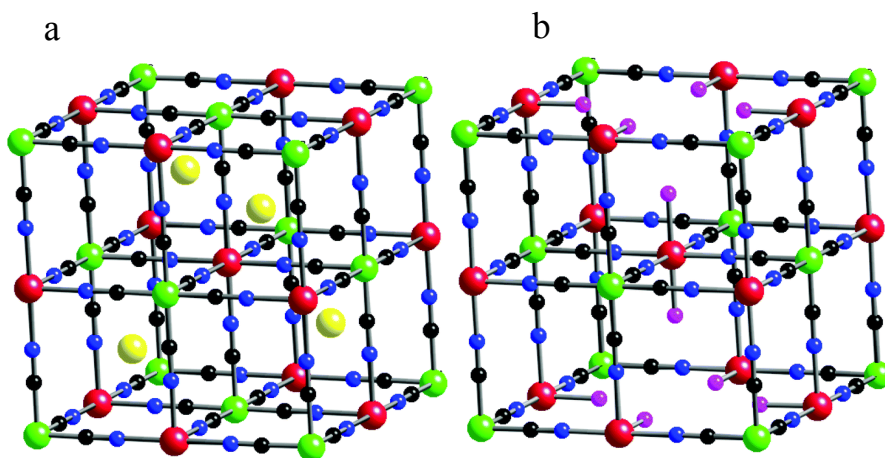
Figure 1.2.2 *Structures of soluble Prussian blue (a) and insoluble Prussian Blue (b). For clarity, waters molecules have been omitted except for oxygen of the coordinated water in the right figure. Fe^{II} (green), Fe^{III} (red), alkaline (yellow), carbon (black), nitrogen (blue) and water oxygen (pink).*

1.2.3. Properties.

I.   Redox behavior of Prussian blue

The cyanide ligand enables effective charge transfer between the iron centres, mainly due to the overlap with the nitrogen p-orbital. The band gap corresponds to the intervalence Fe^{II}-CN-Fe^{III} charge transfer (CT) transition, which has a maximum wavelength of approximately 700 nm. This corresponds to the red region of the visible spectrum, thus explaining its characteristic blue colour.

$$Fe^{III}[Fe^{II}(CN)_6]^{4-} \xrightarrow{\ hv\ } Fe^{II}[Fe^{III}(CN)_6]^{3-}$$
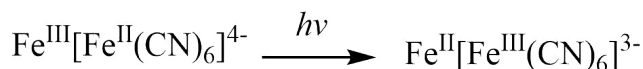
Figure 1.2.3 *Charge transfer transition in Prussian blue*

Consequently PB is redox active, and can be reversibly oxidized or reduced to Prussian yellow (PY) and Prussian white (PW)[13]; respectively (structural details in Figure 1.2.6). The former is also called Berlin green, the latter is also commonly referred to as Everitt's Salt. Only Fe^{III} ions are present in PY and only Fe^{II} in PW. This rich redox/electrochromic electrochemistry has been explored in a great variety of substrates, for applications in devices, displays and sensors[14,15,16,17,18,19]

$$K_2Fe^{II}[Fe^{II}(CN)_6] \xleftrightarrow{\ K^+/e^-\ } KFe^{III}[Fe^{II}(CN)_6] \xleftrightarrow{\ K^+/e^-\ } Fe^{III}[Fe^{III}(CN)_6]$$

Prussian White   Prussian Blue   Prussian Yellow
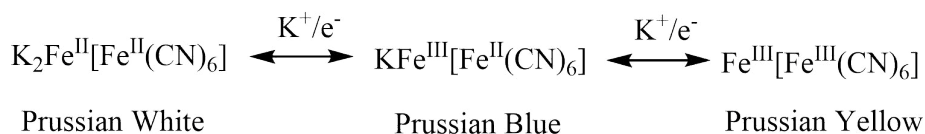
Figure 1.2.4 *Relationship between the PW, SPB and PY structures*
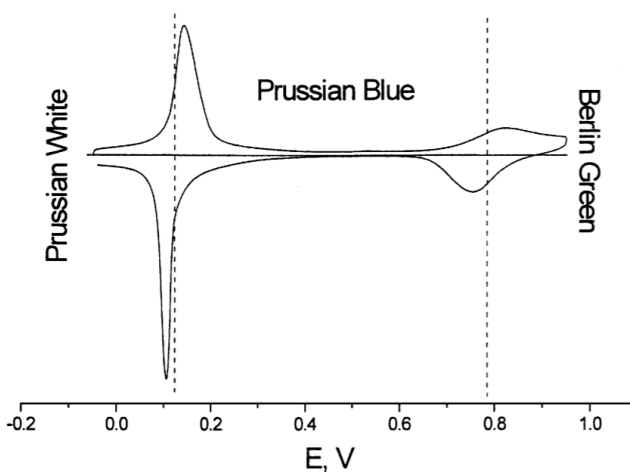
Figure 1.2.5 *Typical cyclic voltagram of Prussian Blue modified smooth glassy carbon electrode, 0.1M KCl, 40mV/s vs SCE (from ref.13)*
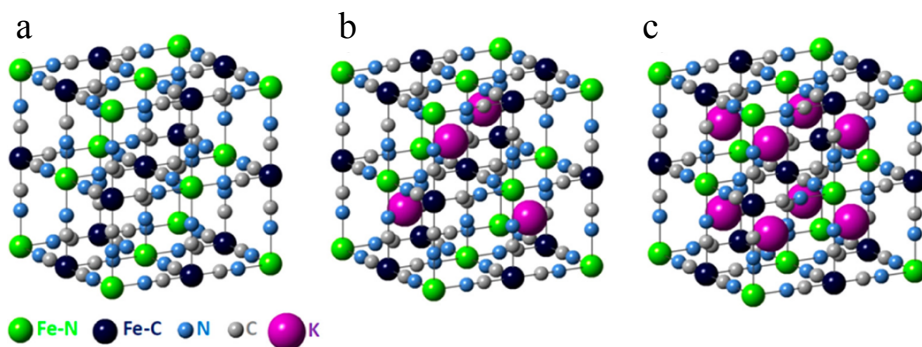
Figure 1.2.6 *Structures of Prussian yellow (a), Prussian blue o "soluble" Prussian blue (b) and Prussian white (c) (adapted from ref.20)*

II.   *Magnetic properties of Prussian blue.*

Since CN^- is a strong ligand when coordinating from its C-site, the iron center linked to carbon is in low-spin (LS) configuration. On the contrary, the weak nitrogen end of cyanide will favor high spin (HS) configuration in the N-bound centers. This gives rise to a total of five unpaired electrons per Fe^{II}-CN-Fe^{III} moiety, with nominal $S = 0$ (LS Fe^{II}, d^6) and $S = 5/2$ (HS Fe^{III}, d^5).

Although the magnetic features of PB were studied since 1928,[21] it was in 1968 when low temperature measurements discovered ferromagnetic ordering below $T_C = 5.6$ K[22]. This magnetic super-exchange between iron centers over 10 Å apart, is due to the electronic delocalization and double exchange between Fe^{III} centers, promoted by the cyanide ligand.
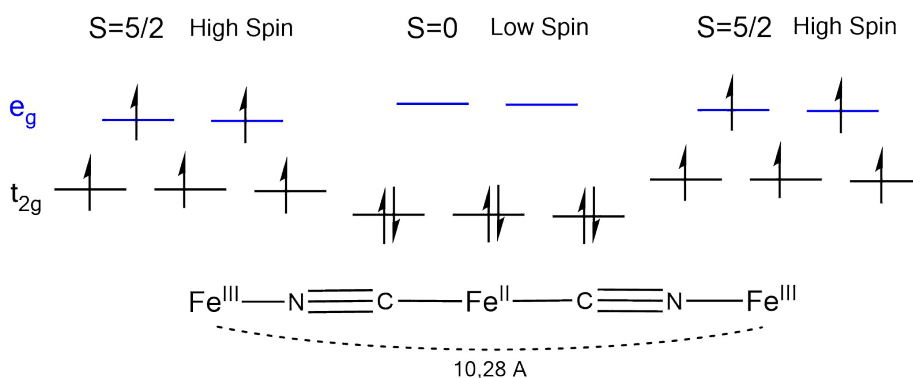
Figure 1.2.7 *Fe^{III}-CN-Fe^{II} moieties in Prussian blue structure. The exchange interaction it is very weak between the paramagnetic centers (Iron centers in a high spin state), which are separate more than 10.20 angstrom.*

1.3. <u>Prussian blue analogues</u>

Many transition metal cations may substitute total or partially the Fe^{III}/Fe^{II} positions in the PB crystal structure, to yield the so-called Prussian blue analogues. These materials have found many applications, where the electronic properties of such a robust and stable coordination polymer may be tuned by their metal composition, oxidation states, or preparation methods. Cyanide can be viewed as the coordination equivalent to oxides, accommodating multiple metal cations, in mixed oxidation states, with non-stoichiometric compositions, but adding a better defined structure, high stability in strong acids, and easy processing from molecular building blocks.

With these molecular approach, materials with extraordinary physical properties have been tailored, [23] including room temperature magnetic ordering, [24] high transition temperature PBA magnets [25,26] magnetic pole reversal [27,28], negative thermal expansion, [29] microporosirity, [30] photomagnetism, [31] ionic conductivity, [32] second harmonic generation [33], multiferroics, spin glass behaviour[34,35], photo induced magnetic transitions[36,37] and photo[38,39,40] and pressure induced[41] electron transfers, and also used for electrochemical applications such as alkali cation solid state batteries[42,43] fuel cells,[44] or electrochromic displays[45,46,47]. Its biocompatibility has also allowed remarkable medical applications as multimodal contrast agents (MRI, optical, photoacustic)[48,49] delivery agents,[50] or anti-radiactive poisoning remedies.[51,52]

In many cases, the transition metals possess different oxidation states that enable electron-to electron transfer due to an energy perturbation. As with the parent PBs, this has led to the formation of many interesting complexes exhibiting a diverse range of optical[53] and electrochemical[54] properties, so they also have potential for device applications such as molecular magnets [55], nanowires[56], electrodes[57]and rechargeable batteries[58]. When combined with their electrocatalytic[59] activity, they have become excellent components for

electrosensors, as selective catalysts for the amperometric detection of a variety of substrates, such as hydrogen peroxide,[60,61,62,63] glucose,[64,65] glutamate,[66] uric acid,[67] and others.[68]

1.3.1. *Structures of Prussian blue analogues*

Prussian blue analogues (PBAs) possess the general formula $AM^{a+}_x[M^{b+}(CN)_6]_z \cdot nH_2O$, in which M^{a+} and M^{b+} are transition metal ions and A is a monovalent counter cation, and can be written, according to Verdaguer and coworkers as $A4xM^{a+}_4[M^{b+}(CN)_6]_{4z}\square_{4(1-z)}\cdot nH_2O$ were $\square$ represented structural vacancies. The PBA structure, like that of PB, from which it is derived, is a three-dimensional cubic lattice of transition metals ions that interact through intermediate CN^- ligands. M^{a+} is octahedrally coordinated by the nitrogen end of the cyanide ligands and M^{b+} is generally coordinated by the C atom. The latter is the stronger bond and M^{b+} has a low spin ground state. The usual means by which a neutral solid complex is obtained is by a simple Lewis acid-base reaction.

Although this reaction looks simple, many experimental parameters may affect the overall outcome, including temperature, solvent, pH, concentration, etc. As for the original PB, the chemical features of the PBAs, including stoichiometry and oxidation states, will strongly depend on the exact synthetic conditions. PBAs are even more versatile than PB, because is open to almost all transition metals in different oxidation states. Their actual stoichiometry and structure is in between two limiting cases:

- $M^{a+}_3[M^{b+}(CN)_6]_2\cdot xH_2O$, with one third of $[M^{b+}(CN)_6]^{(b-6)}$ vacancies are filled with water molecules, averaging a $\{M^{a+}(NC)_4(H_2O)_2\}$ coordination sphere for the M^{a+} cation;

- $A^I_yM^{a+}[M^{b+}(CN)_6]\cdot xH_2O$, isostructural to the SPB structure, with interstitial A^I cations if needed for electroneutrality.

1.4. Thesis goal and outline

In this thesis, we have taken advantage of the multiple possibilities offered by Prussian blue analogues (PBAs) to rationally design materials with novel and promising physical and chemical features. We explored further applications for them, modifying their composition and processing to target several technological issues: water oxidation catalysis, including lab-scale and full-cell electrolyzers; multimodal contrast agents; and multifunctional magnetic materials, combining magnetic ordering and optical activity. Our final goal being the development of multifunctional PBAs in which could attract technological interest.

In the first chapter, we describe the Prussian blue family of materials, with their structural, and physical features. Basic principles on their functionality are correlated to their composition and modifications.

In the second chapter, we explore the catalytic performance of cobalt iron Prussian blue analogues (CoHFe) to promote one of the most challenging reactions nowadays, the oxygen evolution in a water splitting reaction. In particular, we determined the benefits of using CoHFe nanoparticles, which demonstrated improved catalytic features when compared to bulk. Additionally, we confirmed the versatility of this CoHFe catalyst, being active and efficient in a wide pH range; as prepared in multiple electrodes supports; and resistant in exigent working conditions: CoHFe is stable and functional in the long run, even in sea water.

In the third chapter, we move one step closer to real applications, incorporating this catalyst in full-cell devices. On one hand, we built and tested a polymer electrolyte membrane (PEM) containing CoHFe as water oxidation electrocatalyst. Although this device works at 5% the production of a commercial PEM electrolyzer, this is the first example of a working device with no platinum-metal group content in the anode, since the state-of-the-art is

defined by IrO_2. This inexpensive and earth-abundant alternative to current precious metal-based anodic catalysts is promising for further development. On the other hand, we also took advantage of the stability of CoHFe in sea water for the design and construction of a lab scale sea water electrolyzer. A floating electrolyzer, with simple parts and compact construction was built and tested, demonstrating the applicability of this catalyst for such harsh working conditions.

In the fourth chapter, we report our aims to obtain a chiral magnet of high ordering temperature. Our strategy consisted of feeding a chiral ligand into the synthesis of the vanadium-chromium Prussian blue-type coordination polymers (VHCr). Through incorporation of a natural aminoacid (L-proline), we were able to obtain, and characterize chiral magnets with ordering temperatures between 135K and 270K. Their optical activity was confirmed through UV-vis and vibrational circular dichroism data. These chiral molecule-based magnets exhibit spontaneous magnetization at the highest temperatures ever reported, and conveniently close to room temperature. This opens several possibilities for their future application in devices and processes.

Finally, in the fifth chapter, we present our studies for the development of manganese iron Prussian blue analogues (MnHFe) as multimodal contrast agent. These derivatives are potential non-toxic contrast agents for those diagnosis techniques in nuclear magnetic resonance, and optical microscopy (second harmony generation). To expand their multimodal features, we incorporated to their structure heavy alkaline metal cations, to increase their extinction coefficient versus x-ray irradiation. Our strategy was successful, and nanoparticles of these materials demonstrated x-ray attenuation capabilities superior to state-of-the-art commercial tomography contrast agents.

1.5. References

[1] Cotton, F. A.; Wilkinson, G.; Murillo, C. A.; Bochmann, M.; Grimes, R. *Advanced Inorganic Chemistry*. Wiley New York: 1988; Vol. 5.

[2] Nakamoto, K.; "Infrared and Raman Spectra of Inorganic and Coordination Compounds, Part A: Theory and Applications in Inorganic Chemistry", *Wiley,* 6th Ed.

[3] Wang, H.; Li, M.-X.; Shao, M.; He, X. *Polyhedron* **2007**, *26*, 5171.

[4] Wang, S.; Ding, X.-H.; Zuo, J.-L.; You, X.-Z.; Huang, W. *Coordination Chemistry Reviews* **2011**, *255*, 1713.

[5] Wang, S.; Ding, X.-H.; Li, Y.-H.; Huang, W. *Coordination Chemistry Reviews* **2012**, *256*, 439.

[6] Batten, S. R.; Murray, K. S. *Coordination Chemistry Reviews* **2003**, *246*, 103.

[7] Batten, S. R.; Neville, S. M.; Turner, D. R. *Coordination Polymers: Design, Analysis and Application*. Royal Society of Chemistry: 2009.

[8] Lescouëzec, R.; Vaissermann, J.; Ruiz-Pérez, C.; Lloret, F.; Carrasco, R.; Julve, M.; Verdaguer, M.; Dromzee, Y.; Gatteschi, D.; Wernsdorfer, W. *Angewandte Chemie International Edition* **2003**, *42*, 1483.

[9] Efremova, O. A.; Mironov, Y. V.; Fedorov, V. E. *European Journal of Inorganic Chemistry* **2006**, *2006*, 2533.

[10] Buser, H. J.; Schwarzenbach, D.; Petter, W.; Ludi, A. *Inorganic chemistry* **1977**, *16*, 2704.

[11] Bartoll, J. In *The Early Use of Prussian Blue in Paintings*, Proceedings of the 9th International Conference on NDT of Art, 2008; 2008..

[12] Samain, L.; Grandjean, F.; Long, G. J.; Martinetto, P.; Bordet, P.; Strivay, D. *The Journal of Physical Chemistry C* **2013**, *117*, 9693.

[13] Karyakin, A. A. *Electroanalysis* **2001**, *13*, 813.

[14] Rosseinsky, D. R.; Lim, H.; Zhang, X.; Jiang, H.; Chai, J. W. *Chemical Communications* **2002**, 2988.

[15] Rosseinsky, D. R.; Lim, H.; Jiang, H.; Chai, J. W. *Inorganic chemistry* **2003**, *42*, 6015.

[16] Kulesza, P. J.; Zamponi, S.; Berrettoni, M.; Marassi, R.; Malik, M. A. *Electrochimica Acta* **1995**, *40*, 681.

[17] Pharr, C. M.; Griffiths, P. R. *Analytical chemistry* **1997**, *69*, 4673.

[18] García-Jareno, J.; Navarro-Laboulais, J.; Sanmatías, A.; Vicente, F. *Electrochimica Acta* **1998**, *43*, 1045.

[19] Roig, A.; Navarro, J.; Garcia, J.; Vicente, F. *Electrochimica Acta* **1994**, *39*, 437.

[20] Hegner, F. S.; Galán-Mascarós, J. R.; López, N. *Inorganic chemistry* **2016**, *55*, 12851.

[21] Davidson, D.; Welo, L. A. *The Journal of Physical Chemistry* **1928**, *32*, 1191.

[22] Ito, A.; Suenaga, M.; Ono, K. *The Journal of Chemical Physics* **1968**, *48*, 3597.

[23] Tokoro, H.; Ohkoshi, S.I.; *Dalton Transactions* **2011,** *40*, 6825.

[24] Ferlay, S.; Mallah T.; Veillet, P.; Verdaguer, M.; *Nature,* **1995**, *378*, 701

[25] Verdaguer, M.; Galvez, N.; Garde, R.; Desplanches, C. *The Electrochemical Society Interface* **2002**, *11*, 29.

[26] Verdaguer, M.; Bleuzen, A.; Marvaud, V.; Vaissermann, J.; Seuleiman, M.; Desplanches, C.; Scuiller, A.; Train, C.; Garde, R.; Gelly, G. *Coordination Chemistry Reviews* **1999**, *190*, 1023.

[27] Ohkoshi, S.-i.; Iyoda, T.; Fujishima, A.; Hashimoto, K. *Physical Review B* **1997**, *56*, 11642.

[28] Ohkoshi, S.-i.; Abe, Y.; Fujishima, A.; Hashimoto, K. *Physical review letters* **1999**, *82*, 1285.

[29] Chapman, K.W.; Chupas, P.J., Kepert, C.J.; *Journal American Society*, **2006**, *128*, 7009.

[30] Dechambenoit, P.; Long, J.R.; *Chemical Society Review*, **2011**, *40*, 3249.

[31] Sato, O.; Iyoda, T.; Fujishima, A.; Hashimoto, K.; *Science,* **1996**, *272*, 704.

[32] Ohkoshi, S.I. *Journal of the American Chemical Society,* **2010,** *132*, 6620.

[33] Ohkoshi, S.; Saito, S.; Matsuda, T.; Nuida, T.; Tokoro, H.; *Journal Physical Chemistry C* **2008,** *112*, 13095.

[34] Buschmann, W. E.; Ensling, J.; Gütlich, P.; Miller, J. S. *Chemistry–A European Journal* **1999**, *5*, 3019.

[35] Pejaković, D. A.; Manson, J. L.; Miller, J. S.; Epstein, A. J. *Physical review letters* **2000**, *85*, 1994.

[36] Sato, O.; Einaga, Y.; Fujishima, A.; Hashimoto, K. *Inorganic Chemistry* **1999**, *38*, 4405.

[37] Ohkoshi, S.-i.; Hashimoto, K. *Interface-Electrochemical Society* **2002**, *11*, 34.

[38] Sato, O.; Iyoda, T.; Fujishima, A.; Hashimoto, K. *Science* **1996**, *272*, 704.

[39] Bleuzen, A.; Lomenech, C.; Escax, V.; Villain, F.; Varret, F.; Cartier dit Moulin, C.; Verdaguer, M. *Journal of the American Chemical Society* **2000**, *122*, 6648.

[40] Vertelman, E. J.; Maccallini, E.; Gournis, D.; Rudolf, P.; Bakas, T.; Luzon, J.; Broer, R.; Pugzlys, A.; Lummen, T. T.; Van Loosdrecht, P. H. *Chemistry of Materials* **2006**, *18*, 1951.

[41] Ksenofontov, V.; Levchenko, G.; Reiman, S.; Gütlich, P.; Bleuzen, A.; Escax, V.; Verdaguer, M. *Physical Review B* **2003**, *68*, 024415.

[42] Nie P.; Shen, L.F.; Luo, H.F.; Ding, B.; Xu, G.Y.; Wang, J.; Zhang, X.G.; P. *Journal of Materials Chemistry A*, **2014**, *2*, 5852.

[43] Yang, D.; Xu, J.; Liao, X.Z.; Wang, H.; He, Y,S.; Ma, Z.F.; *Chemical Communications*, **2015**, *51*, 8181.

[44] Mousavi-Shaegh, S.A.; Nguyen, N.T.; Mousavi-Ehteshami, S.M.; Chan, S.H.; *Energy Environmental Science*, **2012**, *5*, 8225.

[45] DeLongchamp D.M.; Hammond, P.T.; *Advanced Functional Materials,* **2004,** *14*, 224.

[46] Mortimer R.J.; Reynolds, J.R.; *Journal of Materials Chemistry,* **2005**, *15*, 2226.

[47] Ohkoshi S.I.; Tokoro, H.; Matsuda, T.; Takahashi, H.; Irie, H.; Hashimoto, K. et al., *Angewandte Chemie International Edition,* **2007,** *46*, 3238.

[48] Huang, Y.; Hu, L.; Zhang, T.; Zhong, H.; Zhou, J.; Liu, Z.; Wang, H.; Guo Z.; Chen, Q.; *Scientific Report,* **2013**, 3, 2647.

[49] Liang, X.; Deng, Z.; Jing, L.; Li, X.; Dai, Z.; Li, C.; Huang, M.; *Chemical Communications*, **2013**, *49*, 11029.

[50] Shokouhimehr, M., Soehnlen, E.S.; Hao, J.; Griswold, M.; Flask C.; Fan X.; Basilion, J.P.; Basu, S.; Huangal, S.D.; *Journal of Materials Chemistry,* **2010**, *20*, 5251.

[51] Delchet, C.; Tokarev, A.; Dumail, X.; Toquer, G.; Barré, Y.; Guari, Y.; Guerin, C.; Larionova, J.; Grandjean, A.; *RSC Advances*, **2012**, *2*, 5707.

[52] Chen, R.Z.; Tanaka, H.; Kawamoto, T.; Asai, M.; Fukushima, C.; Kurihara, M.; Ishizaki, M.; Watanabe, M.; Arisaka, M.; Nankawa, T.; *ACS Applied Materials & Interfaces*, **2013**, *5*, 12984.

[53] Moore, J. G.; Lochner, E. J.; Ramsey, C.; Dalal, N. S.; Stiegman, A. *Angew. Chem. Int. Ed* **2003**, *42*, 2741.

[54] Pyrasch, M.; Toutianoush, A.; Jin, W.; Schnepf, J.; Tieke, B. *Chemistry of Materials* **2003**, *15*, 245.

[55] Luneau, D. *Current Opinion in Solid State and Materials Science* **2001**, *5*, 123.

[56] Zhou, P.; Xue, D.; Luo, H.; Chen, X. *Nano Letters* **2002**, *2*, 845.

[57] Dunbar, K. R.; Heintz, R. A. Chemistry of Transition Metal Cyanide Compounds: Modern Perspectives. In *Progress in Inorganic Chemistry, Vol 45*, Karlin, K. D., Ed. John Wiley & Sons Inc: Hoboken, 1997; Vol. 45, pp 283.

[58] Jayalakshmi, M.; Scholz, F. *Journal of Power Sources* **2000**, *91*, 217.

[59] De Tacconi N.R.; Rajeshwar, K.; Lezna, R.O.; *Chemistry of Materials*, **2003**, *15*, 3046.

[60] Zhu, N.; Han, S.; Gan, S.; Ulstrup, J.; Chi, Q.; *Advanced Functional Materials*, **2013**, *23*, 5297.

[61] Du, D.; Wang, M.H.; Qin, Y.H.; Lin, Y.H.; *Journal Materials Chemistry*, **2010**, *20*, 1532.

[62] Chen, L.; Wang, X.J.; Zhang, X.T.; Zhang, H.M.; *Journal Materials Chemistry*, **2012**, 22, 22090.

[63] Nossol, E.; Zarbin, A.J.G.; *Advanced Functional Materials*, **2009**, *19*, 3980.

[64] Li J.; Qiu, J.D.; Xu, J.J.; Chen, H.Y.; Xia, X.H.; *Advanced Functional Materials* **2007**, *17*, 1574.

[65] Wang J.; *Chemical Reviews*, **2008**, *108*, 814.

[66] Karyakin, A.A.; Karyakina, E.E.; Gorton, L.; *Analytical Chemistry*, **2000**, *72*, 1720.

[67] Wang, Z.D.; Ma, Y., Hao, X.G.; Huang, W.; Guan, G.Q.; Abdula, A.; Zhang, H.; *Journal Materials Chemistry A*, **2014**, *2*, 15035.

[68] Chen, S.M.; Journal of Electroanalytical Chemistry, **2002**, *521*, 29.

Prussian blue coordination polymers as water oxidation catalyst

2.1. Introduction

2.1.1. Motivation: Energy and Environment

Population growth and living standards are creating an increase on the global energy demand. The world population in 2015 was 7.347 bill. with a projected increase close to 11.213 bill. in 2100, according to United Nations[1]. Moreover, energy consumption, according to the European Commission, has increased by 74% in 9 years. Rising from 9.227 million toe (tonnes of oil equivalents) in 1995 up to 13.699 million toe in 2014 (Table 2.1.1). Around 80% of the energy consumed comes from non-renewable sources (petroleum, lignite and gas). On the contrary, nuclear energy and renewable energies and waste accounted just for 4,8% and 13,8%, respectively. (Figure 2.1.1)

Table 2.1.1 *World Gross Inland Consumption by Region.*
(Source: International Energy Agency, August 2016)

	1995	*2000*	*2005*	*2010*	*2014*	*2014 (%)*
EU-28	1648	1695	1793	1725	15651	11,4
China	1055	1149	1830	2629	3066	22,4
United States	2067	2273	2319	2215	2216	16,2
Asia	867	10387	1237	15265	1741	12,7
Russia	637	619	652	688	711	5,2
Africa	444	496	600	694	772	5,6
Middle East	307	353	468	623	721	5,3
Rest of the world	2202	2414	2635	2852	2907	21,2
World	**9227**	**10037**	**11533**	**12952**	**13699**	**100**
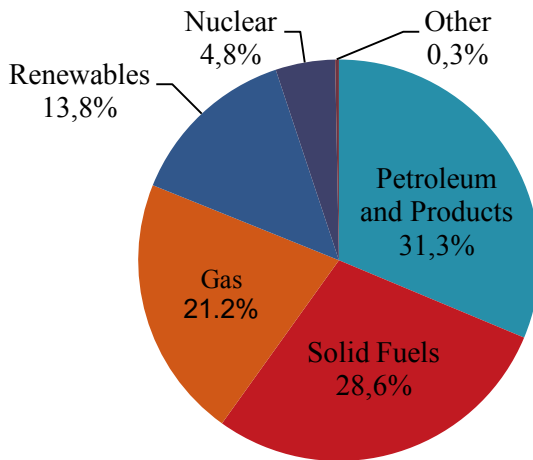
Figure 2.1.1. *World Gross Inland Consumption by Fuel* [2]
(Source: International Energy Agency, August 2016)

These data show the enormous dependence of humanity on fossil fuels (Figure 2.1.1). Unfortunately, consumption of fossil fuels is producing a potentially significant global issue, since it leads to carbon emissions in the form of CO_2 (and other major pollutants) which have negative effects on the environment and long term effects on human health are predicted. Global climate is changing: average surface temperatures have increased, ocean pH has decreased, rainfall patterns have changed, and sea level has risen since industrial revolution[2,3].

With no doubt, meeting this huge demand of energy in a competitive, reliable, clean and sustainable manner is so far the most important scientific and technical challenge in the 21st century. Among the known alternative energy sources, such as nuclear fission, hydroelectric, geothermal, wind, biomass and tidal, only solar energy has the potential to provide enough carbon neutral energy to meet future global energy demand[4,5]. While current technologies are quite efficient collecting and transforming solar energy into electricity (photovoltaics), is difficult to envision an exclusively photovoltaic energy future, because of the intrinsic problem of energy storage. Batteries themselves

cannot substitute major energy demands, since most energy cycles depend on fuels. There is a major reason: chemical fuels are the most convenient and efficient energy storage vector, easy to transport, long term stable and available and ready to provide energy on demand. A scheme able to transform solar energy directly into fuels would be a dream come true.

2.1.2. Use of solar energy.

All the energy consumed by humans in an entire year, correspond to the solar energy that reaches Earth in one hour. This fact makes sunlight the most promising carbon-neutral energy source for the future, as solar radiation is available at any location on the surface of the Earth. Regardless of location, the maximum power density of sunlight on Earth is 1000 watts per centimeter square. The solar source is commonly described in terms of insolation, which means the energy available per unit of area and time, such a kilowatt-hours per square meter per year. Depending on location, the annual insolation can vary over the Earth by factor of three, as an example in northern Scandinavia and Canada the insolation is about 800 kilowatt-hours per square meter a yea, on the contrary a maximum of 2500 kilowatt-hours per square meter a year can be reached in some desert areas[6].

On this regard, it is well documented that solar energy has enough potential to supply current energy consumption in the next century. The extent use of solar energy as primary energy source will be determined by three factors: (i) capture and conversion of the energy contained in solar photons; (ii) solar energy storage; and (iii) cost effective implementation into the global energy markets[5,6,7]. Capture and conversion of solar photons is accomplished by photovoltaics, which generally cannot compete with conventional power plants in grid connected applications. Photovoltaic electricity production cost vary between 0.3-1.5$ a kilowatt-hour, depending on solar insolation, turnkey cost, depreciation periods, and interest rate. Under favorable conditions and at

favorable sites, the lowest cost figure may come down to 0.05-0.06$ a kilowatt-hour[6].

In the absence of cost-effective storage, solar electricity can never be a primary energy source for society. Energy storage options for solar radiation arise in several forms: potential energy (e.g. pumped-hydroelectric, compressed air, and charge storage); kinetic energy (flywheels); thermal energy (concentrates solar thermal and geothermal; and chemical energy (batteries and fuels). Of all possible methods of energy storage, those with the highest energy densities are chemical bonds in fuels. In addition, the technologies that prevail now are congruent with the rapid adoption of solar-derivative chemical fuels.

A number of fuels can be produced by solar energy[8], such as solar hydrogen or carbon-based fuels, such as methane or carbon monoxide.[9] These fuels can be stored and subsequently provide the basis for later electricity generation, and they are a sustainable solution to small-scale distributed energy storage. Fuels achieve high energy densities through the storage of electrons in the small volume of a two electrons bond between light elements (e.g. C-H, N-H, H-H). In comparing the energy densities of hydrocarbon (C-H based), nitrogen based (N-H), and hydrogen (H_2) it is the latest the one which has the largest energy content of any fuel, making it a very good 'vehicle' for holding and distributing energy. With the ability to hold 120MJ/kg, a relatively small amount of hydrogen is needed to store significant amounts of energy. The stable chemistry of hydrogen also means you can store energy longer than any other medium.

Approaches to produce solar fuels, in general, and hydrogen in particular, include: natural photosynthesis, artificial photosynthesis, thermochemical[10,11]. For the first two approaches to produce solar fuels solar energy is captured via photosynthesis and stored in chemical bonds, the sunlight is used to convert water and/or carbon dioxide into oxygen and other materials[12].

2.1.3. Artificial photosynthesis and water splitting

Natural photosynthesis is the process by which plants, some bacteria and some protistans use the energy from sunlight to produce glucose from carbon dioxide and water. In this process, the solar light is used to rearrange bonds of water molecules to oxygen and hydrogen (Eq. 2.1). Thereupon the hydrogen is fixed by its combination with carbon dioxide to produce carbohydrates (Eq. 2.2)

$$H_2O \rightarrow H_2 + \frac{1}{2} O_2 \qquad\qquad E^o = 1.23V \text{ (Eq. 2.1)}$$

$$CO_2 + H_2O \rightarrow 1/6\ C_6H_{12}O_6 + O_2 \qquad\qquad E^o = 1.24V \text{ (Eq. 2.2)}$$

Note that water splitting is subsumed by the reaction in eq. 2.1 on an electron equivalency basis, thus, the production of the carbohydrate stores only 0.01 eV more energy than water splitting. Therefore, water splitting is used in photosynthesis for solar energy storage, while carbohydrate production is the method used by nature to store the hydrogen that released from water splitting reaction.[22] The understanding of this process is highly important on the development of photocatalytic systems able to capture sunlight and convert it into electric energy by using water as a raw material. Current technology employed for the conversion of solar energy into electric energy can be improved by mimicking the ability of natural photosynthetic organism of storing energy into chemical bonds.

In artificial photosynthesis, sunlight is converted into separated electron/hole pairs employing a photovoltaic cell, and charges are captured with catalysts that mediate water splitting.[38]

Against this background, electrochemical water splitting, with the goal of hydrogen production has become a real, clean alternative to replace fossil fuels. During this process two simultaneous reactions are given. On one hand, the oxidation of water at the anode (oxygen evolution reaction, OER) when a catalyst captures four holes, producing molecular oxygen (Eq.2.3). On the other

hand, in the cathode, a separate catalyst captures four electrons, taking place the reduction of protons to hydrogen (hydrogen evolution reaction, HER) (Eq.2.4).

$2H_2O \leftrightarrow O_2 + H^+ + 4e^-$　　　　$E_{anodic}(V) = 1,229 - 0,059(pH)$ *vs* NHE (Eq. 2.3)

$4H^+ + 4e^- \leftrightarrow 2H_2$　　　　　　$E_{cathodic}(V) = 0,000 - 0,059(pH)$ *vs* NHE (Eq. 2.4)
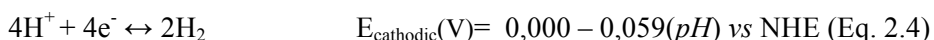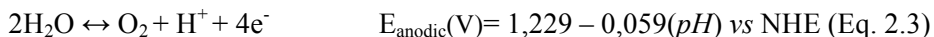
On this regard, it has to be noted that, water oxidation catalysis is the most challenging reaction, due to its high energetic demand, being endothermic with $\Delta G = 4.92$ eV [13]. It is commonly accepted that water oxidation is the bottleneck in water splitting, since it requires four electrons oxidation of two water molecules coupled to the removal of four protons to form an oxygen-oxygen bond. Despite the intrinsic thermodynamic demands of water splitting, kinetics and the reaction mechanism impose an activation energy, which causes an additional potential (overpotential) to overcome the activation barriers, the effects of the concentration gradient or the resistance of the system.

Therefore, we need a water oxidation catalyst that allows us to perform the water oxidation reaction to a potential as close as possible to the thermodynamic potential, so that the process is efficient. Furthermore, water oxidation catalyst must be stable under oxidizing conditions, due to the required potential.

2.1.4. Water oxidation catalysts

A large number of organometallic complexes have been described as homogeneous catalyst since Meyer, in 1982, reported the catalytic oxidation of water by an oxo-bridged ruthenium dimer, known as blue dimer [14]. These complexes have shown high performance in terms of rates and efficiency [15,16,17] and they are easy to optimize and process. Indeed, dozens of water oxidation catalysts (WOCs) from metal complexes with ancillary organic ligands have

been described as WOCs in the last decade, substituting Ru but other metals such as Fe, Co, Ni, Cu, etc. However, all these homogeneous catalysts do not offer long-term stability. Most of them contain organic ligands that are unstable under the strong oxidizing conditions during water splitting process. Hence, it is difficult to envision metal-organic complexes being implemented into water-splitting devices. In the search for technological applications, heterogeneous catalysts have the advantage of higher stability, robustness and easier processability to be implemented.

In the search for catalysts that can work at low overpotentials, stable to air, light, heat or oxidative deactivation metal oxides have been appeared as viable candidates[18,19,20,21] to catalyze water oxidation in a heterogeneous phase, but, the most active, efficient and widely employed materials are oxides of rare and precious metals such as Pt, RuO_2 and IrO_2[22,23,24]. Due to limited availability and high cost of these precious metals, their large scale application is limited as water splitting catalysts. In this context, a large number of materials in the solid state have been investigated as potential water oxidation catalysts, among them, perovskites, transition metal dioxides, layered double hydroxides, spinels and more recently polyoxometalates and Prussian blue analogues.[25,26,27,28,29,44]

The ultimate goal would be to design oxygen evolution catalysts using inexpensive and abundant materials such as transition metals like, cobalt or iron. Electrocatalyts based on earth-abundant elements for oxygen evolution reaction in alkaline media have been well studied[30,31,32,33,34,35,36]. First row transition metal oxides of Co, Fe, or Ni have extremely high performance but only a high pH values (pH>13) where hydrogen production in the half-cell reduction reaction is more difficult[37]. Many of these catalysts are not stable at low pH values and others suffer corrosion or decomposition. One of the most remarkable heterogeneous water oxidation catalyst based in earth abundant materials is the one reported by Nocera[38] where electrodeposited cobalt phosphate layer was used as anode yielding a robust monolithic, photo-assisted

anode able to split water with sunlight at neutral pH. This catalyst shows pH-dependent degradation, making it too costly to compete.

The search for efficient catalysts in acid[39,40,41,42] or neutral solutions[43,44,45,46] based on earth abundant materials for OER is a great challenge. In such operating conditions, nowadays, no catalyst exhibits the efficiency of noble metal oxides, and this significantly increases the cost of this technology.

I.   *Prussian blue derivatives as WOCs.*

The redox chemistry of Prussian-blue type coordination polymers has been well documented for many years[47]. Cyanide is the coordination equivalent to oxide, with peculiar characteristics. The linear binding makes the structures better defined and robust, while maintaining the rich electronic properties arising from non-stoichiometric compositions.

Cyanide as a ligand is as strong as oxo or hydroxo bridges, but stable even in strong acids. Only high hydroxyl concentrations are able to make a nucleophilic attack to the metal centers, promoting transformation of the cyanide architecture into an oxo/hydroxide[48]. Transition metal hexacyanometallates have been studied as components of modified electrodes[49,47] and also as electrocatalyst for the oxidization of organic substrates, moreover, was reported as an efficient reduction catalyst for oxygen[50], where not only the metal centers but also its zeolitic nature was assumed key to explain the remarkable activity. Taking into account that Co centers are the active sites in some of the most successful and efficient homogeneous and heterogeneous water oxidation catalyst,[51,52] cobalt hexacyanometallates appear to possess some of the requirements of a promising WOC:

- High porosity due to $M^{b+}(CN)_6^{-n}$ moieties vacancies, that are filled by water molecules coordinated directly to Co^{II} centers.
- These compounds are robust and highly insoluble in water.
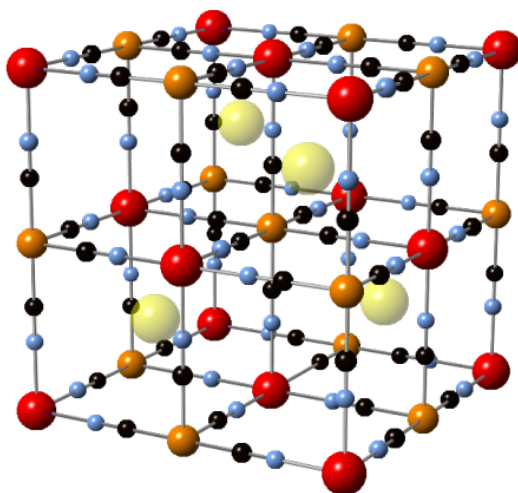
Figure 2.1.2 *Unit cell representation of a face centered cubic Prussian blue type structure. Cobalt (red), iron (orange), carbon (black), nitrogen (blue) and alkaline (yellow)*

They present a high thermal and chemical stability. Thus, it is surprising how PBAs was not systematically explored for one of the most challenging electrochemical reactions: water splitting until 2013, when our group have been demonstrated that cobalt iron Prussian blue analogues (CoHFe) thin films $(K_{2x}Co_{(3-x)}[Fe(CN)_6]_2)$ are efficient and robust electrocatalyst for OER[53] in neutral and acidic electrolyte[54] down to pH=1[55], highly remarkable for precious-metal free materials. At neutral pH, this CoHFe thin films exhibited kinetics that are comparable to those of metal oxides, with long term stability. At low pH, only noble metals exhibit superior performance.

Our hypothesis was that in Prussian blue structure the redox pair Co^{II}/Co^{III}, which is the true catalytic center, would be more stabilized than in the oxide, since cyanide ligand, by its characteristics, allows both, electrons transfer and stabilization of low oxidation states of cobalt.

Characterization experiments were conducted to these modified electrodes after electrochemical water oxidation, including surface-sensitive techniques such Raman or X-ray photoelectron spectroscopy, confirming the absence of any

trace of transition metal oxide. Therefore, the participation of metal oxide nanostructrures evolved during the catalysis was ruled out[54]. In addition, the materials remained in acid media, in which MO_x participation would not be possible.

CoHFe appears to be a viable water oxidation catalyst alternative to metal oxides for promoting water oxidation in devices. They present competitive kinetics, are obtained from earth-abundant elements and can be easily processed as powder, thin-films or nanoparticles, with classic coordination chemistry tools. Furthermore, they are active at neutral or acidic pH, because their stability resides in the strong cyanide bridge in the solid state, with no participation of oxo or hydroxo groups in their skeleton.

Following the results obtained in the water oxidation reaction in our laboratory, both, in thin films and powder through light driven water oxidation[53,55], in this chapter we explore the possibility of processing CoHFe as nanoparticles, and its effect in the electrocatalytic properties. Smaller particle size, and larger surface area was expected to enhance the catalytic genometric activity.

Moreover, we investigate the electrocatalityc activity under different scale-up conditions, such as different pHs or in seawater. Compatibility with organic polymer supports and anion exchange membranes is also addressed. All these studies are looking for possible implementation into water electrolysis devices and future technologies. Regarding technological applications, we will focus in two goals: seawater oxidation conditions; and proton exchange membrane (PEM) electrolyzers. The former, because of its potential as a low-cost raw material, especially if sea water can be used without any pretreatment. The later, because PEM electrolyzers represent the state-of-the-art technology for electrolytic hydrogen production, with the drawback of using noble metals as WOC (IrO_2/RuO_2).

2.2. Results and discussion

2.2.1. Preparation and characterization of Nano-CoHFe

CoHFe nanoparticles (Nano-CoHFe) were prepared by precipitation, mixing $Co(NO_3)_2$ and $K_3Fe(CN)_6$ in formamide in a 5:1 ratio. Co/Fe atomic composition was determined from EDX analyses (Table 2.4.1, experimental section) in good agreement with the major phase $Co_3[Fe(CN)_6]_2 \cdot 14H_2O$. Same procedure was followed in water to prepared standard-size particles.

As prepared, transmission electron spectroscopy (TEM) shows a reduction in particle size compare to the PBA synthetized in water. Rounding edges were also observed, due to the fact that formamide blocks crystals growing by getting coordinated to the Co centers.
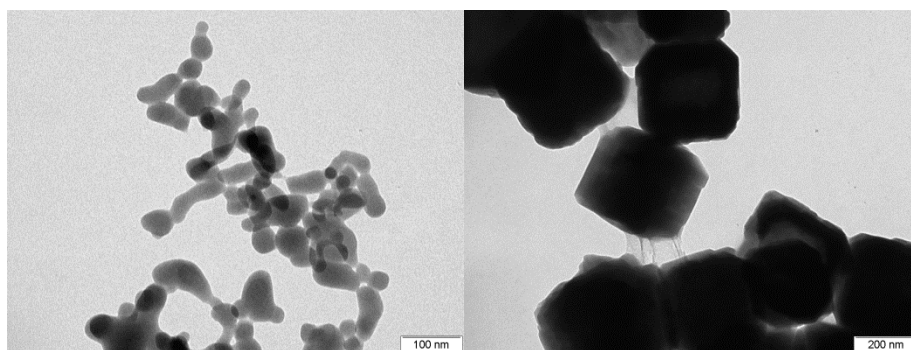
Figure 2.2.1 *TEM images of CoHFe-PBA nanoparticles (left) and CoHFe-PBA (right)*
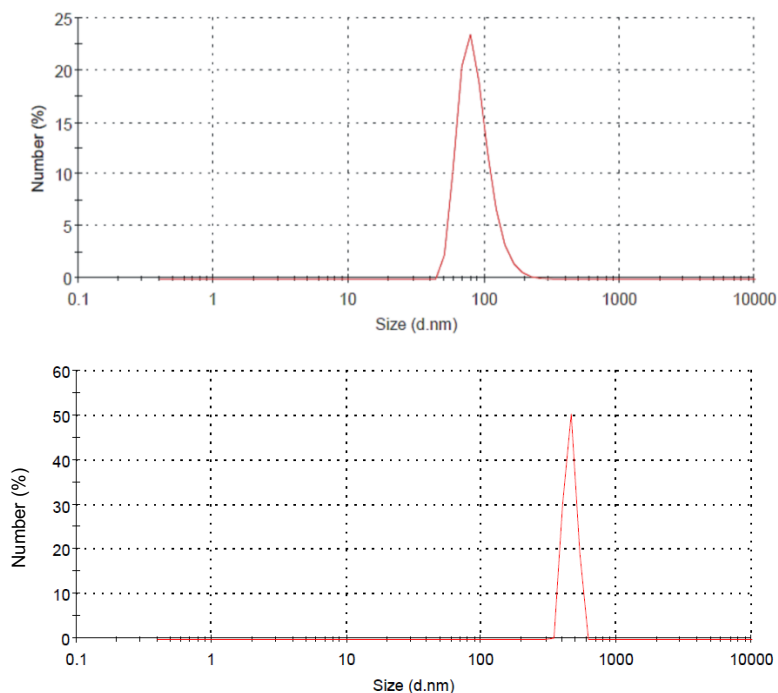
Figure 2.2.2 *DLS signal of Nano-CoHFe (top) and CoHFe in water CoHFe (bottom). Size distribution by number*

We performed dynamic light scattering to measure average particle size. Figure 2.2.2. shown that average particle size in our material is between 40-110 nm, being 450 nm in case of CoHFe synthesized in water. This clearly confirms that our synthetic procedure allows us to significantly decrease the particle size. FT-IR of the nanoparticles shows two major bands in the CN stretching region (Figure 2.2.3). These bands are related to the oxidation state of the metal centers.
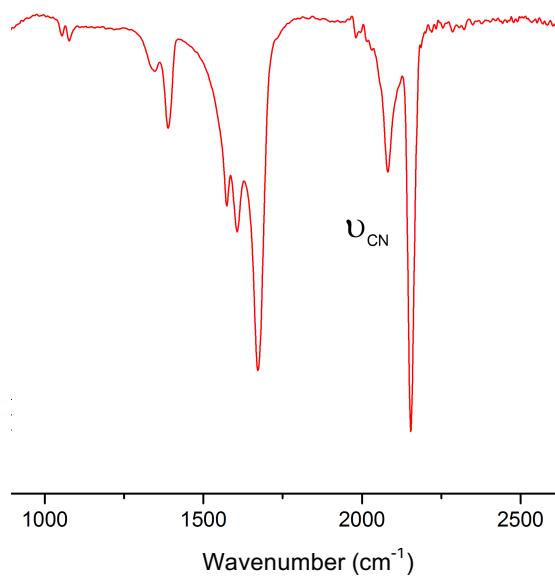
Figure 2.2.3 *FT-IR spectra of CoHFe Prussian blue nanoparticles.*

The strongest one is centered at 2154 cm^{-1} and the second one at 2080cm^{-1}. According to the literature, the first band corresponds to the vibration of the cyanide bridge bound to Fe^{III} and Co^{II}, and the second band corresponds to Fe^{II}/Co^{II} pairs [56,57]. This indicates mixed-valence structure in as-prepared materials. Moreover, confirmed the stoichiometry of the material as was pointed in the infrared spectra by EDX.
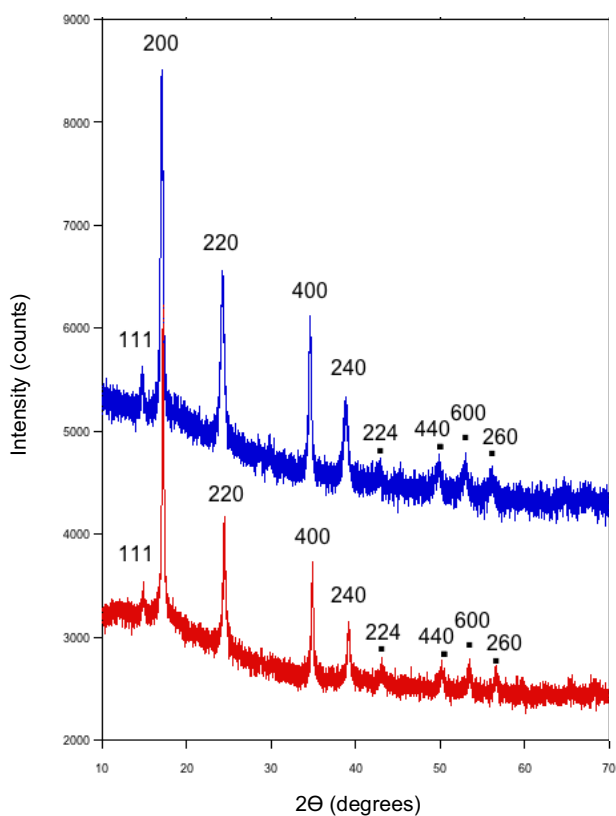
Figure 2.2.4 *Experimental X-ray powder diffraction pattern of CoHFe Prussian blue nanoparticles (blue line) and CoHFe (red line).*

Nanoparticles show the typical X-ray diffraction pattern for a Prussian blue structure, which means that, although we have modified particle size, the crystal structure is preserved[58]. Assuming *Fm3m* space group (face centered cubic structure, FCC), all reflections can be indexed, and no additional reflections were observed. Calculated cell parameter *a* = 1.04 nm and average crystallite size 22 nm. Crystallite size of the samples has been estimated from the line broadening of the most intense Bragg peak (200) using Scherrer's formula.

2.2.2. *Electrocatalytic activity of CoHFe-PBA nanoparticles in seawater.*

The sea is the largest natural water source on the planet. Due to this it has a great potential as source of raw material for obtaining hydrogen. The main problem encountered when working with sea water is that due to high salinity it is a very corrosive medium, where most materials are prone to corrosion.

To evaluate the OER catalytic activity of the CoHFe nanoparticles in seawater, we supported the nanoparticles on FTO electrodes using SiO_2 as inorganic binder. The choice of SiO_2 was motivated because it is stable in the long term to seawater, and in oxidation conditions. For this purpose, we prepared a dispersion of the nanoparticles in a solution of the silica precursor, $Si(OCH_3)_4$ (tetramethyl orthosilicate TMOS), in water and methanol. This solution was subsequently used to coat the FTO electrodes by spin coating, and finally, the electrodes were thermalized in an oven at 60^oC for 30 min to promote polymerization through a sol-gel process[59].

Before seawater experiments, we checked the OER activity for both types of Prussian blue particles through steady state amperometry experiments at neutral pH in a buffer electrolyte (Figure 2.2.5). The current is higher in the case of the nanoparticles in all potential range studied. This confirms enhanced of activity as particle size is reduced, and suggests the most of the active sites are on the surface. Additionally, current density vs potential has an exponential behavior, indicating participation of a catalytic process.
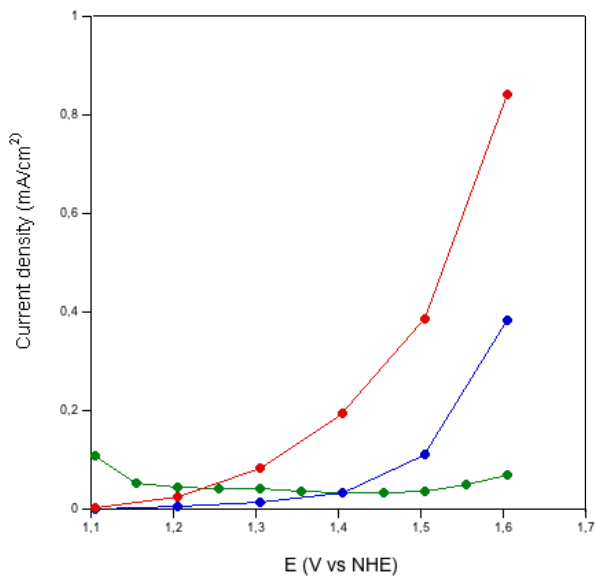
Figure 2.2.5 *State current density measurements for FTO/TMOS ink modified electrodes. Nano-CoHFe (red dots), CoHFe (blue dots) and raw TMOS coated electrode (green dots) in Kpi solution.*
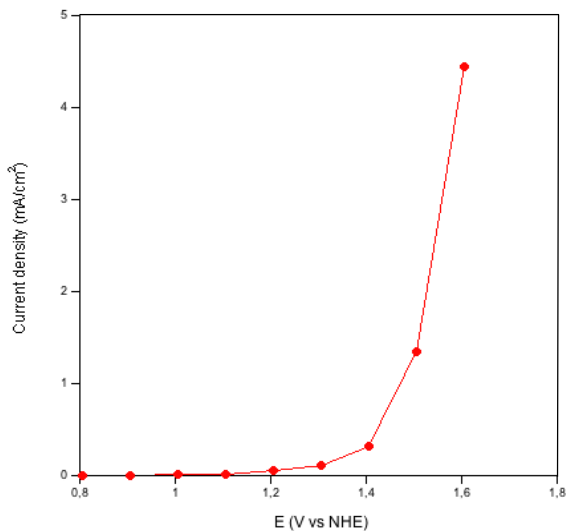
Figure 2.2.6 *Steady-state current density measurements for FTO/TMOS/Nano-CoHFe modified electrodes in seawater.*

We repeated the experiment in sea water with analogous results, but with significantly higher currents. Catalysis starts at a potential close to 1.2 V reaching 4.8 mA /cm^2 at 1.6 V vs NHE (Figure 2.2.6).

The higher currents reached in sea water in comparison to phosphate buffer experiments, may be due to two main reasons. One is the ionic strength of seawater. The concentration of ions in seawater is around 35 g/kg on average[60], which makes it have much higher conductivity. On the other hand we cannot ignore the possible contribution of concomitant chlorine oxidation. Chloride has a standard potential of 1.36 V. Thus, above these potentials, we may have a significant contribution to total current from the chlorine evolution reaction (ClER)

$$2Cl^- \rightarrow Cl_2 + 2e- \qquad E^\circ = 1.36 \text{ V} \qquad\qquad\qquad (Eq. 2.5)$$

$$Cl_2 + H_2O \rightarrow HClO + Cl^- + H^+ \qquad\qquad\qquad (Eq. 2.6)$$

$$HClO \rightarrow ClO^- + H^+ \qquad\qquad\qquad (Eq. 2.7)$$

2.2.3. *Stability of the CoHFe nanoparticles modified electrodes in seawater.*

In bulk water electrolysis experiments (Figure 2.2.7), current density slowly decreases during the first minutes until it reaches a stable value. This initial decay has been observed in most CoHFe electrocatalytic films[53], and has been assigned to mechanical losses of crystallites because of gas bubbles being formed inside the material. Remarkably, this catalyst maintains current densities over 1 mA/cm^2 at reasonable overpotentials, without the use of a conducting support.
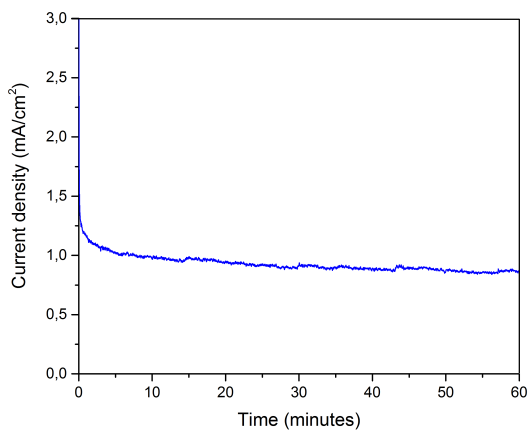
Figure 2.2.7 Bulk water electrolysis at 1.405V vs NHE for 2h CoHFe nanoparticules modified electrodes in sea water.

2.2.4. Electrocatalytic activity of CoHFe nanoparticles in Nafion ink.

Nafion is the state-of-the.-art commercial proton conducting polymer, and the key component of polymer exchange membrane fuel cell (PEMFC), and polymer exchange membrane electrolyzer (PEMEL) assemblies. The anode and the cathode catalysts are adhered on both sides of a Nafion membrane, and then assembled into a cell (further details in chapter three). With the final goal of incorporating CoHFe into a full-cell PEMEL, we studied its activity in a Nafion matrix. Prussian blue nanoparticles were suspended into a Nafion aliphatic, water and ethanol solution, in a sonicator. This ink was drop-casted on a glassy carbon electrode, and let dry for electrochemical characterization.

The cyclic voltamogram (Figure 2.2.8) of these modified glassy carbon electrodes at pH=7 showed a non-reversible oxidation peak centered at 0.9V atribuible to Co^{II}/Co^{III} oxidation[61], preceding a pronounced characteristic water oxidation wave that appears above 1.2V suggesting a catalytic process.
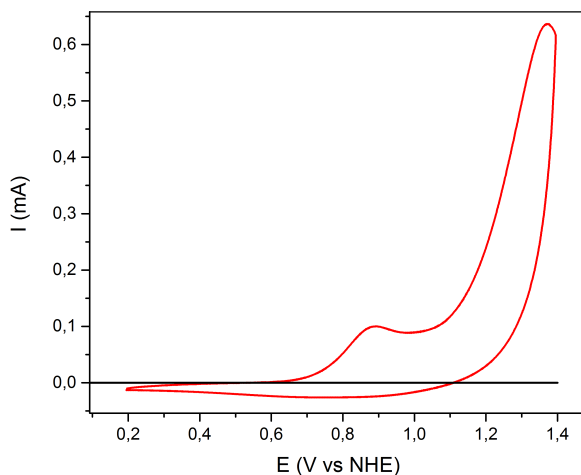
Figure 2.2.8 *Cyclic voltamogram, of glassy carbon modified electrode with Nafion ink containing CoHFe-PBA nanoparticles. Nano-CoHFe (red), glassy carbon (black) in Kpi at pH=7*
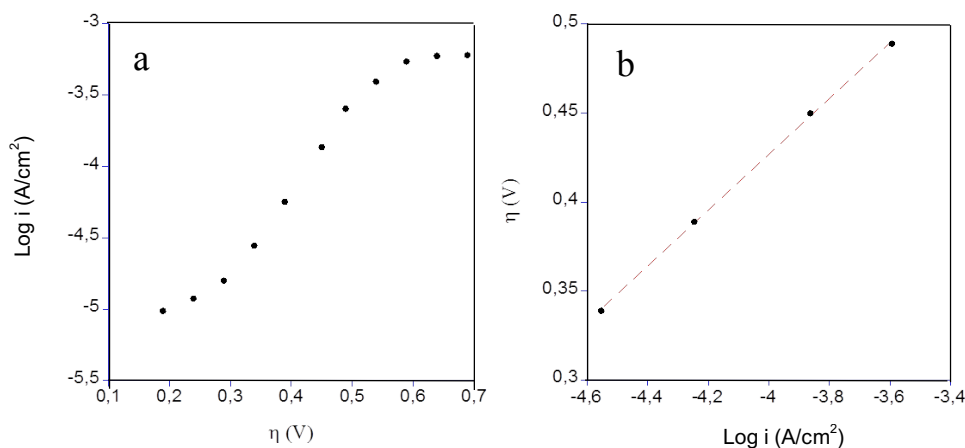
Figure 2.2.9 *Tafel plot in 50 mM Kpi at pH=7 (a). Tafel plot linear fitting (b) y=1.0543+0.15685x; R=0.999974*

For steady–state chromoamperometric measurements, the ink was spin-coated over fluorine doped tin oxide (FTO) glass electrodes. Significant current was detected above 1.205V (vs NHE). At each potential, stable current was reached after ≈ 20 minutes. Tafel plots (Figure 2.2.9) show linear behavior for low overpotentials. The slope is very high, η=157 mV/decade, suggesting slow electron transfer between the electrode and the catalyst, attributed to the intrinsic insulator nature of PB.

Given the high pH stability of PB, we repeated the same experiments as a function of pH (Figure 2.2.8). Even in highly acidic media, the CoHFe electrodes showed catalytic performance and Tafel behavior, although the onset overpotential increases as pH decreases.
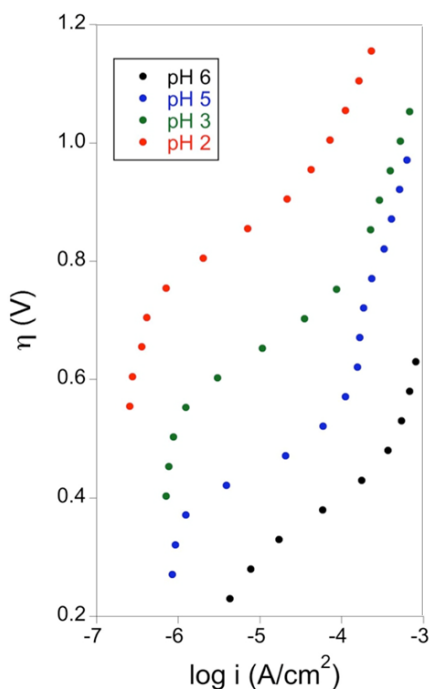
Figure 2.2.10 *Tafel plots of Nano-CoHFe/Nafion/FTO modified electrodes in different pH Kpi solution*
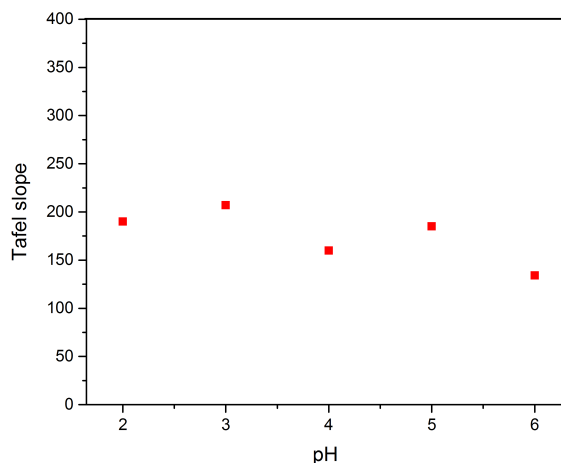
Figure 2.2.11 *Tafel slopes of Nano-CoHFe/Nafion/FTO modified electrodes values at different pH (red dots) in Kpi solutions*

Tafel slope values vary slightly with pH, but remain stable in the studied range (2-6). This is consistent with the results obtained for this type of studies for CoHFe Prussian blue, recently performed by our group[56], and indicates that reaction mechanism does not vary substantially with pH. On the other hand, it also confirms that catalyst is stable at low pH and that, as we have seen in Figure 2.2.11, it continues to maintain a catalytic activity.

The obtained Tafel slops are very high in all cases, between 150 and 250 mV per decade, also much higher than those obtained in CoHFe thin films (80-5mV/decade), previously published by our group[53]. This indicates that the lower activity in the Nafion films is not intrinsic of the CoHFe catalyst, but due to the polymer/catalyst interface. We rationalized that, as part of the Nafion film, the electric contact between electrode and the Nafion-surrounded catalyst is poor.

2.2.4. Stability of CoHFe nanoparticles in Nafion ink modified electrodes.

The medium term stability of these modified electrodes was confirmed by bulk electrolysis experiments and by post-catalysis characterization of the electrodes after water oxidation.

Comparing the current profile showed in Figure 2.2.12 with the one that was obtained in the case of CoHFe thin films[53], as previously mentioned, the current density is about twenty times higher, and current is quite stable. This can be explained through different reasons. On one side, the presence of Nafion as an adherent agent as well as the technique of deposition by spin coating, allows to deposit a larger amount of catalyst besides stabilizing them, and preventing them from being peeled off. On the other side, a decrease in the particle size implies an increase of active area as well as higher number of defects, directly related with the catalytic process.
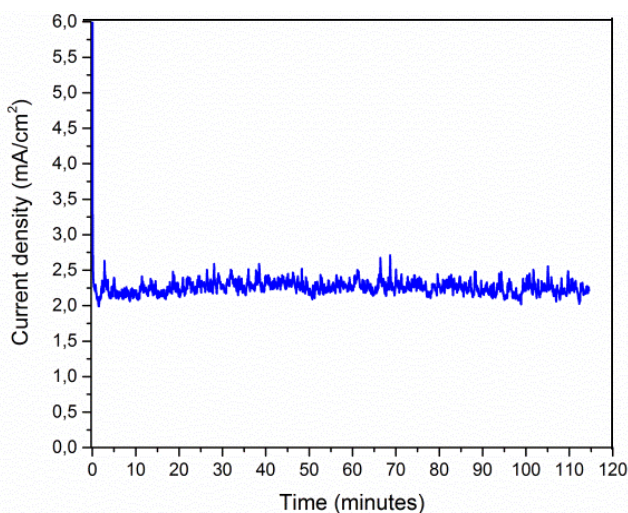
Figure 2.2 12 Bulk water electrolysis at 1.4V for 2 hours of Nano-CoHFe/Nafion modified FTO electrodes,in Kpi buffer solution

Since traces of metal oxides, may evolve during water oxidation catalysis, replacing or modifying the original pre-catalysts, it is essential to use surface sensitive techniques to detect such minor (and sometimes undetectable) adventitious impurities able to contribute to the catalytic process. One of this techniques is Raman spectroscopy.

As it is shown in Figure 2.2.13 all peaks present in the electrodes correspond to those present in the nanoparticles as prepared aswell, and with those reported in the literature for cobalt iron prussian blue[54], except the band that appears to 1600 cm^{-1}, which corresponds to formamide[62] from the synthetic procedure. The typically narrow and sharp oxide bands that appear around 480cm^{-1} and 685cm^{-1} are completly absent, which means that there is no generation of oxides particles, on the surface of the catalyst, during the water oxidation reaction down to the detection limits of this technique.
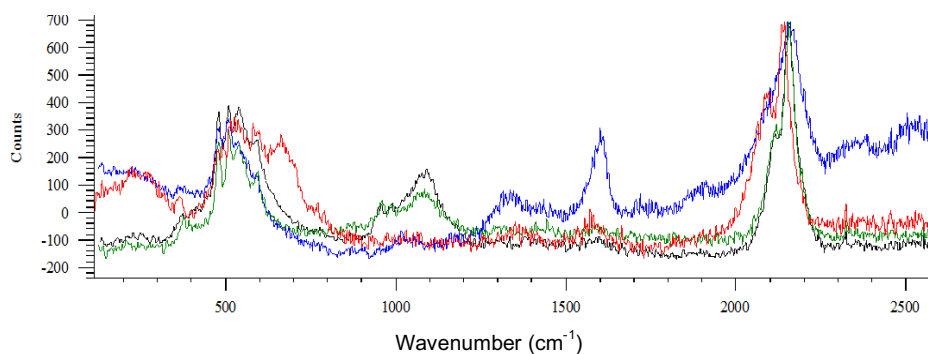
Figure 2.2.13 *Raman spectra of as prepared cobalt iron nanoparticles (black), modified electrode as prepared (blue),modified electrode after steady state current density experiments.After steady state current density experiments at pH=2 (green)*

In the IR spectra (Figure 2.2.14), two original bands, at 2154 cm^{-1} (Fe^{III}-CN-Co^{II}) and 2080 cm^{-1} (Fe^{II}-CN-Co^{II}) are substituted by a very broad band centered at 2120cm^{-1}. This means that during OER the Nano-CoHFe gets homogenized to Co$_4$[Fe(CN)$_6$]$_3$ (4: 3 stoichiometry has been identify by IR band at 2120-2130 cm^{-1}) due to the oxidation of Co^{II} to Co^{III}
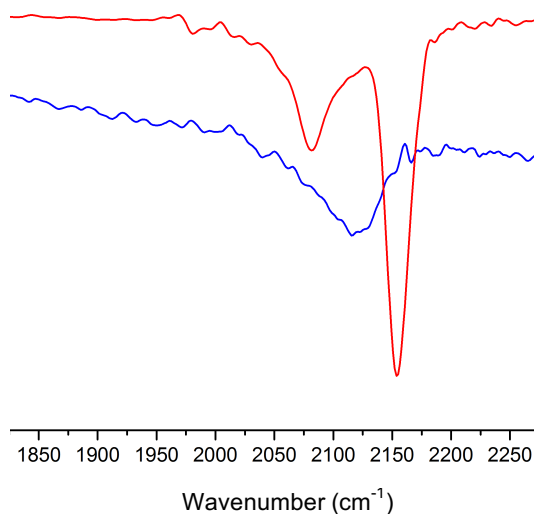
Figure 2.2.14 FT-IR spectra of Nano-CoFe as prepared (red) and after water oxidation reaction (blue)

2.3. Conclusions

Cobalt iron hexacyanometallate nanoparticles can be prepared in aqueous solution from its molecular building blocks, offering unique processing versatility as heterogeneous catalyst. We have demonstrated that cobalt iron Prussian blue nanoparticles can be obtained by an easy and scalable way, substituting water for formamide. These nanoparticles exhibit enhanced catalytic properties, that we assign to the higher relative surface area. In addition, the stability of this material under water oxidation conditions was confirmed and expanded into sea water and acid media. Along its compatibility with the Nafion polymer, these features open interesting possibilities for the implementation of CoHFe nanoparticles in polymer exchange membrane (PEM) electrolyzers, as a noble metal free, inexpensive catalyst. The overpotencials are high at low pH, but the very high Tafel slope indicates this problem comes from poor electron transfer, and not from slow catalysis kinetics. Therefore, this drawback may be overcome by combination of these catalytic nanoparticles with conducting inert supports to improve electron transfer, and total current densities.

2.4. Experimental

2.4.1. Synthesis of CoHFe derivatives

All chemicals were commercially available (<99.%, Sigma-Aldrich) and used without further purification.

CoHFe nanoparticles were prepared by a modified literature procedure [63]. A solution of $K_3Fe(CN)_6$ 0,03M in $Co(NO_3)_2$ 0,15M formamide was quickly added to a formamide solution, as a result we get a dark red-purple dispersion. The mix was kept under stirring 2h. The solid material was dispersed in water and centrifuged (at 6000 rpm) to get a fine red powder by decantation. This purification process was repeated at least three times, up to no traces of formamide is observed in FT-IR spectra. Finally, the nanoparticles were dried at 60ºC, and stored.

Normal size CoHFe was precipitated by adding drop by drop an aqueous solution of $K_3Fe(CN)_6$ 0,03M to $Co(NO_3)_2$ 0,15M water solution at room temperature. After addition, solution was kept under stirring for 2h. Red powder obtained was filtered, washed with water and dried at 60ºC.

2.4.2. *Characterization of CoHFe derivatives.*

Thermogravimetic analysis was performed with powder samples using TGA/SDTA851 Mettler Toledo with Mt1 microbalance.
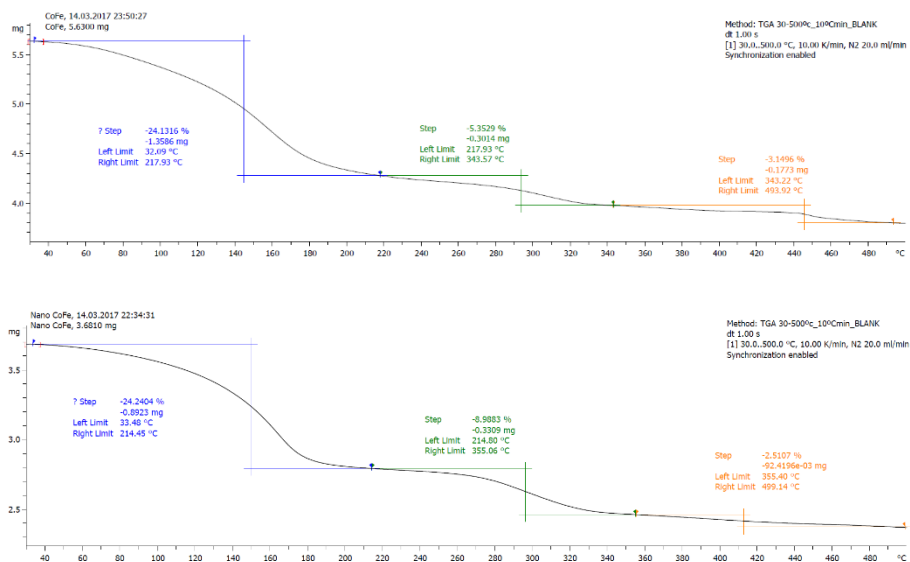
Figure 2.4.1 *Thermogravimetic analysis of CoHFe (top) and Nano-CoHFe (bottom) powders as prepared.*

Infrared spectroctroscopy data were collected in the 3600-600 cm-1 range with Bruker Optics FTIR Alpha spectrometer equipped with Attenuated Total Reflectance (ATR) sample holder.

Powder X-ray powder diffraction data were collected on a D8 Advanced series 2θ/θ powder diffractometer at room temperature in transmission mode or in Bragg-Brentano configuration using a PANAlytical X'pert diffractometer, equipped with a hybrid monochromator, operating with CuKα radiation (λ = 1.541 Å). Cell parameters were calculated by using the (200) peak position, and assuming a FCC geometry.

Energy dispersive X-ray spectroscopy was used to analyze metal content of CoHFe PBA with scanning electron microscope JEOL-JMS400 equipped with an Oxford EDX analyzer (Oxford Instruments).

Table 2.4.1 Composition data in atomic percentage obtained by EDX

Measurements	Compound	Fe (Atomic %)	Co (Atomic %)	Co/Fe Ratio
1		40,01	59,99	1.50
2		37,6	62,4	1.65
3	CoHFe	40,7	59,3	1.46
Mean		39,44	60,56	1.49
1		39,82	60,18	1.51
2		35,12	64,88	1.84
3	Nano-CoHFe	38,34	61,66	1.61
Mean		37,76	62,24	1.65

Dynamic Light scattering of CoHFe PBA size distribution was measured using a Malvern nanoZS analyzer. Samples were prepared sonicating particles in water in a 1mg/ml

Raman measurements were acquired using a Renishaw inVia Reflex Raman confocal microscope (Gloucester- Shire, UK), equipped with an Ar-ion laser at 514 nm, a He–Ne laser at 633 nm, and a Peltier-cooled CCD detector (−70∘ C) coupled to a Leica DM- 2500 microscope. Calibration was carried out daily by recording the Raman spectrum of an internal Si standard. Rayleigh scattered light was appropriately rejected by using edge-type filters. Laser power used was 10% of nominal to avoid sample from burning. Spectra were recorded with the accumulation of at least 3 scans with a 30 s scan time each one.

Transmission electron microscopy done with JEOL 2011 in standard conditions samples dispersed water/Ethanol in1:1 and dropped in Cu grids.

2.4.3. Electrochemical water oxidation with CoHFe modified electrodes.

I.   Preparation of the CoHFe modified electrodes.

As fluorine-doped tin oxide coated glass slides (FTO) we used Pilkington NSG TEC 15A 2.2mm slides with 12v14Ω/sq surface resistivity, and 80.0-81.5% transmittance. FTO slides were cleaned prior use by sonication for 10 minutes in basic soapy solution, deionized water and isopropanol, followed by annealing at 400ºC during 30min. Tetramethyl orthosilicate from sigma Aldrich purum, ≥98.0% (GC) Nafion source was perfluorinated resin solution 5 wt. % in lower aliphatic alcohols and water (15-20%) solution).

For CoHFe/TMOS modified electrodes 70μL of 40mgr CoHFe nanoparticles were sonicated for 30 min in 200 μL TMOS, 500μL Ethanol and 500μL water solution and deposited in two steps in 1.5 cm^2 FTO glass through spin coating technique. In a first step, 1000 rpm for 60s, in a second step at 2000 rpm for 10s. Lastly electrodes were air-dried. For CoHFe/Nafion inks on FTO 4mg CoHFe nanoparticles, were dispersed by sonication in 100μL of Nafion solution, 500μL Ethanol, 500μL water, 30 min sonication. Same spin coating conditions were used.

II.   Electrochemical methods

All electrochemical experiments were performed with a Biologic SP-150 potentiostat. All potentials reported in this manuscript were converted to the NHE reference scale using $E_{(NHE)} = E_{(Ag/AgCl)} + 0.209V$. Unless otherwise stated, the buffer electrolyte used for bulk water electrolysis, cyclic voltammetry and steady-state current experiments was prepared at 50mM potassium phosphate (Kpi), and KNO_3 (1M) as electrolyte. All solutions were prepared with MilliQ-Water (typically 18.MΩ-cm resistivity).

Seawater was collected from La Pineda beach (Tarragona, Spain). As pretreatment, only paper filtering was done to eliminate some solid waste and used without further purification.

Phosphate solutions (50mM) at different pH with KNO_3 (1M) were prepared following the Henderson-Hasselbalch equation were $[HA]$ is the molar concentration of the undissociated weak acid, $[A^-]$ is the molar concentration (molarity, M) of this acid's conjugate base and pK_a is $-\log K_a$ where K_a is the acid dissociation constant.

$$pH = pK_a + log\left(\frac{[A^-]}{[HA]}\right)$$ (Eq.2.8)

Bulk water electrolysis was carried out with well-stirred in two-chamber cell (H cell), with a porous frit connecting both chambers. In one chamber we placed a Pt mesh counter electrode, and in the other chamber working electrode (FTO or GC) and BASi Ag/AgCl (KCl saturated) reference electrode.

Cyclic voltammetry were collected in the 0.2-1.4 V range (vs NHE) at 100mA/s.

Steady state amperometry experiments at neutral pH in a buffer electrolyte, were performed applying a voltage up current reached stability, fifteen minutes, and then the intensity is calculated by making the mean of the signal of the last minute.

Tafel analysis were carried out by obtaining steady current density data from bulk water electrolysis at different applied potentials. A well-stirred 50mM Kpi (KNO_3 1M) at the desired pH was used as electrolyte in the same set-up than the described for bulk electrolysis experiments. The current of electrolysis were used as steady state data. These measurements were performed applying a voltage up current reached stability for at least fifteen minutes, and then the intensity dot plotted is calculated by making the mean of the signal of the last minute.
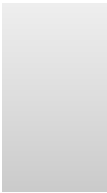
2.5. <u>References</u>

[1]United Nations, D. o. E. A. S. A., Population Division *World Population Prospects. The 2015 Revision, Key Findings and Advanced Tables. Esa/P/Wp.241*; **2015**.

[2] *The EU in the world 2013- A statistical portrait.* Publications Office of the European Union, **2012**

[3] *Fundamental of Materials for Energy and Environmental Sustainability*. Cambridge University Press, **2012**

[4] Lewis N.S.; Nocera D.G.; "Powering the planet: Chemical challenges in solar energy utilization". *Procedings of National Academy of Science of United States of America*. **2006.**

[5] Cook T.; Dogutan D.; Reece S.; Surendranath Y.; Teets T.; Nocera D.; *Chemical Review,* **2010**, *110*, 6474.

[6] United Nations Development Programme. *World Energy Assessment Report: Energy and the Challenge of Sustainability.* **2003**

[7] Lewis, N. S. *Science* **2007**, *315*, 798.

[8] Heeger A.J.; "Solar fuels and artificial photosynthesis report". *Royal Society of Chemistry* **2012**

[9] Barber J.; "Photosynthetic energy conversion: natural and artificial" *Chemical Society Review*, **2006**, *38*, 185

[10] Chen, H.; Cong, T. N.; Yang, W.; Tan, C.; Li, Y.; Ding, Y. *Progress in natural science* **2009**, *19*, 291.

[11] Solar fuels and artificial photosynthesis: science and innovation to change our future energy options. *The Royal Society of Chemistry. Report at the 1st UK Solar to Fuels Symposium*. **2012**

[12] Styring, S. *Ambio* **2012**, *41*, 156.

[13] Dau H.; Limberg C.; Reier T.; Risch M.; Roggan S.; Strasser P.; *ChemCatChem*, **2010**, *2*, 724

[14] Gersten, S. W.; Samuels, G. J.; Meyer, T. J. *Journal of the American Chemical Society* **1982**, *104*, 4029.

[15] Liu, X.; Wang, F. *Coordination Chemistry Reviews* **2012**, *256*, 1115.

[16] Duan, L.; Bozoglian, F.; Mandal, S.; Stewart, B.; Privalov, T.; Llobet, A.; Sun, L. *Nature chemistry* **2012**, *4*, 418.

[17] Ellis, W. C.; McDaniel, N. D.; Bernhard, S.; Collins, T. J. *Journal of the American Chemical Society* **2010**, *132*, 10990.

[18] Hocking, R. K.; Brimblecombe, R.; Chang, L.-Y.; Singh, A.; Cheah, M. H.; Glover, C.; Casey, W. H.; Spiccia, L. *Nature Chemistry* **2011**, *3*, 461.

[19] Minguzzi, A.; Fan, F.-R. F.; Vertova, A.; Rondinini, S.; Bard, A. J. *Chemical Science* **2012**, *3*, 217.

[20] Sivula, K.; Le Formal, F.; Graetzel, M. *Chemsuschem* **2011**, *4*, 432.

[21] Suntivich, J.; May, K. J.; Gasteiger, H. A.; Goodenough, J. B.; Shao-Horn, Y. *Science* **2011**, *334*, 1383.

[22] Nocera, D. G. *Accounts of Chemical Research* **2012**, *45*, 767.

[23] Yagi, M.; Tomita, E.; Sakita, S.; Kuwabara, T.; Nagai, K. *The Journal of Physical Chemistry B* **2005**, *109*, 21489.

[24] Petrykin, V.; Macounova, K.; Shlyakhtin, O.; Krtil, P. *Angewandte Chemie International Edition* **2010**, *49*, 4813.

[25] Trasatti, S. *Electrochimica Acta* **1984**, *29*, 1503.

[26] Pinaud, B. A.; Chen, Z.; Abram, D. N.; Jaramillo, T. F. *The Journal of Physical Chemistry C* **2011**, *115*, 11830.

[27] Morita, M.; Iwakura, C.; Tamura, H. *Electrochimica Acta* **1979**, *24*, 357.

[28] Trasatti, S. *Journal of Electroanalytical Chemistry and Interfacial Electrochemistry* **1980**, *111*, 125.

[29] Bediako, D. K.; Lassalle-Kaiser, B.; Surendranath, Y.; Yano, J.; Yachandra, V. K.; Nocera, D. G. *Journal of the American Chemical Society* **2012**, *134*, 6801.

[30] Chen, S.; Qiao, S.-Z. *Acs Nano* **2013**, *7*, 10190.

[31] Moir, J.; Soheilnia, N.; O'Brien, P.; Jelle, A.; Grozea, C. M.; Faulkner, D.; Helander, M. G.; Ozin, G. A. *Acs Nano* **2013**, *7*, 4261.

[32] Luo, J.; Im, J.-H.; Mayer, M. T.; Schreier, M.; Nazeeruddin, M. K.; Park, N.-G.; Tilley, S. D.; Fan, H. J.; Grätzel, M. *Science* **2014**, *345*, 1593.

[33] Smith, R. D. L.; Prevot, M. S.; Fagan, R. D.; Zhang, Z.; Sedach, P. A.; Siu, M. K. J.; Trudel, S.; Berlinguette, C. P. *Science* **2013**, *340*, 60.

[34] Niu, K.-Y.; Lin, F.; Jung, S.; Fang, L.; Nordlund, D.; McCrory, C. C.; Weng, T.-C.; Ercius, P.; Doeff, M. M.; Zheng, H. *Nano Letters* **2015**, *15*, 2498.

[35] Liang, H.; Li, L.; Meng, F.; Dang, L.; Zhuo, J.; Forticaux, A.; Wang, Z.; Jin, S. *Chemistry of Materials* **2015**, *27*, 5702.

[36] Lutterman, D. A.; Surendranath, Y.; Nocera, D. G. *Journal of the American Chemical Society* **2009**, *131*, 3838.

[37] Subbaraman, R.; Tripkovic, D.; Strmcnik, D.; Chang, K.-C.; Uchimura, M.; Paulikas, A. P.; Stamenkovic, V.; Markovic, N. M. *Science* **2011**, *334*, 1256.

[38] Kanan, M. W.; Nocera, D. G. *Science* **2008**, *321*, 1072.

[39] Wu, J.; Liu, M.; Chatterjee, K.; Hackenberg, K. P.; Shen, J.; Zou, X.; Yan, Y.; Gu, J.; Yang, Y.; Lou, J. *Advanced Materials Interfaces* **2016**.

[40] Pokhrel, R.; Goetz, M. K.; Shaner, S. E.; Wu, X.; Stahl, S. S. *Journal of the American Chemical Society* **2015**, *137*, 8384.

[41] Frydendal, R.; Paoli, E. A.; Chorkendorff, I.; Rossmeisl, J.; Stephens, I. E. *Advanced Energy Materials* **2015**, *5*.

[42] Huynh, M.; Bediako, D. K.; Nocera, D. G. *Journal of the American Chemical Society* **2014**, *136*, 6002.

[43] Jin, K.; Chu, A.; Park, J.; Jeong, D.; Jerng, S. E.; Sim, U.; Jeong, H.-Y.; Lee, C. W.; Park, Y.-S.; Yang, K. D. *Scientific Reports* **2015**, *5*, 10279.

[44] Kanan, M. W.; Nocera, D. G. *Science* **2008**, *321*, 1072.

[45] Zaharieva, I.; Chernev, P.; Risch, M.; Klingan, K.; Kohlhoff, M.; Fischer, A.; Dau, H. *Energy & Environmental Science* **2012**, *5*, 7081.

[46] Dogutan, D. K.; McGuire Jr, R.; Nocera, D. G. *Journal of the American Chemical Society* **2011**, *133*, 9178.

[47] De Tacconi, N. R.; Rajeshwar, K.; Lezna, R. O. *Chemistry of Materials* **2003**, *15*, 3046.

[48] Buckelew, A.; Galan-Mascaros, J. R.; Dunbar, K. R. *Advanced Materials* **2002**, *14*, 1646.

[49] Itaya, K.; Uchida, I.; Neff, V. D. *Accounts of Chemical Research* **1986**, *19*, 162.

[50] Itaya, K.; Shoji, N.; Uchida, I. *Journal of the American Chemical Society* **1984**, *106*, 3423.

[51] Kanan, M. W.; Nocera, D. G. *Science* **2008**, *321*, 1072.

[52] Yin, Q.; Tan, J. M.; Besson, C.; Geletii, Y. V.; Musaev, D. G.; Kuznetsov, A. E.; Luo, Z.; Hardcastle, K. I.; Hill, C. L. *Science* **2010**, *328*, 342.

[53] Pintado, S.; Goberna-Ferrón, S.; Escudero-Adán, E. C.; Galán-Mascarós, J. R. *Journal of the American Chemical Society* **2013**, *135*, 13270.

[54] Goberna-Ferron, S.; Hernandez, W. Y.; Rodriguez-Garcia, B.; Galan-Mascaros, J. R. *ACS catalysis* **2014**, *4*, 1637.

[55] Han, L.; Tang, P.; Reyes-Carmona, Á.; Rodríguez-García, B.; Torréns, M.; Morante, J. R.; Arbiol, J.; Galan-Mascaros, J. R. *Journal of the American Chemical Society* **2016**. *138,* 16037.

[56] Lezna, R. O.; Romagnoli, R.; de Tacconi, N. R.; Rajeshwar, K. *Journal of Physical Chemistry B* **2002**, *106*, 3612.

[57] de Tacconi, N. R.; Rajeshwar, K.; Lezna, R. O. *Chemistry of Materials* **2003**, *15*, 3046.

[58] Bleuzen, A.; Lomenech, C.; Escax, V.; Villain, F.; Varret, F.; Moulin, C. C. D.; Verdaguer, M. *Journal of the American Chemical Society* **2000**, *122*, 6648.

[59] Figueira, R. B.; Fontinha, I. R.; Silva, C. J.; Pereira, E. V. *Coatings* **2016**, *6*, 12.

[60] Millero, F. J.; Feistel, R.; Wright, D. G.; McDougall, T. J. *Deep Sea Research Part I: Oceanographic Research Papers* **2008**, *55*, 50.

[61] De Tacconi, N. R.; Rajeshwar, K.; Lezna, R. O. *Chemistry of Materials* **2003**, *15*, 3046.

[62] Spectra Data Base for organic compounds SDBS. http://sdbs.db.aist.go.jp/sdbs/cgi-bin/direct_frame_top.cgi

[63] Vo, V.; Van, M. N.; Lee, H. I.; Kim, J. M.; Kim, Y.; Kim, S. J. *Materials Chemistry and Physics* **2008**, *107*, 6.

Implementation of cobalt-iron Prussian blue-type OER catalyst in full-cell electrolyzers

Chapter 3

3.1 Introduction.

Within the search for new non-polluting and carbon-free energies one of the routes being explored with intensity is the use of hydrogen as a clean fuel. Hydrogen is the simplest and most abundant element on earth and, furthermore, it is the only fuel that, either in direct combustion engines or in fuel cells, produces energy with only water as by-product[1,2], so it has the capacity to recycle as it is required by sustainability. In 2003 J. Rifkin wrote "*Hydrogen is the most basic and ubiquitous element in the universe. It is the material of the stars and our Sun and, when properly used, will be the Eternal fuel. It never ends and does not produce harmful emissions of CO_2 when is burned; it is only by-products are heat and pure water. We are at the dawn of a new economy, driven by hydrogen, which will fundamentally change the nature of our markets and social and political institutions, just as coal and steam energy did at the beginning of the Industrial Age*[3]".

However, unlike conventional fossil fuels, hydrogen is not readily available in nature; it must be produced from other sources. The current paradox resides in that around 96% of the 65 millions tons per year of hydrogen produced globally is obtained from the reforming or gasification of fossil fuels in refineries[4]. So, in this implementation "Hydrogen economy"[5,6,7,8] is unsustainable. Thus, it is necessary to discard fossil fuels-based hydrogen production, and to exploit renewable energy sources instead (*e.g.* sunlight, wind, wave or hydro-power) with alternative methods of production, such as chemical, biological, electrolytic, photolytic and thermal cracking of water.
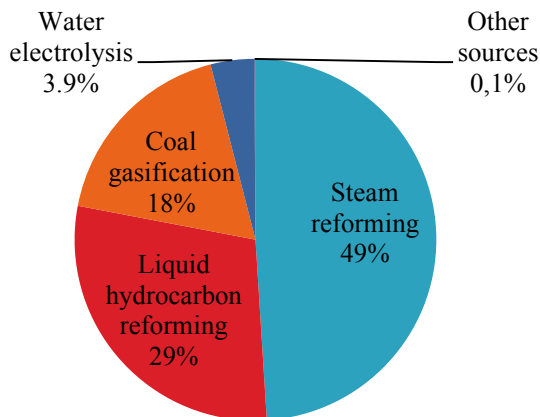
Figure 3.1.1 *Percentage of hydrogen produced by different technologies[9].*

3.1.1. Hydrogen production from fossil fuels.

Hydrogen can currently be produced from fossil fuels mostly by four main technologies:

- Steam reforming (SR): It is the most widespread and inexpensive process [10]. It involves the high temperature (tipically 700-850°C) endothermic catalytic conversion of methane, or other light hydrocarbons, and water vapor into hydrogen and carbon dioxide. The product gas contains approximately 12% of CO, which can be further converted to CO_2 and H_2 thought water shift reaction. The main advantage arises from its high thermal efficiency[*] (around 70-85%)[11] and low operational cost.

- Partial oxidation of natural gas (POX): In this process hydrogen comes from partial combustion of methane with oxygen gas to produce CO and H_2. It is an exothermic reaction, and, therefore does not require external

---

[*] Defined as the lower calorific power contained in the total amount of hydrogen has been produced divided by the total energy supplied to the system.

heating of the reaction neither does it require a catalyst. The process is complemented by further conversion of CO with water steam into H_2 and CO_2. The efficiency for methane fuel it is typically 60-75%.[17]

- Auto thermal reforming (ATR): It is a combination of both, SR (endothermic) and POX (exothermic). Total reaction is exothermic, and so heat is released. The global process is more efficient, simpler and less expensive.[12]

- From carbon coal gasification: Typically, coal is exposed to high temperature under a water flow to produce hydrogen and carbon monoxide. The process must be optimized to the raw material.

Although all these processes are economically highly efficient, due to the very low cost of the raw materials (fossil fuels and water) there are major disadvantages. These forms of production are as contaminant as fossil fuels themselves, not contributing to the establishment of a "carbon-balanced" energy matrix. Additionally, the outcome is low purity hydrogen with a high concentration of difficult-to-separate carbonaceous species such as carbon mono and dioxide, which are highly incompatible with catalysts commonly used in fuel cell systems.[13,14,15,16]

3.1.2. Hydrogen from water splitting

Water is an environmentally clean hydrogen source. It is carbon free, and highly available. So, the most promising method to produce high-quality an high-pure hydrogen ($\approx$100% hydrogen) in both, large and domestic scale, is the electrochemical conversion of water into hydrogen and oxygen through a water electrolysis process: electrochemical breaking of the water molecule into hydrogen and oxygen (Chapter 2, Section 2.1.3). This is a mature technology, which began to be used commercially in 1890.[17]

Unfortunately, electrolytic hydrogen cannot compete in economic terms with fossil-based processes. Electrolytic hydrogen production is a highly energy-demanding process. To decompose water at 25°C, energy of 285.83 MJ/kmol is required. The latter is the formation enthalpy, of which 237.19 MJ/kmol, correspond to the electrical work while the rest is gone to heat. For this reason, this process efficiency* is lower in comparison with the foregoing methods described. Moreover, both semi-reactions (hydrogen evolution reaction, HER, and oxygen evolution reaction, OER) are too slow at the thermodynamic threshold. Important overpotentials are needed to carry out hydrogen production, which implies the use of electrocatalysts. This makes the overall process cumbersome, and economically non-competitive, except for some niche applications (as described in previous chapter)

Additionally, commercial electrolyzers are designed to work in continuous, and their combination with renewable energy sources (which are, by definition, inconsistent) is still an important challenge for their implementation as a clean energy vector. At this moment, electrolytic hydrogen is essentially used for research (due to its high purity) and to store electricity excess (as a solar fuel), as to improve energy grid efficiency. This way, water electrolysis offers more sustainable and cost effective option[18].

I. Hydrogen from seawater

Although water is abundant on the earth, pure water is scarce, because 97.5% is salty, and only 2.5% is fresh water. Moreover, 80% of fresh water is frozen in the icecaps or combined as soil moisture[19].

Taking into account that fresh water is vital for human life and that there are major access problems in large parts of the world[20], it seems obvious the advantage of using salty water sources as feedstock for hydrogen production. This challenge leads to two main strategies:

First option consists of salts content elimination (by distillation, reverse osmosis, etc.) to obtain pure enough water that can be used with current electrolyzers (*e.g.* alkaline, polymer exchange membrane etc). The main advantage of this approach is the use of readily available technologies. The high pretreatment costs (desalinization system), and the environmental problems arising from brine disposal, are the major drawbacks.

A second approach would be the direct electrolysis of seawater, but this technology still needs to be developed, since no electrolyzer can operate in salty environments. The expected advantages are low capital necessities, no need of generation of waste brine solution, because of low impact on overall ocean volume, as well as the possibility to obtain chlorine as by-product. Indeed, chlorine is a valuable intermediate product in industry, and it is produced at large scale by electrolysis of brine, among other production technologies. Around 4% of the electrolytic hydrogen production at industrial scale is obtained as by-product in the chlor-alkali industry[21].

A key problem for the development of this technology is the highly corrosive power of seawater. Most electrocatalysts are attacked/deactivated in such environment, and even more difficult working conditions offers the presence of different chlorine species (Eq. 2.6-2.7). Because of this, only precious platinum (Pt) and iridium (IrO_2) species have been proposed as electrocatalysts[22] for seawater. Their high cost is an economic burden for their commercial applications. Few studies concerning the use of non-precious catalyst for OER in seawater have been reported[23,24,25].

Following our results from chapter 2, we decided to study the feasibility of cobalt-iron Prussian blue analogues as anode catalysts for water splitting in seawater. These Prussian blues are robust materials in brine, not being attacked by strong solution activity. Furthermore, we explored the construction of a lab-scale prototype that could eventually work in open seawaters.

II.   *Hydrogen from pure water.*

Commercial electrolyzers.

The main advantage of fresh water electrolyzers is that several technologies are mature enough at the industrial scale. Compact hydrogen-production systems are available, and can be easily accommodated to both, removable energy sources and domestic scale fuel cells. As an example, Figure 3.1.2 shows a house prototype powered by self-produced hydrogen fuel. In this house, energy from the sun, captured by a photovoltaic cell, and transformed into electrical potential, is used to split water through an electrolyzer during the day). The stored hydrogen is fed into a fuel cell to supply electricity when it is needed, for lights, appliances, and even electric cars.
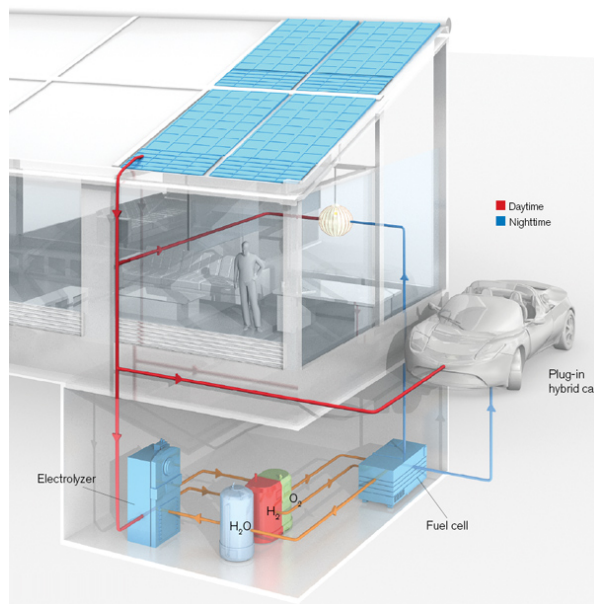

Figure 3.1.2 *Scheme of a house powered by hydrogen* [26]

The basics in a water electrolyser are (Figure 3.1.3):

- DC electrical power source connected to the electrodes that provides the energy required for the process (thermodynamic potential plus overpotencial). It can be provided by the grid, a storage media (e.g. batteries), or a renewal source.
- Two electrodes, the cathode for HER, and the anode for OER. Both compartments must be physically separated to avoid gas products mixing.
- Water (with an electrolyte if needed).
- Transport systems, to move protons and electrons from anode to cathode.
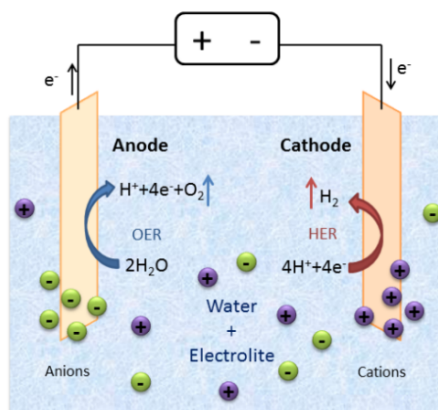
Figure 3.1.3 General scheme of water electrolysis

Depending on the electrolyte, ionic agent (OH^-, H^+, O^{2-}), and the operation temperature, there are three main technologies: (i) alkaline electrolyzers; (ii) proton exchange membrane (PEM) electrolyzers; and (iii) Solid oxide electrolysis cell (SOEC). Only the first two are commercially available.

In alkaline electrolyzers (Figure 3.1.4), a liquid alkaline electrolyte solution of potassium hydroxide or sodium hydroxide is used as feedstock. A diaphragm separates the two electrodes to maintain good product separation. The reactions

in both, cathode and the anode, are those that occur in a water splitting process at high pH values.

The major advantage of this technology is the use of non-precious metal raw materials, including the catalysts. This brings down the costs significantly. It is a mature technology, and commercial devices in cell stacks are available. Its efficiency is not very high (50%-65%). However, the major drawbacks are: (i) the need for corrosive feedstock; (ii) inability to operate at high current flux (<0-.5 A/cm^2) because of high ohmic losses through liquid electrolyte and diaphragm; (iii) poor separation between products (high permeability of the membrane to oxygen) and (iv) carbonation: atmospheric CO_2 gets easily dissolved in the feedstock, lowering the pH and harming function (catalysts, production, etc.).[27]

Cathode: $4H^+ + 4e^- \rightarrow 2H_2$ (Eq. 3.1)

Anode: $4OH^- \rightarrow O_2 + 2H_2O + 4e^-$ (Eq. 3.2)
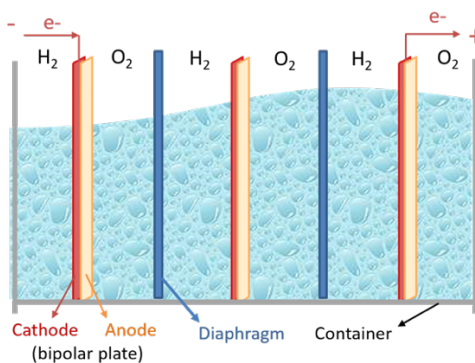

Figure 3.1.4 *General scheme of alkaline stack electrolyzer.*

Proton exchange membrane (PEM) water electrolysis requires no liquid electrolyte, which simplifies the design significantly, allowing to achieve higher efficiencies [28] (50-75%). The electrolyte is an acidic polymer membrane (commonly solid Nafion polymer) which acts as a solid electrolyte that allows

protons to travel of through it, while is electrically insulating, and impermeable to oxygen, which prevents the mixing of both gases. Materials that make up the cathode and the anode are attached to opposite sides of the membrane conforming an assembly called membrane electrode assembly (MEA), the heart of the electrolyzer. Water is introduced at anode side where it is split into protons and oxygen. Protons travel of through the membrane to the cathode where they react with electrons to produce hydrogen molecules.

Anode: $H_2O \rightarrow$ ½ $O_2 + 2H^+ + 2e^-$ (Eq. 3.3)

Cathode: $4H^+ + 4e^- \rightarrow 2H_2$ (Eq. 3.4)
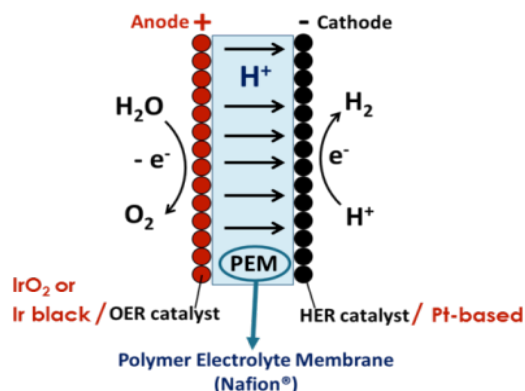
Figure 3.1.5 General scheme of polymeric membrane electrolyzer.

A polymer electrolyte membrane electrolyzer (Figure 3.1.5) has many advantages, among them, capability for compact design and stacking, for operating at high current densities, and also in high-pressure conditions[29]. This is key in terms of high-pressure hydrogen store convenience[30]. On the other hand, main disadvantages are operating requirements: low pH (membrane), and a temperature (typically $80^{\circ}C$) high enough to provide suitable ionic conductivity of the membrane but low enough to ensure its hydration and stability. This limits

construction materials, mainly catalysts: platinum group materials (*e.g.* Pt, Ir, IrO$_2$, Ru, RuO$_2$) for both, cathode and anode. Thus, although production performance meets most of the industrial standards, it is still too costly to compete with fossil fuels reforming.

And lastly, to take advantage that water decomposes at high temperature (water thermolysis) [31], solid oxide electrolyzer cells (SOEC) are being widely investigated[32] In this approach, a water steam is fed through a porous cathode, typically at 700-1000°C. When a voltage is applied, the steam moving through the cathode-electrolyte interface is reduced to form pure H$_2$ and O^{2-} ions. Hydrogen is collected and the superoxide ions are conducted through a solid-state electrolyte (Figure 3.1.6) (*e.g.* mixed oxides or nickel cermet).[33] At the anode interface, oxygen ions are oxidized to form oxygen gas. Despite the high temperature, this process could be coupled to industrial processes, obtaining the required energy from industrial heat waste. The main disadvantage is the need to further develop the solid electrolytes to minimize gas mixtures maintaining high enough currents. Because of this, SOECs are still in the lab-scale phase, with no commercial units available.
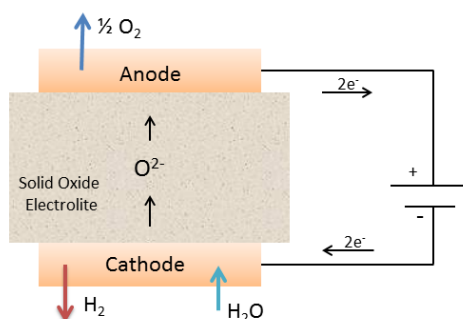

Figure 3.1.6 *General scheme of solid oxide electrolyzer*

Cathode: H$_2$O + 2e$^-$ →H$_2$+ O^{2-} (Eq.3.5)

Anode: O^{2-} → ½ O$_2$ + 2e$^-$ (Eq.3.6)

To sum up, in Table 3.1.1 we show a brief summary about each technology. At this moment, PEM electrolyzers are considered the most promising technology to be combined with renewable energy into a green hydrogen production scheme, mostly due to their high efficiencies, high current densities, portability and no need for corrosive liquids.

Table 3.1.1 *Summary of water electrolysis technologies.*

Type	Alkaline	Polymer electrolyte (PEM)	Solid oxide (SOEC)
Charge carrier	OH^-	H^+	O^{-2}
Reactant	Water	Water	Water, CO_2
Electrolyte	NaOH/KOH	Polymer	Ceramic
Electrode	Raney Ni	Pt, Ir	Ni-Cermet
Temperature	40-90°C	20-150°C	700-1000°C
Efficiency, %	50-65%	50-75%	
Current density (A/cm^2)	0.1-0.4	>1.6	
Advantages	Mature, well stablished technology Non-noble catalysts Long term stability Relative low cost	High current densities High voltage efficiency Rapid system response Compact system design High gas purity	Efficiency up 100% Non noble catalysts High pressure operation
Disadvantages	Low current densities Low pressures Gases crossover Corrosive environment	High cost components Noble catalyst Acidic corrosive environment Commercialization	High temperature Laboratory stage bulky system design No cost information

Polymer electrolyte membrane electrolyzers (PEMELs)

Despite all key advantages, the current high cost of this technology is limiting its widespread application. As described before, operating conditions (acidic medium, 80°C) strongly limit materials choice for cell housing, bipolar plates, electrodes, catalysts and supports[34].

One of the biggest challenges in this technology are the catalysts. Although they do not lead to cell costs at this moment[35], being precious metals, they will be a major issue concerning both, price and shortage, if this technology becomes widely used.

On the cathode side, platinum yields the best catalytic activity for HER, being stable in acid media and reducing conditions. To minimize costs, the amount of Pt has been decreased to a minimum, through dilution in carbon-based supports (Pt-black materials) or minimazed in particle size[36,37]. Besides, complete substitution of Pt has not been achieved, although some promising materials are at research stage, such as the MoS_2 family[38,39], or nickel-based compounds[40,41].

More crucial is the anode catalyst. The acidic environment drives up the OER overpotential and dissolves most non-precious metal oxides. Additionally, the high electric potential, up to 2V, is highly corrosive. In this context, RuO_2 has shown the best catalytic performance, however, it is not stable during oxygen evolution[42]. Because of this, IrO_2 is the preferred OER catalysts for PEMELs. It exhibits high corrosion resistance, and slightly lower activity compared to RuO_2[43]. Unfortunately, iridium is expensive and the rarest metal in Earth's crust, with a production of less than 9 tons a year[44]. Substitution of IrO_2 by a low-cost alternative would thus have a tremendous impact on the future large-scale deployment of this technology.

Cobalt-iron Prussian blue analogues, as was demonstrated previously, is an efficient and fast catalysts for OER[45,46]. It is also stable and active in a large pH

range, between 2 and 11, and, therefore, it shows all requirements to be incorporated in a PEMEL. The only drawback is its low electronic conductivity. This can be remediated by incorporation of a proper electron-conductive support. CoHFe has been deposited on carbon allotropes[47], but carbon is unsuitable for PEMEL anodes, due to carbon corrosion at potentials higher than 0.6 V (vs. RHE)[48], especially above 60°C. Composites of CoHFe and TiO_2 were recently prepared and characterized[49] but not interrogated for their OER activity.

In this chapter, we will report the first interfacing of CoHFe nanoparticles on a conductive oxide for PEMEL anode implementation. Antimony-doped tin oxide (ATO) has recently been investigated as a carbon-free and corrosion-resistant support for platinum particles at the cathode of PEM fuel cells, and as a stable support for IrO_2 at the anode of PEM electrolyzers[50,51,52,53]. The CoHFe-ATO composite catalyst shows promising activity and stability in typical PEMEL operating conditions. Available data, though, indicates that the ATO stability is limited to low anode potential (<2.0V vs. RHE). Improved electrode morphology and catalyst-support interface are still needed to close the gap with costly state-of-the-art IrO_2 anodes.

3.2   Result and discussion

3.2.1. Hydrogen from seawater.

In order to advance towards seawater splitting, we decided to design and build a seawater electrolysis device based on CoHFe. The original idea was a membrane-less prototype that, ultimately, could be released in the sea to produce hydrogen floating autonomously, and powered by photovoltaic energy.

Our first task was the optimization of the anodes, as we understood would be the limiting part. Afterwards, the relation between cathode/anode areas, and the influence of their separation distance. Finally, we also need to pay attention to chlorine evolution in the anode, as by-product. This is interesting from a commercial point of view, due to the industrial impact of the chlor-alkali industry.

I.   Lab-scale experiments.

Taking into account the maximum current density observed on a 2D geometry for these materials (4-5mA/cm^2), our strategy to get higher current densities in hydrogen production was to increase the anode surface area, at minimum volume increase. We tested the deposition of the catalyst (Nano-CoHFe) with different techniques, on highly porous supports of P-doped and Sb-doped Si. Silicon wafers were made porous by anodization. Then, the porous silicon surface was oxidized in order to passivate it. The Si/SiO_2 supports were coated with FTO through spray electrolysis procedure to enhance surface conductivity. For initial tests, the electrodes were dip-coated with Nano-CoHFe.

P-doped Si/SiO_2 waffers coated with FTO and CoHFe nanoparticles were found to give the best OER performance as supported by LSV data (Figure 3.2.1). Better

onset overpotential, and significantly better current densities were found in analogous experiments.
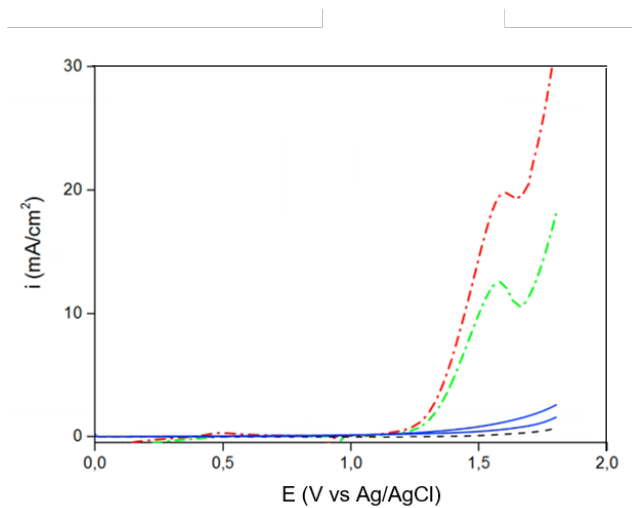

Figure 3.2.1 *Linear sweep voltammetry of P-Si/FTO/Nano-CoHFe (red line), Sb-Si/FTO/Nano-CoHFe (green), bare P-Si/FTO (blue) and bare Sb-Si/FTO(black) in seawater at 50 mV/s.*

With respect to the cathode, we tested different systems: Pt mesh, Ni foam, stainless steel mesh, stainless steel foam, and carbon felt. The latter was pre-treated by annealing at 450ºC. With the exception of Pt and carbon felt, all other cathodes suffered strong corrosion and decomposition processes, once submerged in seawater. For the electrolyzer design, Pt was discarded in terms of cost, so carbon felt was chosen as cathode material. It is a black highly porous foam-like material made of carbon fibers, used at industrial level as a heat and friction insulator. It is highly resistant and low cost ($800/13Kg).

Once both electrodes were selected, we determined the optimum anode/cathode surface ratio to maximize HER. For that propose, we tested the performance of a 1 cm^3 carbon felt cathode, when combined with several 1cm^2 anodes in a tap. The highest performance was obtained for an anode/cathode ratio of 4, taking into account their geometrical surface (Figure 3.2.3).
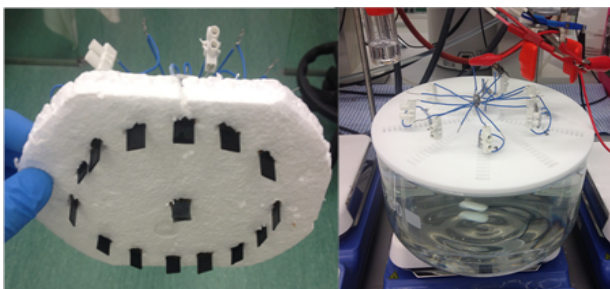
Figure 3.2.2 *Experiment of optimization of the cathode/anode surface ratio.*
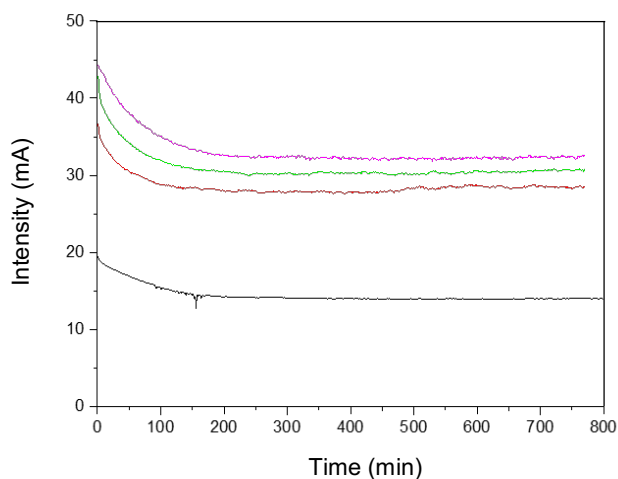
Figure 3.2.3 *Chronoamperometry in seawater at 2V in two electrodes configuration for anode:cathode surface ratios of 1cm^2/1cm^3 (black), 2cm^2/1cm^3 (red), 3cm^2/1cm^3 (green) and 4cm^2/1cm^3 (pink)*

According to these results, we found out the optimum ratio was 4 cm^2 of anode per 1cm^3 of cathode, reaching 8 mA/cm^2 for hydrogen evolution. We observed little, if any, influence on the current data depending on the distance between electrodes. For instance, identical current was found in the 1-22 cm range

(maximum diameter of our recipient). This indicated that the anode/cathode distance does not affect the system's performance, probably due to the high conductivity of seawater.

When analyzing the gas products, we found quantitative hydrogen production at the cathode (Figure 3.2.5). On the anode, a mixture of oxygen and chlorine was produced. We found that the O_2/Cl_2 ratio depends on the total applied potential. The reaction is almost quantitative towards OER at low potentials, and the ratio changes as potential is increased (Figure 3.2.4). At potentials over 3V, Cl_2 is the major product. This trend can be attributed to the fact that the chloride oxidation reaction (Eq. 2.5) requires less electrons than the water oxidation reaction (Eq. 2.3). Hence, although the latter presents a lower thermodynamic potential, the chlorine production is kinetically favored.
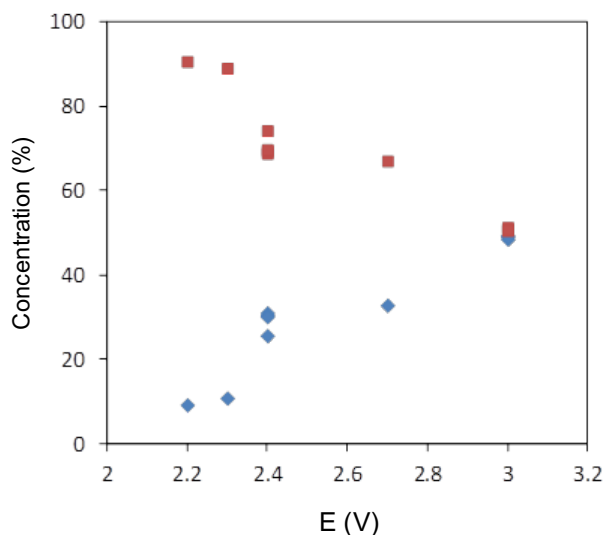
Figure 3.2.4 *Oxygen (red)/chlorine (blue) rate in gases produced at the anode at different potentials. Two electrodes configuration.*
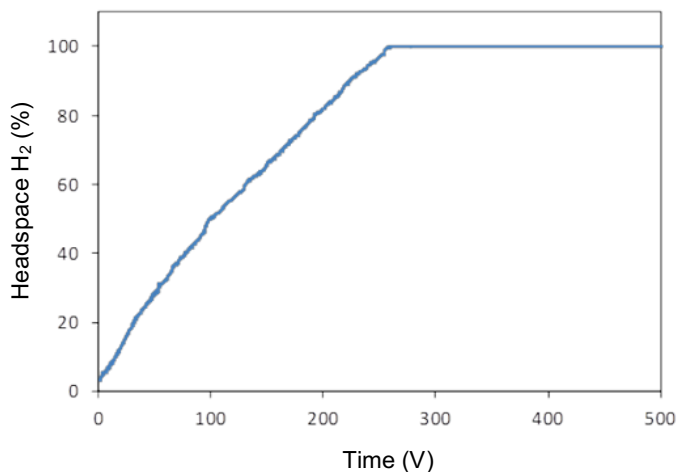
Figure 3.2.5 *Hydrogen evolution in headspace by time.*

II.   Prototype design and construction.

The next step was to design and build a pilot-scale electrolyzer with the basic parameters extracted from our electrode optimization.

The cathode consisted of a central graphite rod with a sheet of carbon felt wrapped around it (Figure 3.2.6a), to be placed below a glass funnel as collector for the hydrogen outlet stream.
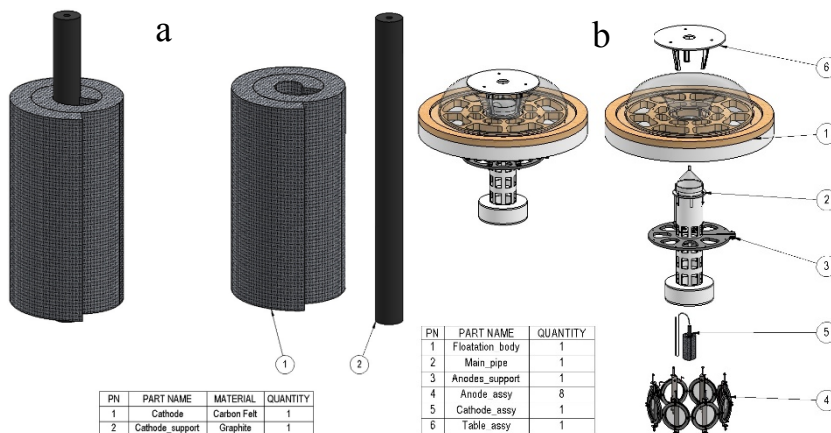
Figure 3.2.6 *Scheme of cathode (a)and cathode place (b)*

To ensure and regulate flotation, a foam was placed under the dome. A sand deposit at the bottom of the cathode central cylinder was included to allow for device weight control, according to operation requirements (Figure 3.2.6.b number 1,2).

In the anode side, titanium cylindrical pieces (Figure 3.2.7a number 2) were used to hold the anodes, made from 10 cm diameter circular Si wafers, coated with FTO, and decorated with Nano-CoFe. The electrodes were sandwiched in a plastic frame to keep electrical connections insulated from seawater (Figure 3.2.7a). These electrodes were placed surrounding the central cathode (Figure3.2.6b number 4). In Figure 3.2.8 the final design is shown, which could

PN	PART NAME	MATERIAL	QUANTITY
1	Anode	Si/SiO2/FTO	1
2	Anode_connection	Ti	1
3	Anode_support	PVC	1
4	Back_support	HDPE	1
5	Front_support	HDPE	1
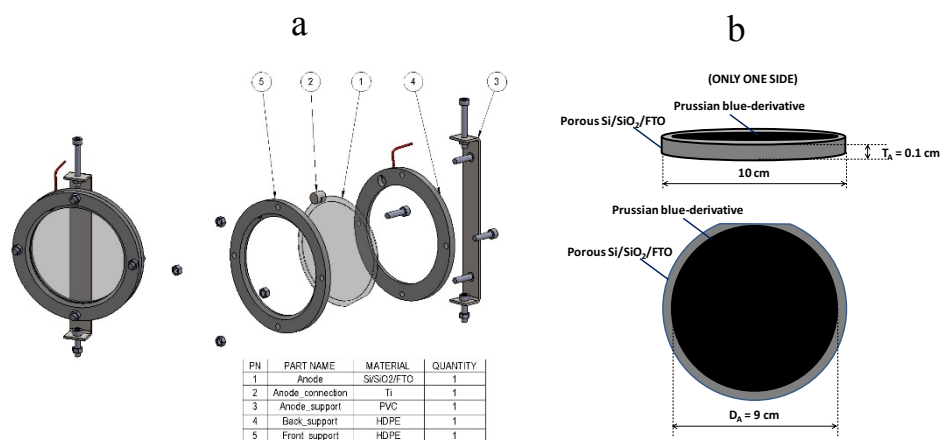
Figure 3.2.7 Scheme anode wafers (b) and its support (a)
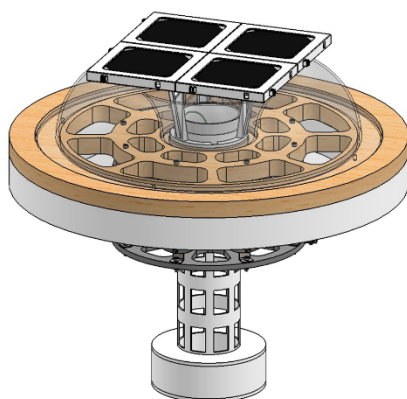
Figure 3.2.8 Final design of the prototype

be ideally powered by solar energy.

A glass dome was fixed over the anodes to collect oxidation gas products, mainly O_2 and Cl_2 (Figure 3.2.9) All welding points and electrical connections were glued with resin to assure electrical insulation.

PN	PART NAME	MATERIAL	QUANTITY
1	Dome	Glass	1
2	Floatation_base	Wood	1
3	Floatation_ring	LDPS	1
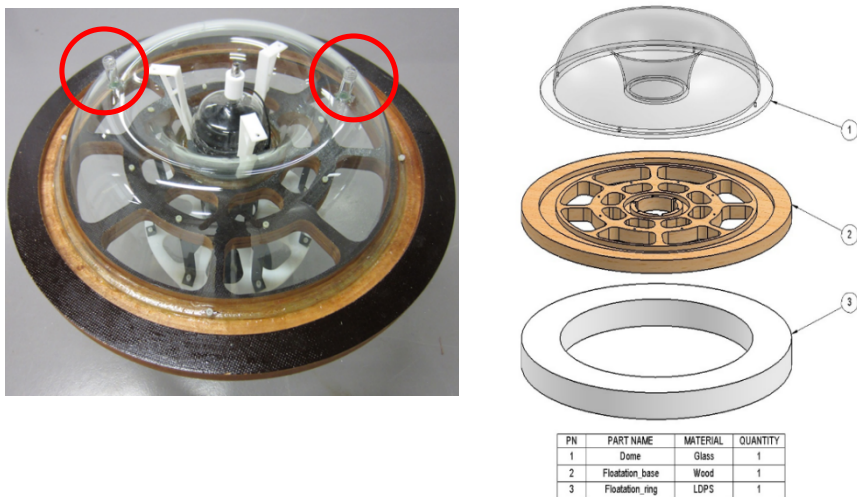
Figure 3.2.9 *Detail of the glass dome with gases outlet (red circles)*

III.   Test and validation of the electrolyzer.

The test and validation stage of the seawater electrolyzer was carried out with a power supply. Gases were collected from both, anode and cathode compartments, as shown in the next Figure 3.2.10.

Nitrogen was used as carrier gas to push out oxygen and chlorine mixture in the anode side, to be analyzed *ex situ*. A hydrogen electrochemical sensor was placed at the cathode exit to detect hydrogen production *in situ.*

Choronoamperometries were carried out applying different potentials (Figure 3.2.12) with the electrolyzer floating on a 1000 L recipient, full of sea water. Recirculation system (5L/h) was incorporated. In Figure 3.2.11, we present a photograph of a real measurements disposition.
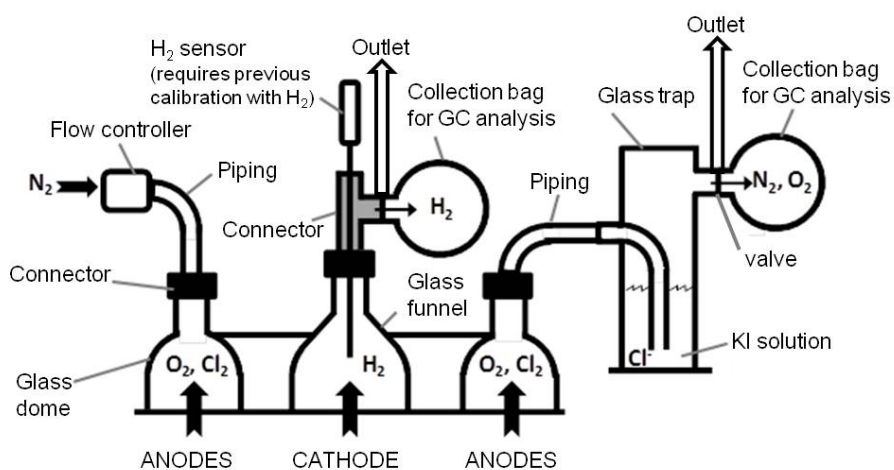
Figure 3.2.10 *Scheme of set-up for the collection of the gases*
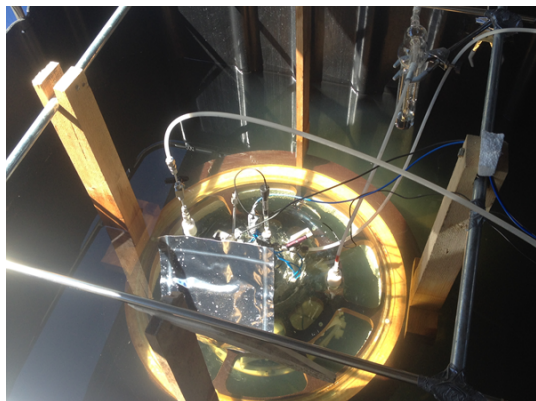
Figure 3.2.11 *Prototype immerse into a seawater tank for inline gases collection*
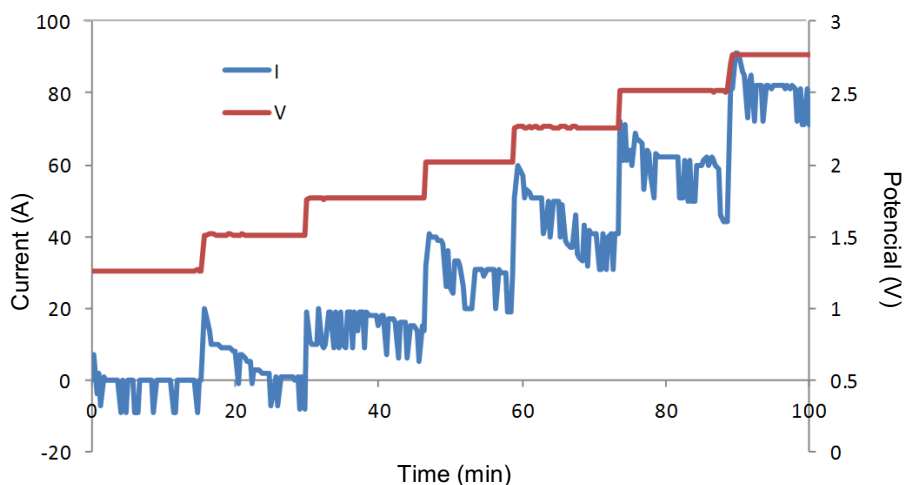
Figure 3.2.12 *Amperometry at different potentials of prototype. Intensity (red) and voltage (blue).*

During these experiments, we observed much lower current densities ($0.080mA/cm^2$ at 2.7V) than expected. Despite many efforts, we could not identify the origin of these low currents.

From our observations, the most plausible reason must be related to the configuration or design of the prototype. The same electrodes, extracted from the prototype, and used in a smaller laboratory recipient promoted better currents, around 0.5 mA/cm^2 but far away from the expected results. Even a single wafer

led to 0.6 mA/cm^2 after 60 min at 2.7V, in a 5L-tank, which was a current comparable to that obtained with 8 wafers in the prototype (Figure 3.2.13). In fact, the larger the total anode area was used, the lower current density was obtained.
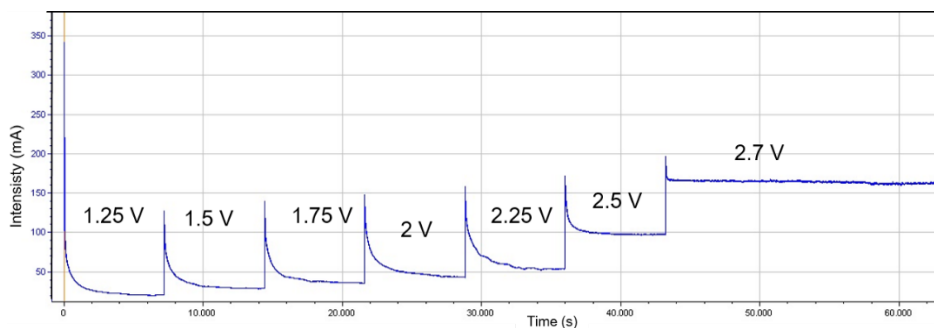
Figure 3.2.13 Chronoamperometry at different voltage in lab scale

Since electrode composition is the same, we assign the differences to: (i) poor stirring and water recirculation in the larger recipient; (ii) high resistance of the electrical connections in the prototype and certain corrosion degree due to incomplete insulation; (iii) poor gas evacuation in the larger recipient due to large volume of the dome; (iv) precipitation of salts on the electrodes, diminishing total surface, or concentration of species modifying the seawater conditions at the proximity of the electrodes; (v) non-proportional scaling of CoHFe nanoparticles deposition method on large areas.

IV. *General considerations and conclusions*

We have designed and built a complete electrolyzer prototype able to work with seawater. Our simple design is a floating device, and extracts pure hydrogen from water when applying a potential difference between cathode and anode in the 2.3– 4 V range.

Under 2.7 V difference, this electrolyzer produces 0.0334 NL of H_2 per hour per cm^2 in the cathode. This production rate is far from commercial PEM electrolyzers (0.28-0.85 NL of H_2 per hour per cm^2)[54], but taking into account the simple design, the readily available feedstock (seawater), and the long term stability of our device, based on cheap and widely available raw materials and able to operate under room temperature and atmospheric pressure inexpensive raw materials, the economic value of our prototype is still unclear.

On a final note, the chloride production may be an interesting commercial opportunity. Chlor-alkali industry is in the search for novel chlorine production technologies, and our catalyst has demonstrated to be stable and robust during oxygen production, but also during chlorine production. This possible application is also under study.

3.2.2. Proton exchange membrane water electrolysis.

Nano-CoHFe supported on Sb-doped SnO$_2$ as a promising non-noble anode catalyst for PEMEL.

I.   Optimization of the CoHFe/ATO phase

As mentioned before, the poor electrical conductivity of CoHFe nanoparticles (and PBA in general) requires the use of a conducting support for its implementation in a PEMEL cell. First task was to determine the optimal catalyst/ATO rate. Homogeneous mixtures were obtained by sonication of a suspension of both materials Np-CoHFe and ATO (CoHFe@ATO from now) in the desired ratio overnight (typically 20h) . To test the catalytic activity in OER, Nafion inks of these mixtures were deposited on a glassy carbon electrode to carry out linear sweep voltammetry experiments in a rotating disk electrode (RDE). Catalyst loading was 257 µg/cm^2. No influence of time deposition was found as of 12h.
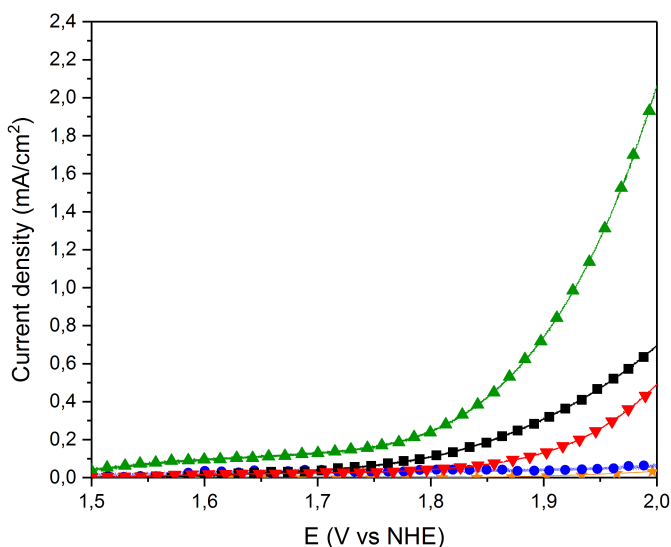
Figure 3.2.14 *Linear sweep voltammetry plot of 9%CoHFe@ATO (blue), 17%CoHFe@ATO (black), 38%CoHFe@ATO (green), 44%CoHFe@ATO (red) and ATO (orange)*

As observed in Figure 3.2.14, the highest current density was found for the 38% Nano-CoHFe content in ATO, which achieved 2.1 mA/cm^2. So, this catalyst was chosen for further experiments.
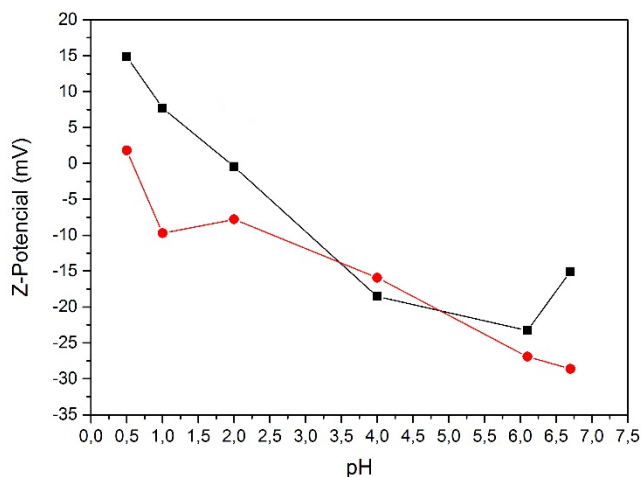
Figure 3.2.15 *Z-potencial values for Nano-CoFe (black) and ATO (red)*

With the intention to enhance the catalytic activity, Z-potencial measurements were done. It is well known that Z-potencial, which is related to pH, can have a strong influence on the electrostatic interaction between particles as long as they have different surface charge depending on the proton concentration. We found that the highest difference in z-potencial betweem catalyst and ATO support was reached at pH = 1.2 and 6.2 (Figure 3.2.15). However, when the mixing was repeated at these pH values, we did not observe better electrochemical performance. So, we kept the standard procedure in MilliQ water.

II. Structure and morphology of Nano-CoHFe, ATO tubes and 38%CoHFe@ATO

The morphology of ATO was evaluated by electron microscopies. The FE-SEM micrographs shown in Figure 3.2.17 indicate the formation of fiber-in-tube structures with outer diameter of ca 170 nm. The outer surface of the tubes is homogeneously covered with grains, having an average diameter of 15 nm (Figure 3.2.16). The fiber-in-tube morphology can be ascribed to the inhibition effect of the particle growth produced by the presence of antimony[55,56].
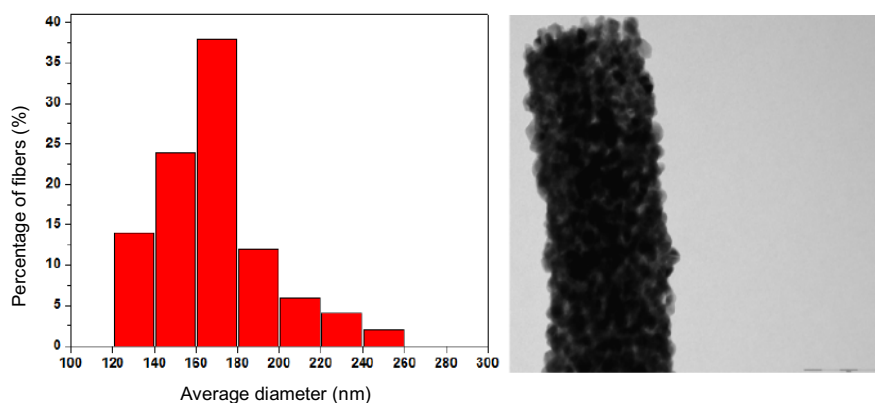
Figure 3.2.16 *Diagram showing the distribution of ATO tube diameters (left) analyzed from SEM micrographs (right).*
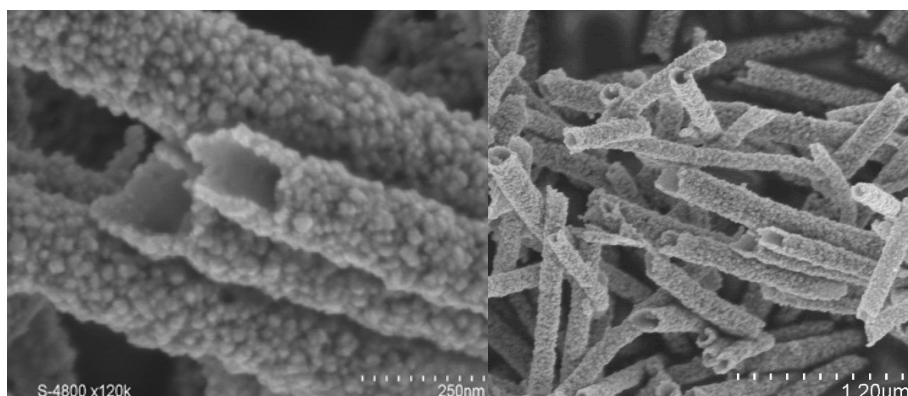
Figure 3.2.17 *FE-SEM micrograph of ATO tubes. The fibre-in-tube structure is best seen for tubes that are oriented nearly normal to the image plane, as for example on the lower right handside corner.*

The crystallinity of the ATO tubes was revealed by XRD (Figure 3.2.18) with all diffraction peaks corresponding to the rutile SnO_2 structure. No diffraction peaks related to separate phases containing antimony were detected. The SnO_2 crystallite size calculated using the Scherrer equation was 16.5 nm, in agreement with TEM observations.
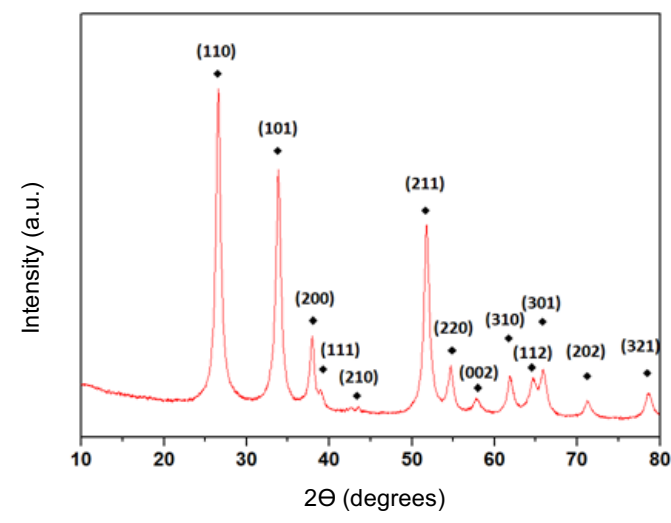
Figure 3.2.18 *XRD of ATO. Indexes for the rutile structure of SnO_2 rutile phase indicated.*

The nitrogen sorption isotherms showed a hysteresis in the relative pressure range of 0.7-1.0 (type-IV isotherms), which is typical of mesoporous materials (Figure 3.2.19). The specific surface area of ATO calculated by the BET equation was 35 m^2/gr. The enhanced surface area compared to SnO_2 materials with lower Sb content can be attributed to smaller grain size and more hollow structure[57].
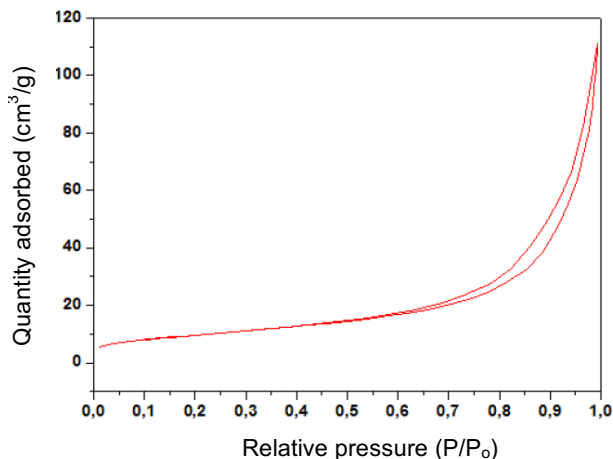
Figure 3.2.19 *Nitrogen sorption isotherm of ATO tubes*

38%CoHFe@ATO morphology and structure was investigated in detail. Figure 3.2.20 shows a high magnification TEM image, revealing the partial coverage of the outer surface of ATO tubes by CoHFe particles (light grey). Due to the transparency of CoHFe with TEM, CoHFe particles located on top the ATO tube may not all be visible. Also, the possible presence of CoHFe inside the ATO tubes cannot be assessed here. While some CoHFe particles seem to be loosely connected to the ATO tubes. FT-IR analyses presented later support a modified electronic state for all CoHFe particles in 38%CoHFe@ATO catalyst due to the ATO support, implying that all CoHFe particles are electrically connected to the support.
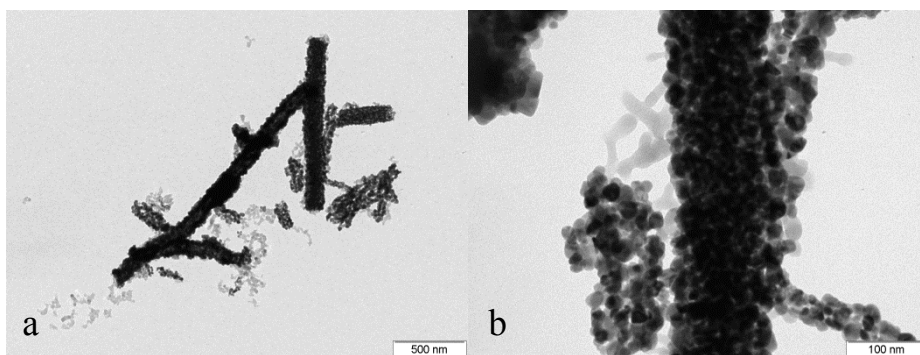
Figure 3.2.20 *Lower (a) and higher (b) magnification TEM micrograph of 38%CoHFe@ ATO catalyst*

The XRD pattern of 38%CoHFe@ATO (Figure 3.2.21 blue line) reveals the most intense peaks of the SnO_2 rutile structure ($2\theta = 27°, 34°, 38°$, see Figure 3.2.18), with minor peaks assigned to the four most intense peaks for pure CoHFe (Figure 21 red line). A slight increase of the peak positions corresponding to CoHFe in 38%CoHFe@ATO relative to pure CoHFe reveals a decreased interplanar distance (Bragg's law), possibly due to a spin transition of Co and Fe ions between pure CoHFe and 38%CoHFe@ATO.
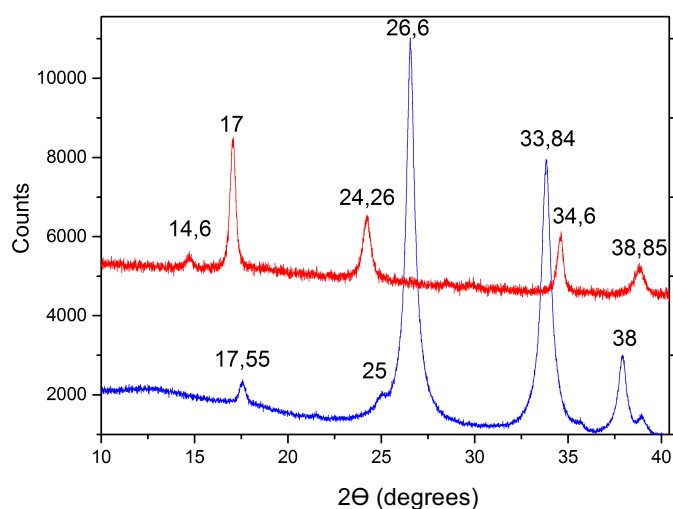
Figure 3.2.21 XRD of fresh 38%CoHFe@ATO (blue) and Nano-CoHFe (red)

A charge transfer mechanism between CoHFe and TiO_2 anatase was recently reported[58,59]. The study concluded that TiO_2 induced a charge transfer spin transition of CoHFe from $Co^{II}_{(HS)}$-NC-$Fe^{III}_{(LS)}$ to $Co^{III}_{(LS)}$-NC-$Fe^{II}_{(LS)}$, resulting in a shortened Co-N bond and decreased unit cell parameter (XRD) from 10.34 Å for CoHFe particles to 10.07 Å for the CoHFe@TiO_2 composite[59]. Decrease of the unit cell dimension as a result of a change of oxidation state from Co^{II} to Co^{III} is well known for pure CoHFe compounds, with the various Co and Fe oxidation states being controlled by the Co:Fe ratio during synthesis[64].

In order to further investigate whether this charge transfer transition also occurred for 38%CoHFe@ATO, the electronic state and coordination of Fe and Co ions were analyzed by FT-IR spectroscopy (Figure 3.2.22). The vibration mode at 2170 cm^{-1} can be assigned to Co^{II}-NC-Fe^{III} bridges (2156-2166 cm^{-1})[60] and Co^{III}-NC-Fe^{III} bridges (2190 cm^{-1}). The vibration mode at 2140 cm^{-1} can be assigned to Co^{III}-NC-Fe^{II} bridges (2120-2130 cm^{-1}). The shoulder around 2080-2110 cm^{-1} can be assigned to Co^{II}-NC-Fe^{II} bridges or to non-bridging cyanides on the surface or at other defective sites[64,61]. No vibration modes for pure ATO in the region 1000-3000 cm^{-1} are expected[62,63]. For 38%CoHFe@ATO (Figure 3.2.22, blue line), a single band is observed at 2100 cm^{-1}, overlapping with the shoulder observed on the spectrum of CoHFe alone. This clear spectral change unambiguously demonstrates a long-range electronic effect of ATO on CoHFe, since they were separately synthesized before being mixed. Red shift from 2150 to 2100 cm^{-1} of the FT-IR spectra from CoHFe to 38%CoHFe@ATO perfectly matches the spectroelectrochemical red shift observed when electrochemically cycling CoHFe films from 0.9 to 0.0V vs NHE ($Co_3^{II}[Fe^{III}(CN)_6]_2$ to $K_2Co_3^{II}[Fe^{II}(CN)_6]_2$ conversion)[60].
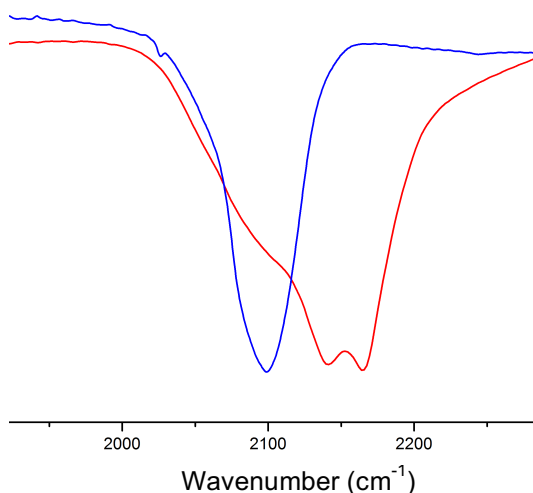
Figure 3.2.22 *Infrared spectra of catalyts as prepared (blue) and Nano-CoHFe starting material (red)*

To sum up, XRD and FT-IR show that the CoHFe nanoparticles were not denaturated during the suspension procedure (XRD pattern typical for CoHFe) but the unit cell parameter was slightly decreased and the FT-IR was red-shifted, both changes being explained by spin transitions of different Co-NC-Fe electronic states (including Fe^{III} and Co^{III} existing in pure CoHFe) to a single band assigned to a Co^{II}-NC-Fe^{II} vibration mode in 38%CoHFe@ATO.

III.   *Electrochemical characterization in liquid electrolyte*

We performed cyclic voltammetry measurements on this catalyst in order to investigate its electrochemical interface, including the presence of redox peaks and the magnitude of the capacitive current (Figure 3.2.23). In both graphs, a synergy effect was found. In graph b, Co^{III}/Co^{II} reversible peak from 0.45V up to 0.90V[64] is maintained in the catalyst but both peaks are slightly shifted to lower potentials. Possibly due to the presence of ATO and the induced charge transfer discussed previously. Low pH electrolytes values (pH=1) provoke a shift in the oxidation potencial of CoHFe[65]. Figure 3.2.23b also shows that the electrochemical signal for 38%CoHFe@ATO results from the superposition of the capacitive current of the ATO support and the redox peak characteristic for CoHFe. The fact that the double layer current of 38%CoHFe@ATO is as high as that of ATO alone indicates that the whole ATO surface is not blocked by the CoHFe particles. Combined with the FT-IR analyses showing all CoHFe particles are in electric contact with ATO this implies in turn that the CoHFe content in 38%CoHFe@ATO is sufficiently low to avoid the formation of a thick layer of CoHFe particles on ATO tubes that could electrically insulate the outer CoHFe particles from the conductive ATO support. At higher CoHFe contents this results in a decreased OER activity of the composite material. Figure 3.2.23a shows a significant electro catalytic wave above 1.8V.
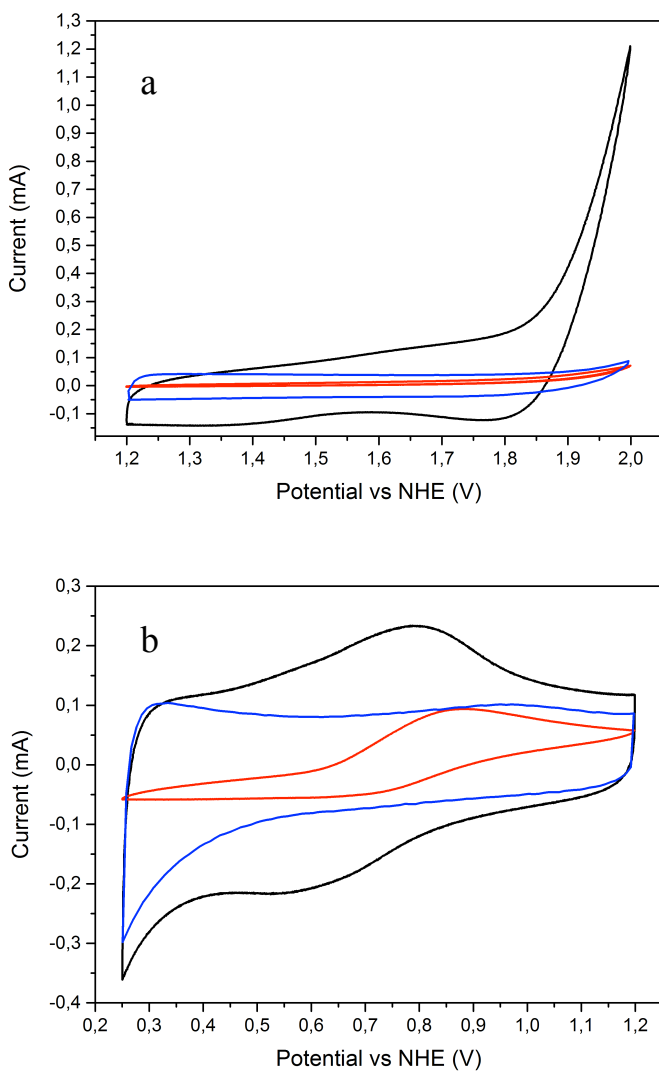
Figure 3.2.23 *Cyclic voltammagram of catalyst (black), ATO (blue) and Np-CoHFe (red)*

IV. Investigation of 38%CoHFe@ATO in PEMEL.

To perform PEMEL experiments, the first step was the membrane electrode assembly (MEA) fabrication. The anode catalyst layer deposited on Teflon glass-fibre by spray of a Nafion ink to be transferred onto Nafion membrane *via* hot pressing. In a second step, the catalytic cathode gas diffusion layer decorated with Pt particles supported on carbon was also hot pressed onto the opposite side of the Nafion membrane (Figure 3.2.24). Then, the MEA is sandwiched in the cell between two gaskets and a Ti-sintered mesh as gas diffusion layer in the anode side. MEAs were assembled in a square 6.25 cm^2 active-area single cell, having Ti- and Au–coated stainless steel anode and cathode plates, respectively (Figure 3.2.25)
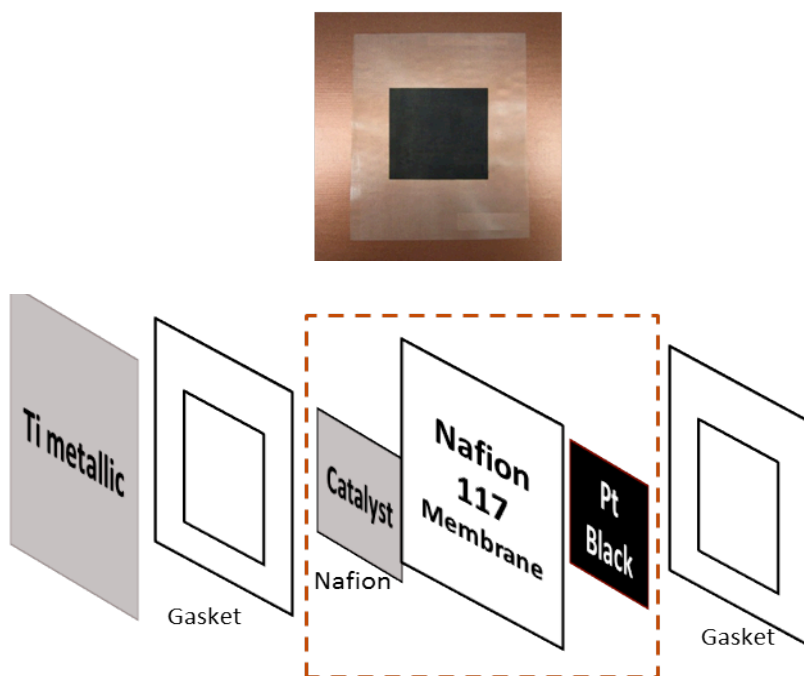
Figure 3.2.24 *Photography of a real MEAS with 38%CoHFe@ ATO (top).
Basic outline of the heart of the cell with the MEA in the core (bottom)*
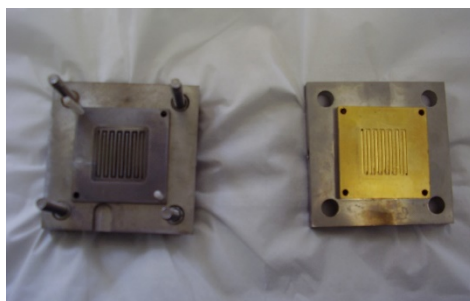
Figure 3.2.25 *Polymer electrolyte cell unit open it. Cathode side (left) made of titanium, anode side is made of stainless steel plate coated with gold*

The effect of the Nafion[®] content in the ink formulation was first optimized. Contents lower than 20wt.% were insufficient to allow the transfer of the sprayed catalyst film onto the Nafion membrane by hot pressing, while contents higher than 30 wt.% lead to overly high cell ohmic resistance (higher than 800mΩ) during break-in of the PEMEL, as measured by electrochemical impedance spectroscopy (EIS). To get successful measurements, cell resistance at 80ºC after hydration overnight should be less than 100mΩ.

Following this initial screening, the catalyst 38%CoHFe@ATO was dispersed with 20 and 30wt% of Nafion and isopropanol (see experimental section), sprayed and transferred onto a Nafion 115 membrane at a catalyst loading of 3mg/cm^2. For 20% and 30% resistance were 208mΩ and 200mΩ . Once the cell is assembled, it is connected to the test bench (Figure. 3.2.26) where potencial or current is applied while pumped water at 80ªC circulates through the anode side.

Following the break-in procedure, the initial polarisation curve was recorded (Figure 3.2.27a). The onset potential is ca 1.7V, in line with the RDE results. To initially investigate the stability at a higher current density, the cell voltage was fixed at 2V for 22 h and the current density recorded (Figure 3.2.27c).
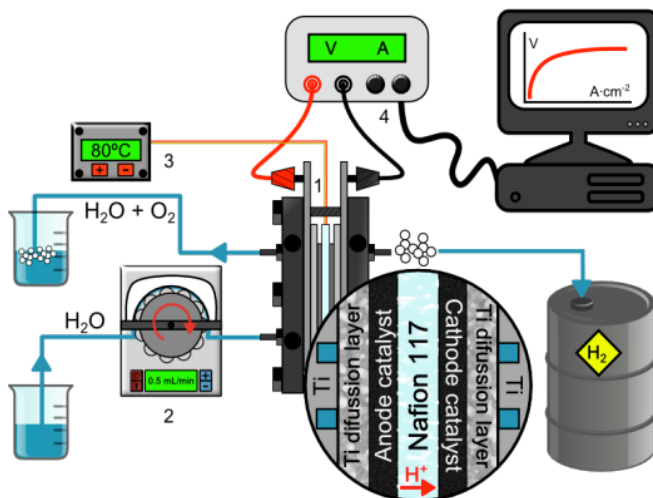
Figure 3.2.26 Scheme of PEM electrolyser system: electrochemical reaction cell (1), peristaltic pump and water reservoir (2), temperature controller (3) and potenciostate (4) (adapted from 39)

A loss of only 10 % of the current density is observed during 22 h, attesting the relative stability of the anode catalyst in acidic medium even at such high electrochemical potential. Moreover, the loss may be assigned to either CoHFe or to the ATO support. While the latter has been demonstrated to be stable in anodic conditions in PEMEL up to 1.8V, the operation over a long duration at such a high voltage has been rarely investigated. To go further in the potential-dependence of this instability, we gradually increased the cell potential from 1.5V to 2V, staying 4h at each potential, and completing the experiment with a 2.2V potentiostatic control for 20h (Figure 3.2.27b). The current density is either constant or slowly increases at each potential step up to 1.9V, shows a small decrease during the 4h step at 2V and a dramatic decrease during the next step at 2.2V. In order to understand the origin of this instability at potentials above 2V, we characterized the ATO support and of the CoHFe nanoparticles post-electrolysis.
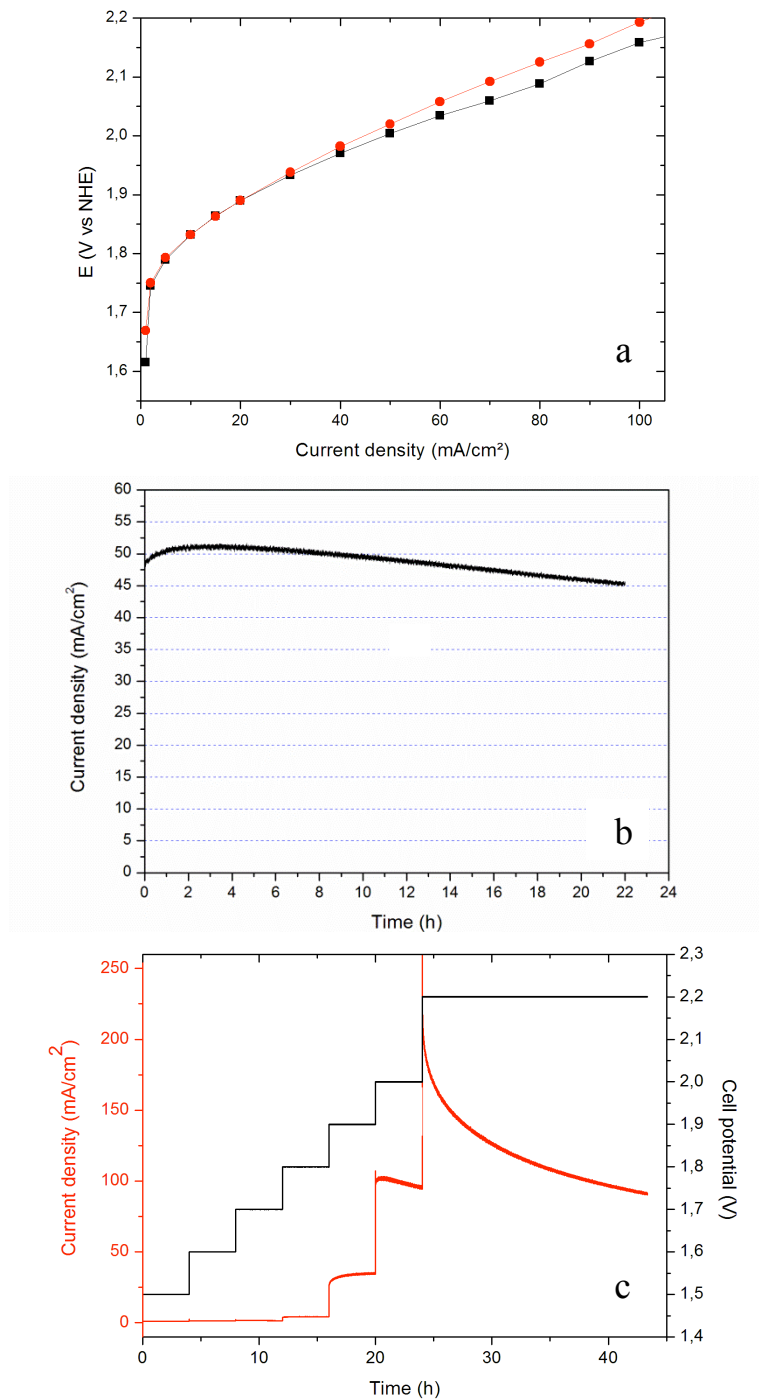
Figure 3.2.27 *PEMEL initial polarization curves before and after the CA at 2V (a), CA at 2V (b) and CA for 4h at each potential (c). MEA was conditioned 4h at 1.6V before starting the measurement with 3mg/cm² of 38%CoHFe@ATO*

V.   *Stability of 38%CoHFe@ATO in PEMEL.*

The infrared spectra (Figure 3.2.28) showed different bands from 2025 cm^{-1} up to 2180cm^{-1} proving the presence of CoHFe in catalyst postmortem. In the catalyst as prepared spectra, the main band is centered at 2100cm^{-1}, typical of Co^{II}-CN-Fe^{II} (HS), in a Co/Fe rate 1.5, with a small peak at lower wavenumbers (2025 cm^{-1}) assigned to Co^{III}-CN-Fe^{II} (LS). Thus, the relative peak intensity changes during the electrocatalityc process, indicating a change in the oxidation state.
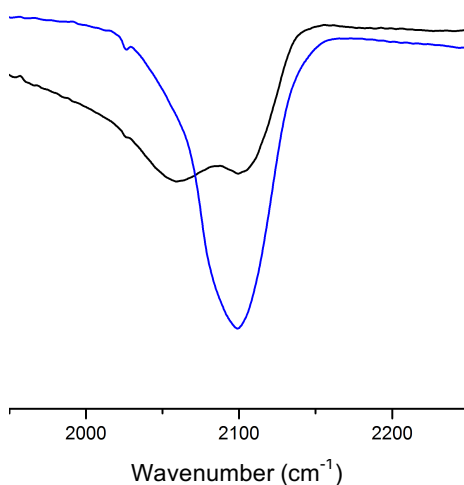
Figure 3.2.28 *Catalyst FT-IR spectra as prepared (blue) and post-mortem (black)*

The presence of CoHFe is also proved by TEM analysis (Figure 3.2.29) as the more transparent material due to the lower density of PBAs compared with ATO. Main difference between fresh and post-morten images (Figure 3.2.20 *vs* 3.2.29) is that, some support fibers become shorter and less decorated with catalyst, which could be related to the poor stability observed in the steady state chronoamperometry experiments.
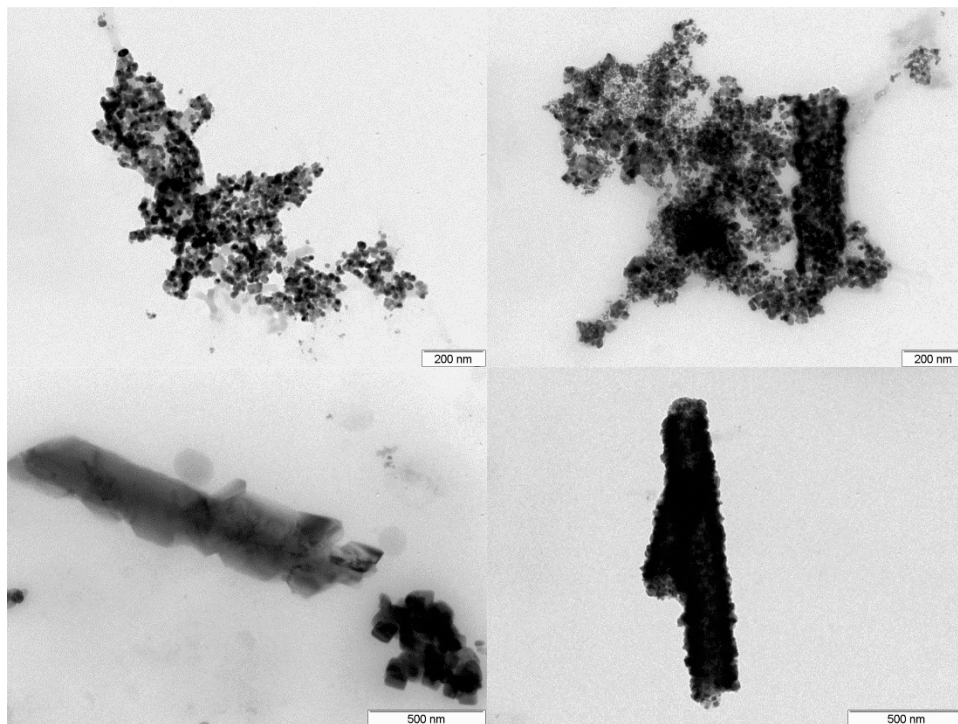
Figure 3.2.29 *TEM images of post-mortem catalyst*

In order to check whether the composition of the catalyst before and after the PEMEL experiments remains the same, energy-dispersive X-ray spectra were recorded. The Co/Fe ratio strongly decreases, from 5.45 to 1.88, supporting the idea that a change in the PBA structure takes place during water electrolysis. Still, the stoichiometry obtained is typical of the PBA.

The electrochemical stability of ATO was investigated outside the PEMEL by measuring the amount of Sb and Sn leached during an electrochemical corrosion test in acidic electrolyte at 80°C. An ATO-coated Ti electrode was potentiostatically controlled at open circuit potentials (1.9, 2.0 or 2.2V vs. NHE) for 4h, and the amount of metal leached out in the electrolyte was measured with ICP-MS (Table 3.2.1).

Table 3.2.1 *ICP-MS data of the amount of elements leached during corrosion test of ATO at 80°C in 0.1M H_2SO_4.*

Potential (V vs NHE)	Sn loss (%)	Sb loss (%)	Average Sb content in corroded material/at %
OCP	$< 10^{-5}$	$< 10^{-4}$	10.0
1.9	0.14	7.7	9.5
2.0	0.16	8.5	9.4
2.2	22.6	52.7	6.0

Sb and Sn concentrations in electrolyte measured after immersion of ATO at OCP were negligible (*e.g.* the leaching is entirely associated with applied high electrochemical potential). A significant leaching of Sn and Sb was measured after 4h at a potential of 1.9 or 2.0V vs NHE, while a massive leaching of Sn and even more Sb is quantified after 4h at 2.2 V vs. NHE. These results suggest that the main degradation mechanism leading to the decrease in current density observed above 2V in PEMEL with the 38%CoHFe@ATO should be the electrochemical corrosion of the ATO support. The preferential loss of Sb (Table 3.2.1) probably reduces the electronic conductivity of ATO, especially on the surface. This would electrically insulate the CoHFe particles from the electron conductive network of the anode layer and, thereby, negatively affect the anode performance, even if CoHFe itself is stable in such conditions. The massive leaching of Sb and Sn could also affect the proton conductivity of the Nafion ionomer in the anode or in the membrane.

The anode based on 38%CoHFe@ATO and subjected to the potentiostatic test at 2V for 20h was also characterized by XRD, FT-IR spectroscopy and TEM. The XRD pattern in Figure 3.2.30 (green curve) does not reveal the characteristic peaks for the pristine crystalline CoHFe structure (see the four minor peaks observed in figure 3.2.30, blue curve), except for the minor peak located at ca 39º. It is therefore difficult to discuss from the post mortem XRD pattern possible electronic or structural changes during the PEMEL operation at 2V on CoHFe.

FT-IR proves more suitable, with Figure 3.2.31 showing the spectrum after the 20h test at 2V (Figure 3.2.31 black curve). It reveals two bands, one located at 2100 cm^{-1} and assigned to Co^{II}-NC-Fe^{II} and the other band, not previously observed on the catalyst powder before electrochemical operation, located at ca 2060 cm^{-1}. FT-IR therefore reveals a new vibration band that was absent in the pristine catalyst powder. The presence of this band at such a low wave number might result from the integration of protons generated during OER inside the CoHFe structure, possibly leading to the reduction of Fe and/or Co cations under OCP conditions for electroneutrality. This new band may also be related to the partial amorphization of CoHFe after the potentiostatic experiment, as revealed by XRD.
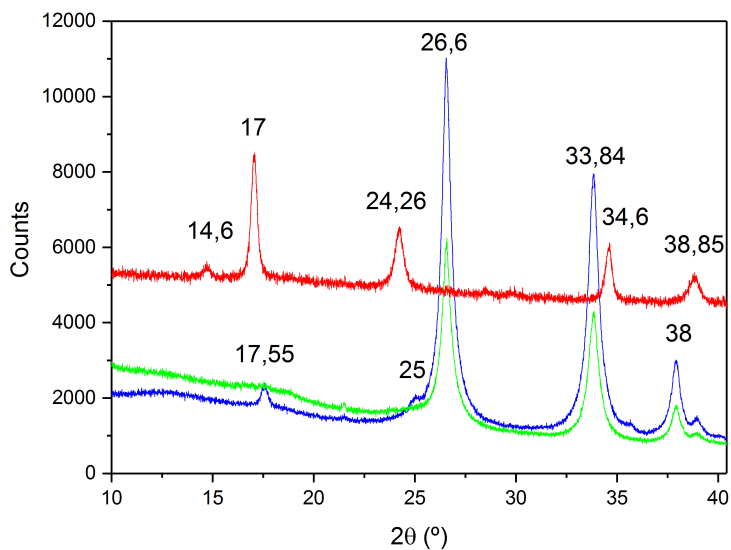
Figure 3.2.30 *XRD pattern of CoHFe nanoparticles (red), catalyts as prepared (blue) and catalyts postmortem after PEMEL test at 1.9V for 20h (green)*
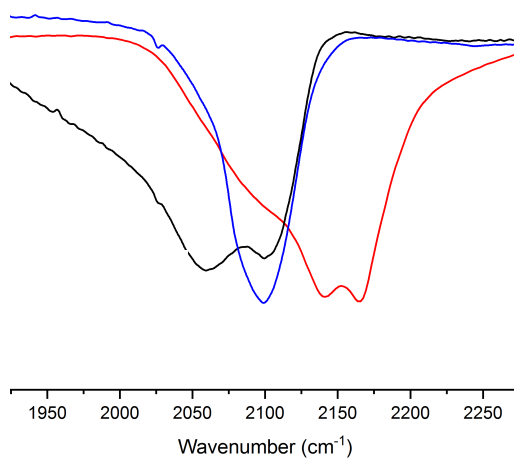
Figure 3.2.31 *FT-IR spectra of CoHFe nanoparticles (red), catalyts as prepared (blue) and catalyts postmortem after PEMEL test at 1.9V for 20h (black)*

3.3   Conclusions.

In summary, first of all, it should be noted that we were able to design and build a full-cell electrolyzer that works with seawater in semi-industrial conditions. Despite the poor performance (in terms of current), we learned many important requirements to go towards real working conditions. Our catalyst were robust working in extremely harsh conditions, to obtain hydrogen and chlorine, both gases of industrial interest. On the other hand, we identified design issues (too large gas reservoir, key importance of stirring, poor scaling of dip coating processing, etc.) that must be re-thought for future designs to both, improve autonomy and assure efficient gas collection.

We have also shown that the incorporation of CoHFe Prussian blue nanoparticles into a PEMEL architecture is a viable strategy with incredible potential, despite being far from the IrO_2 benchmark (1A/1.6V). Currents may increase if the robust CoHFe is combined with a proper conducting support. It is important to note that the architecture we used was originally optimized for the IrO_2 catalysts, after decades of research and development. Our results constitute the first non-IrO2 PEMEL that actually works.

Regarding the apparent instability, we have shown that it comes mainly from the support, whereas the active phase, despite undergoing structural changes (observed previously) remains active including at high potentials (2V) in acid media. From this point of view, it seems reasonable to devote huge efforts towards the use of CoHFe in PEMELs, as a unique opportunity to avoid the use of Platinum group metals.

3.4   Experimental

Electrodes preparation for sea water electrolysis

Silicon electrodes supports preparation (silicon type n, doped with Phosphorus. (Resistivity <0.002 Ω.cm) First cleaning immerse in acetone keep it 5 min in ultrasound, then silicon wafers are keep 20 min immerse in 1:4 HF:Ethanol. Afterwards, anodization process is done. Teflon reactor fitted with Pt mesh is fill with a solution of 20mL H_2O, 2.5 mL HF, 25mgr $KMnO_4$ and 60mgr Na-dodecyl sulfate. Then, 15mA/cm^2 current density is applied for 30 min in a three electrodes configuration with Ag/AgCl as reference electrode. After anodization, washing is done with water and immerse in ethanol. Finally, is dried with nitrogen.[66]

FTO spray deposition, a solution of $SnCl_4$ (0.2M) and 5% of FNH_4 in ethanol is sprayed on a heat SiO_2 porous wafer (450K), pyrolysis took place in silicon surface yielding high conductivity FTO coating.[67]

Dip coating on SiO_2/FTO wafer was done dip-coating overnight into a well stirred Nano-CoFe dispersion of 1mgr/ml and dried on air.

Iodometric tritration chlorine concentrations were measured following a protocol from Occupational Safety and Health Administration (OSHA)[68].

Chronoamperometry in seawater each potential was maintained 15 min.

Materials preparation for PEMWE

CoHFe nanoparticles were prepared by a modified literature protoco[69]. A solution of 0.03M $K_3Fe(CN)_6$ in formamide was quickly added to a formamide solution of 0.02M $Co(NO_3)_2$, forming a dark purple dispersion. The solution was kept under stirring for 2 h. After this time solid was separate from formamide by centrifugation/decantation, later on, solid material was dispersed in deionized

water and centrifuged at 6000 rpm to collect a fine red powder by decantation. This purification process was repeated at least three times. Finally, the CoHFe nanoparticles were dried at 60ºC.

ATO tubes were prepared by electrospinning, as previously reported by us[70]. In summary, 0.1 g SbCl$_3$ (99 %, Sigma-Aldrich) was added to a solution containing 0.78 g SnCl$_2$ (98 %, Sigma-Aldrich) and 0.8 g polyvinylpyrrolidone (PVP, Mw ~ 1,300,000, Sigma-Aldrich) dissolved in a mixture of ethanol (99.8%, Fluka) and N,N-dimethylformamide (DMF, 98 %, Fluka) at a ratio of ethanol to DMF of 1.8. The obtained mixture was stirred overnight and electrospun at room temperature on a rotating drum (Linari Biomedical) using a voltage of 15 kV, a needle-collector distance of 10 cm and a flow rate of 0.3 mL/h. The as-prepared SbCl$_3$-SnCl$_2$/PVP fibers were calcined at 600 °C for 4 h in air with a heating rate of 5°C min^{-1} in order to remove the carrier polymer and to form ATO. The synthesis described above results in 10 at% Sb in SnO$_2$, a composition that was previously shown to result in sufficient electronic conductivity[71]

Polymer exchange membrane water electrolysis

Liquid electrolyte to test the catalytic activity in OER of each catalyst the ink was then prepared with 5 mg of CoHFe@ATO, 440 µL ethanol, 100 µL H2O and 10 µL Nafion solution (5 wt % Nafion dispersed in lower alcohols) and sonicated together for 30 min. An aliquot of 5 µL of the ink was deposited on a glassy carbon electrode of 0.196 cm^2 geometric area. To perform **linear sweep voltammetry** 5 µL of ink were dropped on a rotating disk glassy carbon electrode. Measurements were carry out in a in a three-necked flask at 50mV/s, at 1600 rpm in 0.1M H$_2$SO$_4$ electrolyte. NHE as reference and Pt mesh as a counter electrode.

Cycle voltammetry was done in the same conditions at 100 mV/s without rotation.

Z-potencial were determined by dynamic light scattering with a NanoSZ (Malvern). Measurements were done in a 1mgr/ml water dispersion. pH was fixed with H_2SO_4 (1M) and NaOH (1M) solutions.

Ink preparation and deposition technique for PEMEL anodes.

The catalytic ink for the anode is then prepared by adding simultaneously 38%CoHFe@ATO, Nafion solution (5 wt %, Dupont), 3 mL isopropanol and 1 mL deionized water in a 5 mL vial. For preparing 6.25 cm^2 anodes with a targeted loading of 38%CoHFe@ATO of 3mg/cm^2, the ink comprised 37.5 mg of 38%CoHFe@ATO. With our spray method, circa 50 % of the ink is typically deposited on the active area, the rest being deposited on the outer Teflon-glass fiber fabric frame. The aliquot of Nafion solution to result in 20 wt % dry Nafion to the total mass of solids is 215 µL. The ink is sonicated for 45 min and entirely sprayed with an aerograph (Badger Air-brush, universal®) on a Teflon-glass fibre fabric masked with a second, thicker, Teflon-glass fibre fabric. Both masks were placed on an in-house made heating pad thermostated at 8°C. The exact catalyst loading deposited on the active area is deduced from the weight change of the Teflon sheet before and after the spraying and drying.

Membrane Electrode Assembly (MEA)

The Nafion 115 membrane was first cleaned with 3% H_2O_2 solution at 80°C for 1 h, then 1M H_2SO_4 at 80°C for 1h and finally with deionized water at 80°C for 1 h. The membrane is dried at 80°C in oven and stored in a plastic bag. The anode catalyst layer deposited on Teflon glass-fibre was then transferred onto the membrane *via* hot pressing. The membrane and anode/Teflon sheet were sandwiched between two metallic plates themselves covered by Teflon-glass fibre fabric. The press was heated to 80°C, the metallic plates comprising the anode and membrane introduced in the press, and pressure increased to 8.1 MPa. Then the temperature was increased to 135°C and once reached, the pressure was increased

to 15.7 MPa for 5 min. In a second step, the catalyzed cathode gas diffusion layer (Sigracet 10BC, 0.5 mg Pt cm^{-2}, Baltic Fuel cells) was hot pressed onto the anode-membrane assembly in the same conditions as described above, in order to complete the MEA fabrication.

Break-in procedure is done to condioner the cell. Ones MEA is assembled into the cell water (80ºC) is introduce in both sides, cathode and anode, closed and keep it overnight, then is connected to measurements setup and current of 100mA applied for 24h.

Energy dispersive X-ray spectroscopy was used to analyze metal content of CoHFe PBA and ATO with scanning electron microscope JEOL-JMS400 equipped with an Oxford EDX analyzer (Oxford Instruments).

Table 3.4.1 Metal content in atomic percentage of 38%CoHFe@ATO before and after PEMWE experiments

Element	As prepared		Post-mortem	
	Atomic (%)	*Rate*	*Atomic (%)*	*Rate*
Fe K	0.42	Co/Fe	0.71	Co/Fe
Co K	2.29	5.45	1.34	1.88
Sn L	89.95	Sb/Sn	90.35	Sb/Sn
Sb L	7.34	0.81	7.60	0.084
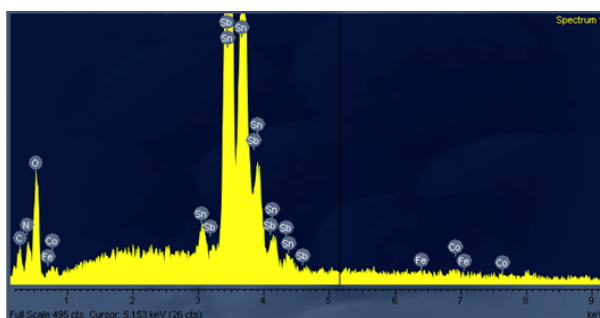
Figure 3.4.1 EDX spectra of 38%CoHFe@ATO as prepared

Leaching experiments were done with 2.7 mg/cm^2 of ATO sprayed on Ti foil. ATO subjected to 4 h of a given potential, then concentration of Sb and Sn in electrolyte was measured.

Methods

Powder X-ray diffraction (PXRD) data were collected on a D8 Advanced series 2Θ/Θ powder diffractometer at room temperature in transmission mode.

FT-IR measurements were carried out on a Thermo Nicolet iS50 spectrometer equipped with a DTGS detector (or MCT if using the N_2 cooled detector), KBr beamsplitter at 4cm^{-1} resolution were collected in absorbance mode.

Scanning electron microscopy: SEM images and EDX spectra were obtained with an Environmental Scanning Electron Microscope JEOL-JMS6400 equipped with an Oxford Instruments X-ray elemental analysis.

Transmission electron microscopy done with JEOL 2011 in standard conditions samples dispersed water/Ethanol in1:1 and dropped in Cu grids.

Electrochemical methods. All electrochemical experiments were performed with a Biologic SP-150 potenciostate, an ALS Ag/AgCl (3.5MKCl) reference electrode and Pt wire or mesh counter electrode. All potentials reported in this manuscript were converted to the NHE reference scale using E(NHE) = E(Ag/AgCl)+0,209 V. Unless otherwise stated , the electrolyte used for linear sweep voltammetry (LSV) and cyclic voltammetry (CV) was prepared H_2SO_4 (0,1M) in MilliQ giving a pH 1 solution.

3.5 References

[1] Granovskii, M.; Dincer, I.; Rosen, M. A. *Journal of Power Sources* **2006**, *159*, 1186.

[2] Marbán, G.; Valdés-Solís, T. *International Journal of Hydrogen Energy* **2007**, *32*, 1625.

[3] Jeremy Rifkin. "The Hydrogen Economy: The Creation of the Worldwide Energy Web and the Redistribution of Power on Earth", *Paperback* , **2003**

[4] International energy agency: http://www.iea.org

[5] Grube, T.; Stolten, D. *BWK* **2010**, *62*, S16.

[6] Grube, T.; Fischedick, M.; Pastowski, A.; Stolten, D. *Chemie Ingenieur Technik* **2009**, *81*, 7, Grube, T.; Fischedick, M.; Pastowski, A.; Stolten, D. *Chemie Ingenieur Technik* **2009**, *81*, 7.

[7] Stolten, D.; Emonts, B.; Grube, T. *BWK* **2008**, *60*, S1.

[8] Ghosh, P.; Emonts, B.; Janßen, H.; Mergel, J.; Stolten, D. *Solar Energy* **2003**, *75*, 469.

[9] Muradov, N.; Veziroğlu, T. *International Journal of Hydrogen Energy* **2005**, *30*, 225.

[10] Ogden, J. M.; Steinbugler, M. M.; Kreutz, T. G. *Journal of Power Sources* **1999**, *79*, 143.

[11] Sørensen, B. *Hydrogen and Fuel Cells: Emerging Technologies and Applications*. Academic Press: **2011**.

[12] Joensen, F.; Rostrup-Nielsen, J. R. *Journal of Power Sources* **2002**, *105*, 195.

[13] Papageorgopoulos, D. C.; de Bruijn, F. A. *Journal of the Electrochemical Society* **2002**, *149*, 5.

[14] Chellappa, A.; Fischer, C.; Thomson, W. *Applied Catalysis A: General* **2002**, *227*, 231.

[15] Springer, T.; Rockward, T.; Zawodzinski, T.; Gottesfeld, S. *Journal of the Electrochemical Society* **2001**, *148*, A11.

[16] Cheng, X.; Shi, Z.; Glass, N.; Zhang, L.; Zhang, J.; Song, D.; Liu, Z.-S.; Wang, H.; Shen, J. *Journal of Power Sources* **2007**, *165*, 739.

[17] Kalamaras, C. M.; Efstathiou, A. M. In *Hydrogen Production Technologies: Current State and Future Developments*, Conference Papers in Science, 2013; Hindawi Publishing Corporation: **2013.**

[18] Tee, S. Y.; Win, K. Y.; Teo, W. S.; Koh, L. D.; Liu, S.; Teng, C. P.; Han, M. Y. *Advanced Science* **2017**.

[19] El-Dessouky, H. T.; Ettouney, H. M. *Fundamentals of Salt Water Desalination*. Elsevier: 2002.

[20] http://www.un.org/en/sections/issues-depth/water/index.html

[21] Raissi, A. T.; Block, D. L. *IEEE Power and Energy Magazine* **2004**, *2*, 40.

[22] Bennett, J. *International Journal of Hydrogen Energy* **1980**, *5*, 401.

[23] Kato, Z.; Sato, M.; Sasaki, Y.; Izumiya, K.; Kumagai, N.; Hashimoto, K. *Electrochimica Acta* **2014**, *116*, 152.

[24] Surendranath, Y.; Dincă, M.; Nocera, D. G. *Journal of the American Chemical Society* **2009**, *131*, 2615.

[25] Dionigi, F.; Reier, T.; Pawolek, Z.; Gliech, M.; Strasser, P. *ChemSusChem* **2016**, *9*, 962.

[26] Bullis, K. *MIT Technology Review* **2008**, *111*, 56.

[27] Schröder, V.; Emonts, B.; Janßen, H.; Schulze, H. P. *Chemical engineering & technology* **2004**, *27*, 847.

[28] Ayers, K. E.; Anderson, E. B.; Capuano, C.; Carter, B.; Dalton, L.; Hanlon, G.; Manco, J.; Niedzwiecki, M. *ECS Transactions* **2010**, *33*, 3.

[29] Medina, P.; Santarelli, M. *International Journal of Hydrogen Energy* **2010**, *35*, 5173.

[30] Onda, K.; Kyakuno, T.; Hattori, K.; Ito, K. *Journal of Power Sources* **2004**, *132*, 64.

[31] E. Funk, J. *International Journal of Hydrogen Energy* **2001**, *26*, 185.

[32] Brisse, A.; Schefold, J.; Zahid, M. *International Journal of Hydrogen Energy* **2008**, *33*, 5375.

[33] Shen, P. K.; Wang, C.-Y.; Jiang, S. P.; Sun, X.; Zhang, J. *Electrochemical Energy: Advanced Materials and Technologies*. CRC Press: 2015. 573-575

[34] Carmo, M.; Fritz, D. L.; Mergel, J.; Stolten, D. *International journal of hydrogen energy* **2013**, *38*, 4901.

[35] Ayers, K. E.; Anderson, E. B.; Capuano, C.; Carter, B.; Dalton, L.; Hanlon, G.; Manco, J.; Niedzwiecki, M. *ECS Transactions* **2010**, *33*, 3.

[36] Seger, B.; Kamat, P. V. *The Journal of Physical Chemistry C* **2009**, *113*, 7990.

[37] Kim, H.-J.; Kim, W.-I.; Park, T.-J.; Park, H.-S.; Suh, D. J. *Carbon* **2008**, *46*, 1393.

[38] Kumar, S. S.; Selvakumar, K.; Thangamuthu, R.; Selvi, A. K.; Ravichandran, S.; Sozhan, G.; Rajasekar, K.; Navascues, N.; Irusta, S. *International journal of hydrogen energy* **2016**, *41*, 13331.

[39] Corrales-Sánchez, T.; Ampurdanés, J.; Urakawa, A. *International journal of hydrogen energy* **2014**, *39*, 20837.

[40] McKone, J. R.; Sadtler, B. F.; Werlang, C. A.; Lewis, N. S.; Gray, H. B. *ACS Catalysis* **2013**, *3*, 166.

[41] Mahale, N. K.; Ingle, S. T. *Energy* **2017**, *119*, 872.

[42] Baglio, V.; Di Blasi, A.; Denaro, T.; Antonucci, V.; Aricò, A.; Ornelas, R.; Matteucci, F.; Alonso, G.; Morales, L.; Orozco, G. *Journal of New Materials for Electrochemical Systems* **2008**, *11*, 105.

[43] Cruz, J.; Baglio, V.; Siracusano, S.; Ornelas, R.; Ortiz-Frade, L.; Arriaga, L.; Antonucci, V.; Arico, A. *Journal of Nanoparticle Research* **2011**, *13*, 1639.

[44] Vesborg, P. C.; Jaramillo, T. F. *RSC Advances* **2012**, *2*, 7933.

[45] Pintado, S.; Goberna-Ferrón, S.; Escudero-Adán, E. C.; Galán-Mascarós, J. R. *Journal of the American Chemical Society* **2013**, *135*, 13270.

[46] Goberna-Ferron, S.; Hernandez, W. Y.; Rodriguez-Garcia, B.; Galan-Mascaros, J. R. *ACS catalysis* **2014**, *4*, 1637.

[47] Qian, L.; Yang, X. *Talanta* **2006**, *69*, 957.
[48] Dhanushkodi, S.; Tam, M.; Kundu, S.; Fowler, M.; Pritzker, M. *Journal of Power Sources* **2013**, *240*, 114.

[49] Berrettoni, M.; Ciabocco, M.; Fantauzzi, M.; Giorgetti, M.; Rossi, A.; Caponetti, E. *RSC Advances* **2015**, *5*, 35435.

[50] Xu, J.; Li, Q.; Christensen, E.; Wang, X.; Bjerrum, N. J. *Int. J. Electrochem. Sci* **2013**, *8*, 2388.

[51] Marshall, A. T.; Haverkamp, R. G. *Electrochimica Acta* **2010**, *55*, 1978.

[52] Wu, X.; Scott, K. *International Journal of Hydrogen Energy* **2011**, *36*, 5806.

[53] Marshall, A.; Børresen, B.; Hagen, G.; Tsypkin, M.; Tunold, R. *Electrochimica Acta* **2006**, *51*, 3161.
[54] Chen, Y. X.; Lavacchi, A.; Miller, H. A.; Bevilacqua, M.; Filippi, J.; Innocenti, M.; Marchionni, A.; Oberhauser, W.; Wang, L.; Vizza, F. *Nature communications* **2014**, *5*, 4036.

[55] Senthilkumar, V.; Vickraman, P.; Jayachandran, M.; Sanjeeviraja, C. *Journal of Materials Science: Materials in Electronics* **2010**, *21*, 343.

[56] Cavaliere, S.; Subianto, S.; Savych, I.; Tillard, M.; Jones, D.; Roziere, J. *Journal of Physical Chemistry C* **2013**, 18298.

[57] Savych, I.; Subianto, S.; Nabil, Y.; Cavaliere, S.; Jones, D. *Phys.Chem.Chem.Phys.* **2015**, *17*, 23.

[58] Ciabocco, M.; Berrettoni, M.; Giorgetti, M.; Sougrati, M. T.; Louvain, N.; Stievano, L. *New Journal of Chemistry* **2016**, *40*, 10406.

[59] Giorgetti, M.; Aquilanti, G.; Ciabocco, M.; Berrettoni, M. *Physical Chemistry Chemical Physics* **2015**, *17*, 22519.

[60] Lezna, R. O.; Romagnoli, R.; de Tacconi, N. R.; Rajeshwar, K. *Journal of Physical Chemistry B* **2002**, *106*, 3612.

[61] Sato, O.; Einaga, Y.; Fujishima, A.; Hashimoto, K. *Inorganic Chemistry* **1999**, *38*, 4405.

[62] Krishnakumar, T.; Jayaprakash, R.; Pinna, N.; Phani, A.; Passacantando, M.; Santucci, S. *Journal of Physics and Chemistry of Solids* **2009**, *70*, 993.

[63] Zhang, J.; Gao, L. *Inorganic Chemistry Communications* **2004**, *7*, 91.

[64] De Tacconi, N. R.; Rajeshwar, K.; Lezna, R. O. *Chemistry of Materials* **2003**, *15*, 3046.

[65] Han, L.; Tang, P.; Reyes-Carmona, Á.; Rodríguez-García, B.; Torréns, M.; Morante, J. R.; Arbiol, J.; Galan-Mascaros, J. R. *Journal of the American Chemical Society* **2016**.

[66] Lehmann, V.; Gösele, U. *Applied Physics Letters* **1991**, *58*, 856.

[67] Garcés, F.; Acquaroli, L.; Urteaga, R.; Dussan, A.; Koropecki, R.; Arce, R. *Thin Solid Films* **2012**, *520*, 4254, Garcés, F.; Budini, N.; Koropecki, R.; Arce, R. *Thin Solid Films* **2013**, *531*, 172, Garcés, F.; Budini, N.; Arce, R.; Schmidt, J. *Thin Solid Films* **2015**, *574*, 162.

[68] https://www.osha.gov/dts/sltc/methods/inorganic/t-id126sgx-pv-01-0112-m/t-id126sgx-pv-01-0112-m.html

[69] Vo, V.; Van, M. N.; Lee, H. I.; Kim, J. M.; Kim, Y.; Kim, S. J. *Materials Chemistry and Physics* **2008**, *107*, 6.

[70] Cavaliere, S.; Jiménez- Morales, I.; Ercolano, G.; Savych, I.; Jones, D.; Rozière, J. *ChemElectroChem* **2015**, *2*, 1966.

[71] Wang, Y.; Brezesinski, T.; Antonietti, M.; Smarsly, B. *Acs Nano* **2009**, *3*, 1373.

Optically active molecule-based high temperature magnets

4.1. Introduction

4.1.1. Magnetism.

Since the earliest historical references to the phenomenon of magnetism range from ancients Chinese and Indian, in IV century B.C, to Thales of Mileto in ancient Greece, between 6th and 7th centuries B.C.[1]; human being has tried to understand and profit greatly from the discovery of magnets and magnetism. This reliance on magnets is assured to expand as we move further into the 21st century.

Figure 4.1.1 *The first compass was used not to point people in the right direction literally, but helping them order and harmonize their environments and lives. (Ancient China, 4th century B.C.)*

Magnets are found in many devices and are often taken for granted. These products have an impact on all parts of society and our economy. As an example, there are more than twenty magnets in an automobile[2]. The market size of magnetic materials was around 55.52 USD Billion in 2014, and is projected to reach USD 96.00 Billion by 2020, at annual growth projected of 9.6% until 2020.[3] This field will only continue to grow in the future. As a direct consequence of the continued importance placed on magnets and magnetism, many materials-science laboratories worldwide are focusing on the development and the improvement of magnetic materials.

All matter is affected, in one way or another, by the presence of a magnetic field (H). It can be, in general, attracted or repelled, depending on their electronic configuration. When the magnetic field is repelled, it is called a diamagnetic response (antiparallel alignment, Figure 4.1.2). Diamagnetic behavior is present in all substances, since its microscopic origin is due to the perturbation of the magnetic field to the movement of paired electrons in their orbits. It is typically a weak perturbation, and it is only relevant in the absence of other magnetic response. Diamagnetic susceptibility (χ^D), in a first approximation, is constant for a given material, and does not depend on applied field nor temperature.

When the magnetic field is attracted, it is called a paramagnetic response (parallel alignment, Figure 4.1.2). This is due to the presence of unpaired electrons. When an external magnetic field is applied, the net spins get oriented in the same direction, minimizing this total energy. Contrary to χ^D, paramagnetic susceptibility (χ^P) is temperature dependent, due to the thermal contribution (entropy) that affects the perfect alignment with the external magnetic field.

Thus, the magnetic susceptibility (χ) of any material has two components. The diamagnetic contribution is always present. But it is always much smaller than the paramagnetic contribution, if unpaired electrons are present. Because of this, the latter are typically called paramagnetic materials.
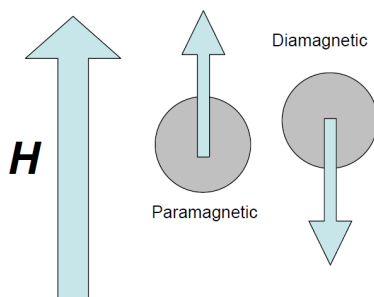

Figure 4.1.2 Possible orientations of the matter under a magnetic field

$$\chi = \frac{\partial M}{\partial H} \; \textit{if H is small} \; \chi = \frac{M}{H} \tag{Eq. 4.1}$$

$$\chi = \chi P + \chi D \tag{Eq. 4.2}$$

Some paramagnetic materials may show permanent magnetization, in the absence of an external magnetic field. This arises from strong interactions between unpaired spins in the solid, giving raise to long range magnetic order, structured into magnetic domains. Parallel alignment of all magnetic moments in a given lattice, in the absence of an external magnetic field, is called ferromagnetic ordering, as it is at the origin of ferromagnets. This spontaneous magnetization may also be destroyed by entropy (thermal energy) and it only occurs below a certain critical temperature (T_C or Curie temperature). Above T_C, entropy is strong enough to destroy the magnetic alignment, and the material becomes paramagnetic.

Permanent magnets are key components of multiple technological applications (memory units, engines, circuits, etc.). These magnets are typically required to have a very high T_C, since industrial processes or devices work at room temperature or above. The ordering temperature depends on the magnetic interactions between spin carriers. This is imposed by the crystal and electronic structure of a given material, which determines distances, effective overlap, symmetry, number of neighborhood, etc. For this reason, among others, classic magnets (with highest T_C) are metals such as cobalt or iron, their alloys, or oxides of different kinds,[4] where interactions between spin carriers (metal centers) are the strongest.

I.   *Molecule-based magnets.*

Molecule-based magnets (MMs) are a diverse and promising class of magnetic materials obtained from the combination of metallic cations connected by ligands, responsible for the magnetic super-exchange in the solid. These coordination chemistry magnets are distinct when compared with classic magnets, typically dense solid state materials, as metals[5,6,7] , alloys [8,9,10,11,12] and oxides [13 , 14 , 15] . In MMs magnetic ordering coexists with low density, transparency, electrical insulation, and low temperature fabrication[16], properties that are unavailable in conventional magnets.

Most of them are based in extended systems of paramagnetic ions linked by bridging ligands that offer efficient pathways (*e.g.* overlapped π-orbitals) to allow for strong super exchange interactions, giving rise to magnetic ordering[17]. An exciting possibility offered by MMs within materials science is the synthesis and design of multifunctional magnetic materials combining different physical and chemical properties. This trend opens new technological applications and/or novel physical phenomena [18] , since the combination of physical properties may be tailor-made by the right selection of building blocks[19].

These advantages come with one important drawback. The low density and ligand connectivity in MMs promotes weak (or very weak) interactions between spin carriers (the metal centers, or organic radicals), resulting in very low critical temperatures. Most MMs behave as magnets only below liquid He temperature (5K). Only small bridging ligands, offering connectivity pathways of 3 atoms (or less) and/or incorporating a π pathway, have deliver higher temperature magnets. Such ligands include azine [20] , azide [21] , oxalate [22 , 23] oximate[24,25,26], triazole[27], etc. Better than all them is the cyanide ligand. It offers the shorter available pathway (M^{a+}–CN–M^{b+}), with strong π contribution, and with good orthogonality between magnetic orbitals to maximize their overlap. With all these ligands, a great variety of molecular magnets have been obtained,

mimicking the properties commonly associated with classical magnets, including high coercivity[28] and critical temperature over room temperature[29].

4.1.2. High ordering temperature PBA magnets.

The family of Prussian blue analogues exhibit magnetic ordering temperatures in a very large temperature range, from liquid nitrogen to up to 373K. T_C depends on the metal centers and their corresponding oxidation state. Examples of these high temperature magnets are $CsMn^{II}[Cr^{III}(CN)_6]$ (90K) [30], $Cs_2[Ni(V(CN)_6]$ (125K) [31], $Cr_{1.5}[Cr(CN)_6]$ (240K) [32], $Cr^{III}[Cr^{III}(CN)_6]_{0.93}[Cr^{II}(CN)^6]_{0.005}$ (260K) [33], $V^{II}_{0.42}V^{III}_{0.58}[Cr^{III}(CN)^6]_{0.86}$ (315K)[34] or $K_{0.058}V^{II/III}[Cr^{III}(CN)_6]_{0.79}$ (372K)[35]. As mentioned before, magnetic interaction, ordering temperature and magnetic properties strongly depend on electronic configuration, structure, and cyanide orbitals interaction[36].

Vanadium-chromium Prussian blue analogues are the room temperature magnets reported up to date in the family. In this case, magnetic interaction between spin carriers is antiferromagnetic (antiparallel alignment) but the different magnetic moment still stabilizes spontaneous magnetization. These magnets are called ferrimagnets[37].

Ferrimagnet
Below T_C, spins are aligned
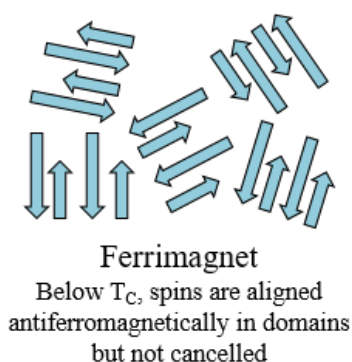antiferromagnetically in domains
but not cancelled

Figure 4.1.3 Representation of spins alignment in magnetic domains in a ferrimagnet

Although these materials are essentially amorphous, the short-range structure is known. The Cr^{III} cations are linked to six cyanide ligands in octahedral configuration through the carbon end. The coordination of the vanadium centers (typically in a mixture of II/III oxidation states, depending on preparation) is not as easy to determine, due to the non-stoichiometric nature. Depending on stoichiometry, they are coordinated to 4-6 to six nitrogen atoms, and solvent molecules. The magnetic moments from Cr^{III} and V^{II} are aligned antiparallel[29]. Both being S = 3/2 ions, the spins should compensate each other. However, the stoichiometry (V/Cr ≈ 1.5), and the presence of V in higher oxidation states (III and even IV) give rise to ferromagnetic ordering. For example, it was also reported by Verdaguer and co-workers in 2002 that the presence of catalytic amounts of V^{III} during the synthesis of these materials lead to PBAs with stoichiometry close to $VCr_{2/3}$[38].
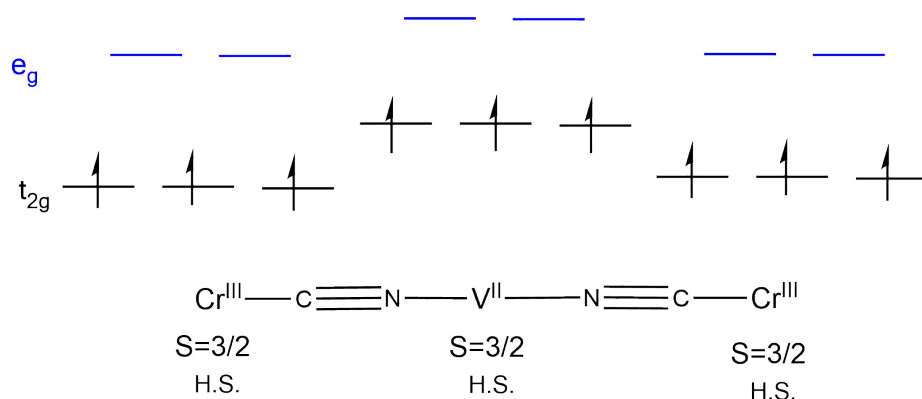
Figure 4.1.4 V^{II}-CN-Cr^{III} moieties in Prussian blue structure (not to scale)

At the practical level, a primary feature of these compounds is that they must be prepared under inert atmosphere conditions. The inherent instability of vanadium cations in low oxidation states, even when they form part of the PB structure, makes them difficult to handle, synthesize and characterize. The V^{II}-Cr^{III} PBA is readily oxidized to the V^{IV} analogue when exposed to air. This new compound is also a ferrimagnetic material. Both antiferromagnetically coupled

ions are non-equivalent ($S_{Cr^{III}} = {}^3/_2$; $S_{V^{IV}} = {}^1/_2$) . T_C is significantly lower (115K) in this vanadyl-chromium PBA. The exposition to air transforms the octahedral V^{II} centers into pentacoordinate V^{IV}=O symmetry, with an oxygen atom linked by a double bond in the apical position[39]. This change in symmetry produces an alteration in the linearity of the cyanide bridges, and along structural changes in connectivity, decreases the strength of magnetic interactions and consequently rising the T_C.

4.1.3. Multifunctional magnetic materials.

MMs are particularly well-suited for the development of multifunctionality. These materials are obtained from molecular building blocks, offering a great versatility. Multiple synthetic tools are available in the design of a rational approach to modify or combine multiple functions in the starting molecular building blocks. Thus, it is possible to synthetize tailor-made materials that combine two or more properties by design. This powerful strategy cannot be applied to traditional inorganic solids, like oxides or alloys.

This synthetic strategy has yielded unique multifunctional materials in which two (or more) properties can coexist independently, cooperate or compete. Some examples include photo-active magnet[40], stimuli responsive conductors[41], magnetic porous materials[42], magnetic sensors[43], etc…

One of the most studied multifunctional molecule-base materials (MMMs) are those that combine electrical and magnetic properties. The most successful strategy was based on the combination of cationic conducting networks with anionic magnetic network. These radical salts were obtained from organic donors, generally derivatives of tetrathiofulvalene (TTF), which provide band of conductivity; and anionic coordination complexes, as magnetic moment carriers.   This combination has been very powerful, yielding magnetic superconductors[44,45], metallic magnets[36], superconducting magnets[46,47] , or

chiral metallic magnets[48]. The latter is a fine example of a true multifunctional material, combining three co-existing physical properties: magnetic ordering, metallic conductivity, and optical activity (Figure 4.1.5).

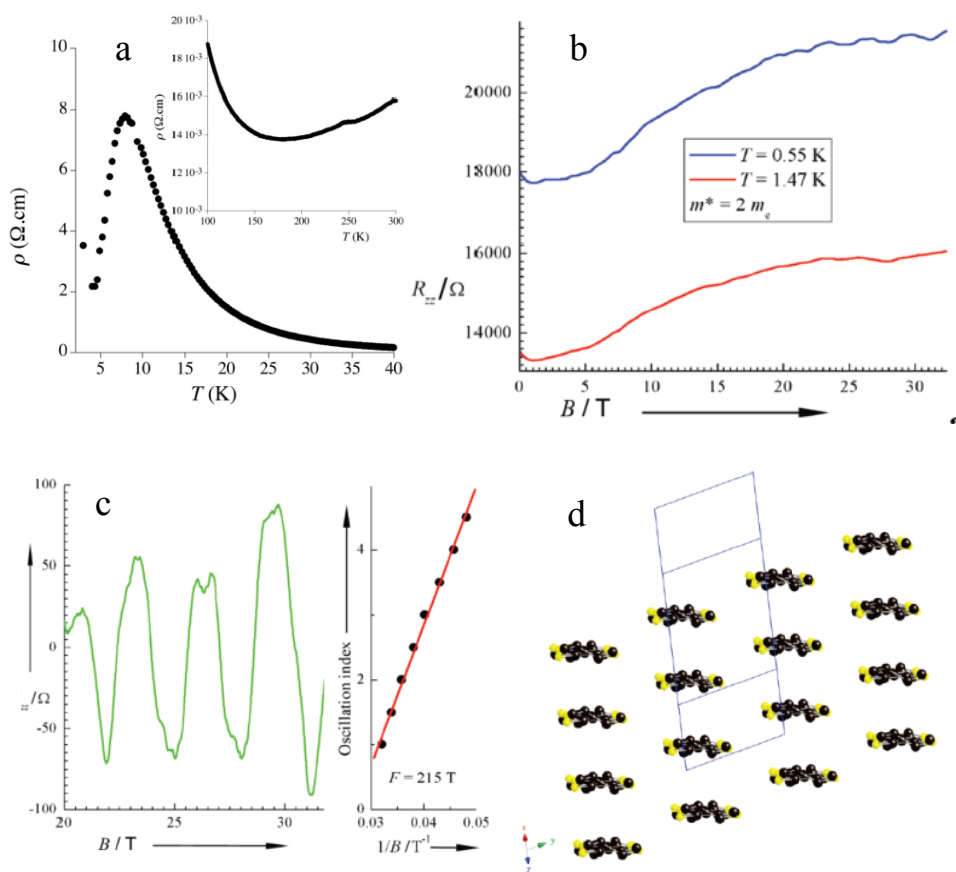***Figure 4.1.5*** *Thermal dependence of the in-plane resistivity for crystals of (TMET)$_x$[MnCr(ox)$_3$]·CH$_2$Cl$_2$ (a), interlayer resistance of a single crystal (b). Shubnikov-de Haas oscillations at 550 mK plot (greenline) of the oscillation index vs inverse field position whose slope gives the frequency (redline) (c). Packing of the organic layers in the crystal structure (d) (from ref.48)*

I.   *Chirality*

Chirality is a concept that appears in several branches of science. In a chiral object, its specular image is not superimposable, due to the absence of a symmetry operation (center of symmetry). As a simple example, the human left hand is not superimposable with the right one, when both are specular images. This difference, originated due to the space group symmetry, has tremendous effects on the physical and chemical properties.

At the molecular level, a chiral molecule may exist as two possible optical enantiomers or isomers, corresponding to the two possible distinct geometries it can adopt: each one the specular image of the other.
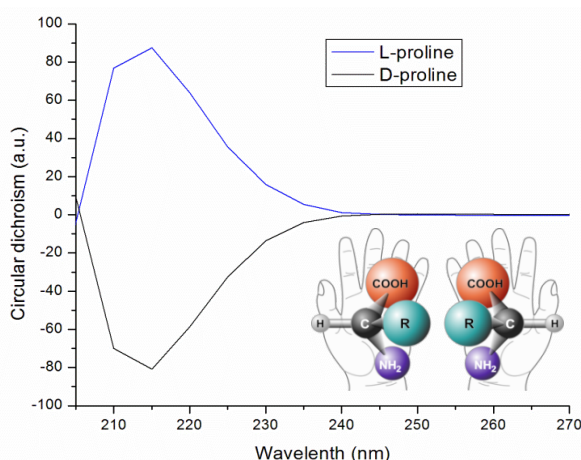
Figure 4.1.6 *Circular dichroism signal aqueous solution of both proline enantiomers, L and D. Hands and amino acids as example of chirality*

Most common and simple way to check whether a compound is chiral or not is to expose it to polarized light (circular dichroism, CD). Each enantiomer will interact differently with the incident beam that will be diverted. This deviation will be of the same magnitude but of opposite direction for each enantiomer (D

or L). Thus, in circular dichroism spectra, signal will be specular images for the two enantiopure samples of a molecule (Figure 4.1.6).

Within the molecular magnetic materials, the incorporation of optical activity, chirality, is of great interest. Chiral magnets have attracted also the attention of physicist and chemist following the observation of co-existing asymmetric magnetic anisotropy and magneto-chiral dichroism[49,50]

In this context, a large variety of bimetallic chiral complexes derived from Prussian blue analogues have been extensively studied. One of the most powerful synthetic strategies to obtain this family of chiral magnets is the combination of a complex between metal ion and chiral ligad with the cyanometallate. The chiral ligand typically coordinates the divalent metal cation, lowering connectivity, but providing optical activity[51].

Figure 4.1.7 *General scheme of synthetic strategy to obtain Prussian blue analogues chiral derivatives with general formula $[M^{a+}(L)_m]_y[M^{b+}(CN)_6]_x$*

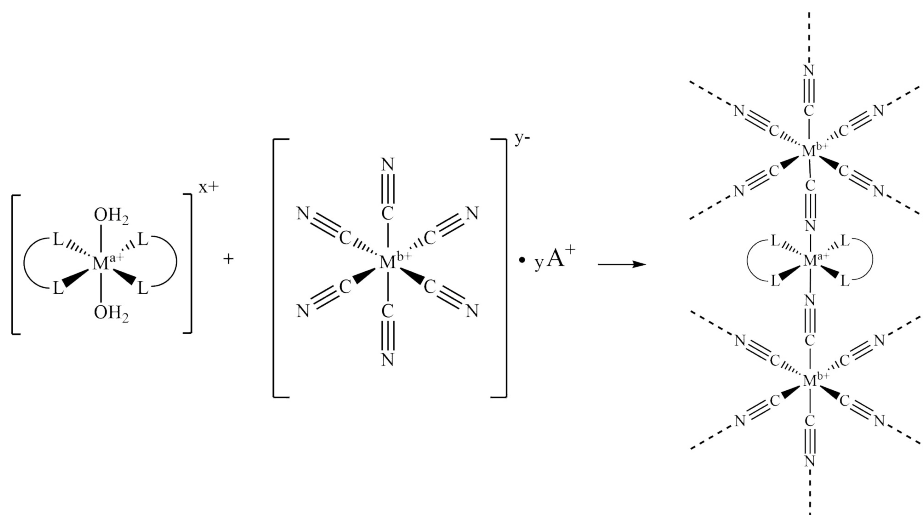With this strategy, a large number of molecular magnets have been obtained, clusters [52,53], both short chain and linear polymers [54,55], and bi [56,57] and tridimensional [58,59]. The dimensionality and topology of these assembled systems depend strongly on the nature of the starting complex $M^{a+}(L)_m$: number of coordination vacancies available in the metal, its coordination geometry, the stereovolume or its functionalization, among others. Additionally, the connectivity of the cyanometalate unit is also important. These systems have few structural defects, and in general, they crystallize in low symmetry space groups presenting magnetic anisotropy. On the other hand, the lower connectivity between the metal centers makes the magnetic ordering temperatures significantly lower than that of their analog Prussian blue structures. This strategy has not been applied to the high temperature magnets, the VCr derivatives. Maybe because of the difficult preparation and handling of these material. However, this possibility is especially appealing since the high temperature chiral magnets could be obtained.

The main objective of this chapter is the incorporation of a chiral inductor in the preparation of high temperature cyanide-based magnets. Our target magnetic material will be prepared from the reaction of vanadium (II) and hexacyanochromate in the presence of an enantiopure coordinating ligand that will provide optical activity to the system.

4.2. Results and discussion.

4.2.1 First attempt: diamine ligands.

In a first attempt, following the strategy previously described for the preparation of chiral magnets with cyanide bridges[60,61,62], we used the bidentate ligand 1,2-diaminocyclohexane (dien). Starting from VCl_2, we could not obtain a single phase compound. As soon as VCl_2 was added to an amine aqueous solution (0.1 M), a brown fine powder precipitate that did not react with hexacyanochromate. Brown solid FT-IR shows oxide/hydroxide peaks an non dien peaks, although these reactions were carried out in strict anaerobious conditions (Figure 4.2.2).
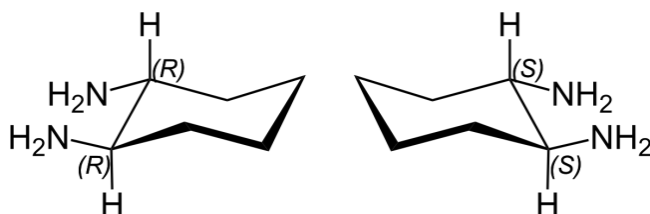
Figure 4.2.1 1,2-diaminocyclohexane ligand enantiomers
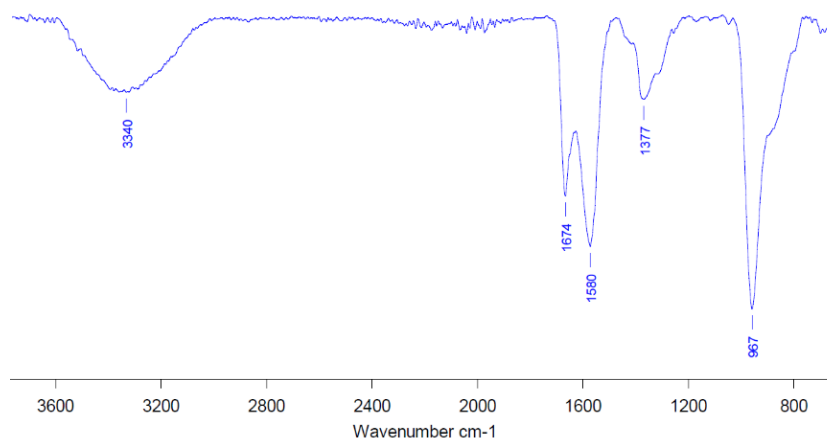
Figure 4.2.2 FT-IR spectra of brown solid

Taking into account that the lower the vanadium oxidation state the more unstable is, we examined the possibility to prepared the corresponding V(dien)$_n$ starting material from a V^{III} source, to be reduced *in situ* to yield the V^{II}-ligand moieties, that will react later with Cr(CN)$_6^{-3}$. According to literature, some high temperature magnets had been prepared as thin films through electro synthetic procedures[63,64,65]. Inspired on this, we attempted to follow this strategy, by applying a reduction potential (-1.0V vs NHE) to an FTO working electrode immersed in a solution containing K$_3$Cr(CN)$_6$, VCl$_3$, and the enantiopure 1,2-diaminocyclohexane (pH=6). A blue-brown fine powder deposited on the electrode surface of the FTO working electrode after several minutes, then powder is scratched to charazterized.

The IR spectra for this materials shows the typical cyanide stretching band(v_{CN}) at 2170cm^{-1}, a weak band at 2116 cm^{-1} assigned to the V^{II}-Cr^{III} couple, and also the V=O stretching band (v_{VO}) at 978cm^{-1}, confirming the presence of vanadyl centers. However, no sign of the presence of the ligand was confirmed.
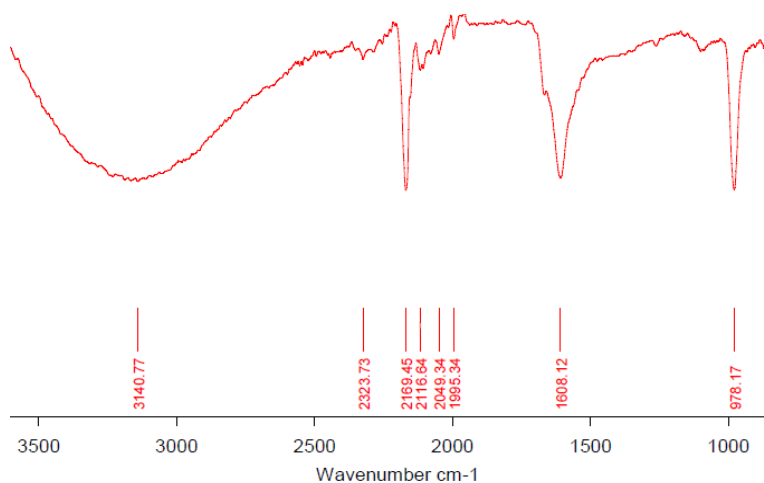
Figure 4.2.3 *FT IR spectra of compound synthesized with 1,2-diaminocyclohexane as ligand.*

Magnetic measurements[*] (Figure 4.2.4) indicate this material is essentially the vanadyl Prussian blue analogue[39], with the characteristic $T_C \approx 120$ K as defined by the as defined by the zero-field cooled, field cooled and remnant magnetization.
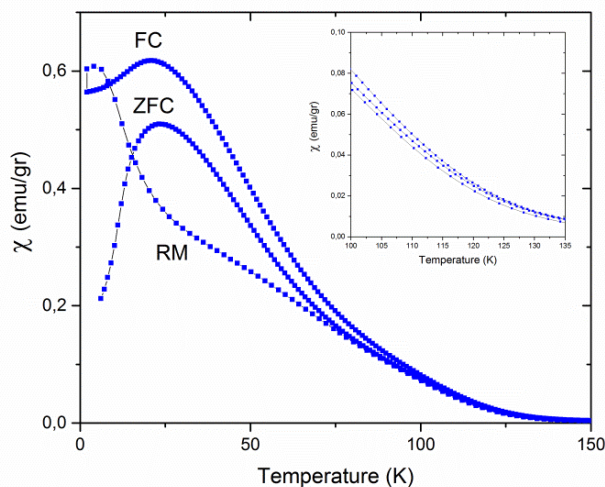
Figure 4.2.4 *Thermal dependence of magnetic susceptibility in field-cooled (FC), zero field-cooled (ZFC) and remmanent magnetization (RM) at 50 Oe applied field (H) in compound synthesized with enantiopure dien.*

No optical activity was found, as expected, due to the absence of ligand in the material.

We associated this synthetic problem to the basicity of the ligand. A 0.1M solution of dien already reaches pH=10, destabilizing V^{II}. Looking at the vanadium Pourboix diagram, it is evident that the low oxidation states are unstable at such high pH in water. Indeed, it is common to find in the literature that the starting materials for V^{II} compounds are prepared from strong acids (*e.g.* triflic acid)[66,67]

---

[*] Magnetic measurements will be plot in terms of emu/gr for all VHCr compounds. This makes easier direct comparison for all derivatives of these non-stoichiometric and hard to-handle compounds of variable composition.
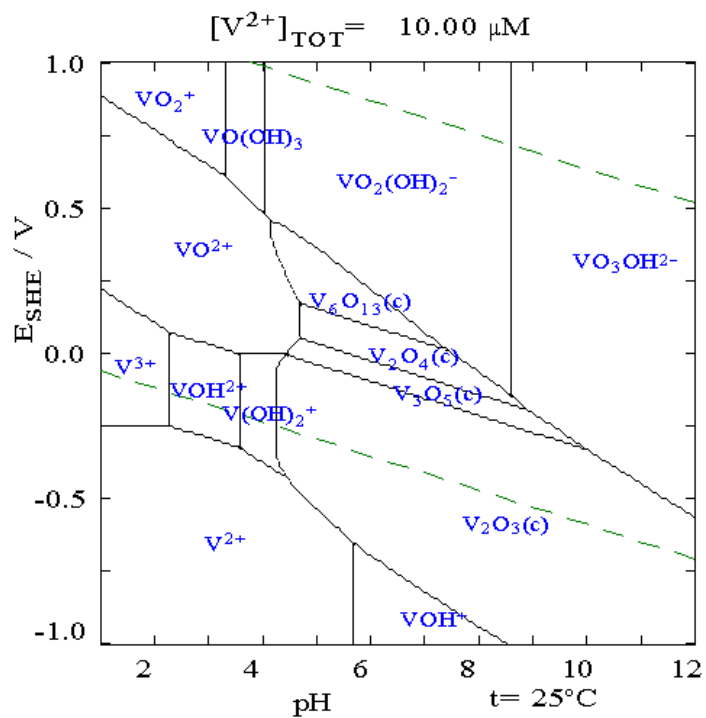
Figure 4.2.5 *Pourboix diagram of vanadium species in water*

4.2.2 Amino acid ligands: L-proline

Looking for other chelating ligands with lower impact on pH, or even with acid character, we turned our attention to natural amino acids. Being zwitterions, most aminoacids do not modify pH conditions. Among them, proline seemed to be the best suited to act as a chelating enantiopure ligand. In proline, the tertiary chiral carbon is linked to a carboxylic acid (pKa 1.95) and to a secondary amine (pKa 10.47). Its most preferred coordination mode uses the secondary amine and the carboxylate group, to form a very stable 5 membered coordination ring with metal cations. This coordination is predominant even at very low pH (below 4), as required for the success of our synthesis[68,69].
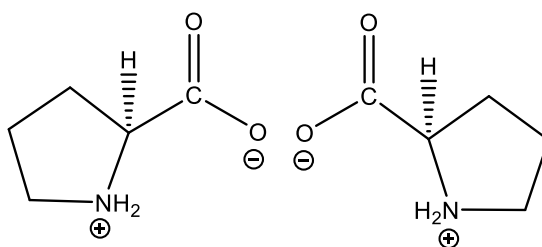
Figure 4.2.6 *Zwitterionic structure of both proline enantiomers: (S)-proline (left) and (R)-proline*

I.   Synthesis and characterization

With these perspectives, we carried out the reaction between VCl_2 and L-proline (L-pro) in water in a 1:2 ratio. Overnight, the initial green dispersion became a brown solution. Our attempts to isolate the $V(L-pro)_2X_n$ complex from solution were unsuccessful. Therefore, we followed the reaction by filtering adding a aqueous Tetrabutilammonium hexacyanochromate (TBA_3-$Cr(CN)_6$) to the brown solution. Immediately, a deep blue precipitate formed (**1**). The solid was centrifuged and washed with water and methanol. As a control experiment, we carried out the same reaction, in absence of proline, to assess the formation of a pure $V/Cr(CN)_6$ phase under these synthetic conditions. As described before,

the magnetic properties of these high T_C magnets are very sensitive to preparation conditions. Therefore, comparison between **1** and the proline-less compound (**zero**) will be fundamental to understand the effect of the ligand in the optical and magnetic properties. Additionally, these compounds were exposed to air for 24h to check their stability. For compound **1,** the formula $Na_{0.1}K_{0.26}(TBA)_{0.53}[V(O)]_{1.65}[Cr(CN)_6]_{1.08}(Pro)_{4.3}Cl_{0.9} \cdot 13H_2O$ ($M_w = 1105.102$ g/mol) was confirmed by elemental analysis (after exposition to air), distinct from the results for compound **zero**. $V(O)_{9.25}[Cr(CN)_6]_{0.80}Cl_8 \cdot 16H_2O$ ($M_w = 1429,424$ g/mol). Vanadium content is very high in **zero**, with a high chlorine content, suggesting the presence of vanadium chloride impurities. This may appear due to the high insolubility of VCl_2, that was not removed upon washing and purification.

Spectroscopic characterization of vanadium/proline "1:2" (1)

The IR spectra (Figure 4.2.7) for **1** confirmed the presence of proline in the compound by the signature band at 2964 cm^{-1} (orange box) corresponding to the hydrogen nitrogen stretching frequency. The CN^{-} stretching band is centered at 2160 cm^{-1} in compound **zero**, corresponding to the V^{III}-Cr^{III} pair. This peak tends to decrease when the compound is exposed to air, meanwhile a peak centered at 2168 cm^{-1} confirms the oxidation to the V^{IV}-Cr^{III} phase.

Moreover, in the proline-free compound (**zero**), two bands are present initially, one weaker, centered at 2118 cm^{-1} assigned to V^{II}-Cr^{III} and another one, stronger, centered at 2175 cm^{-1} corresponding to V^{IV}-Cr^{III} couple. After being exposed to the air, the oxidation of vanadium to vanadyl is more prominent. In all compounds, before and after air, the presence of vanadyl groups is confirmed by oxygen-vanadium (IV) stretching band between 975 cm^{-1} and 980 cm^{-1} wavenumbers.
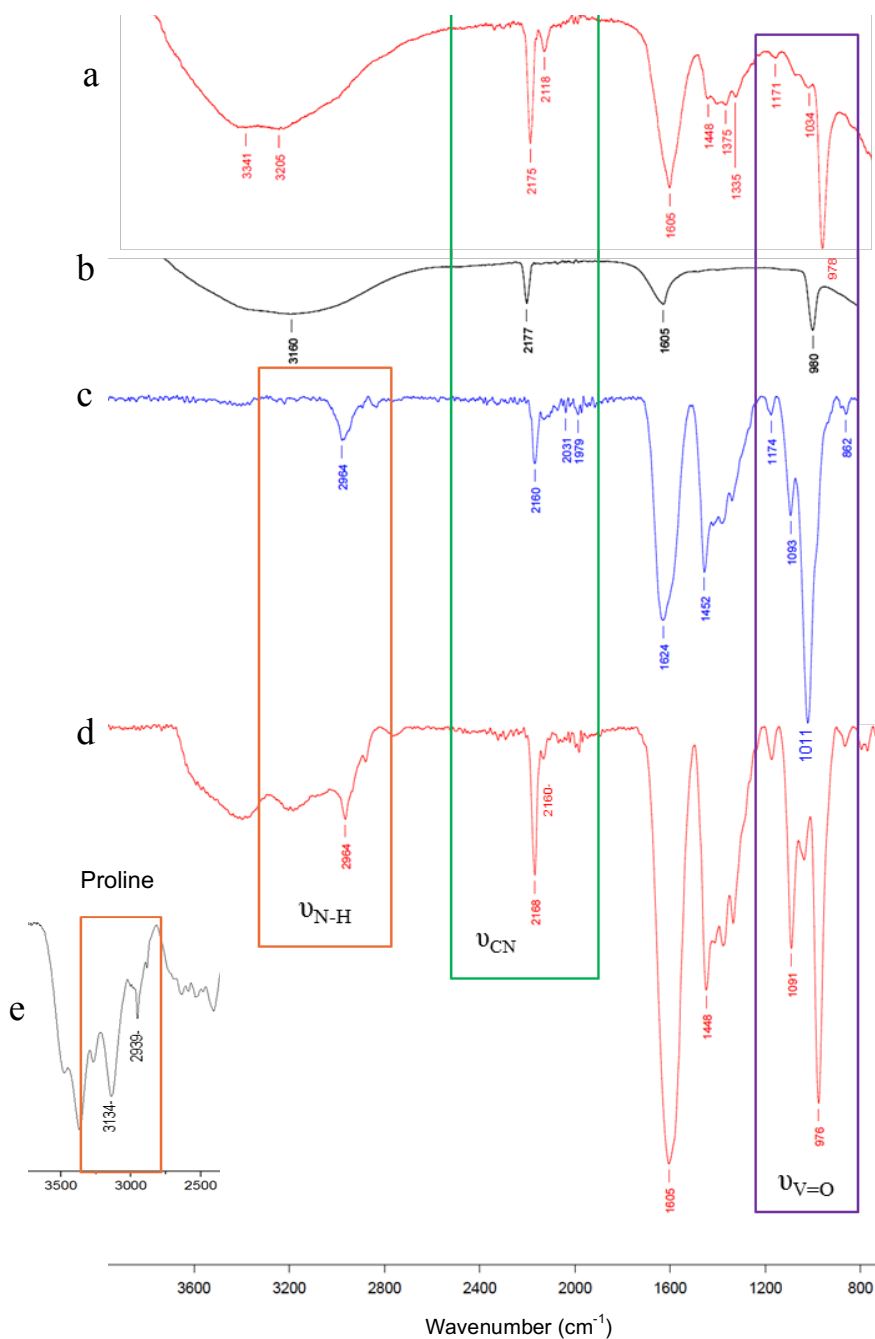
Figure 4.2.7 *FT-IR of **2** as prepared (a) and after 24h exposed to air (b), **1** as prepared (c) and **1** after 24h exposed to air (d). Proline spectra also show it (e)*

Magnetic properties

To characterize the magnetic behavior of these materials, we performed zero-field-cooled/field cooled (ZFC/FC) magnetic measurements (Figure 4.2.8). Critical temperature can be extracted from the point where the two curves separate. Compound **1** shows a T_C of 130 K, and decreases down to 28K once it is exposed to air. This is typical of these materials, and indicates the air oxidation of vanadium to vanadyl. **Zero** shows a T_C of 275 K (Figure 4.3.9), and of 120 K once it is exposed to air, which is in agreement with IR data (Figure 4.2.7) .

In the case of **zero**, the initial T_C indicates partial oxidation of the material, since it is significantly lower than literature data, owing to our different synthetic procedure. After air oxidation, the T_C is in good agreement with the vanadyl Prussian blue analogue[70]. The significantly different T_C for **1** indirectly confirms the participation of the ligand binding the vanadium centers. The lower T_C must be due to lower connectivity and dimensionality, since the L-pro ligand blocks coordination sites, and bridging super exchange pathways.

The remnant magnetization (RM) existing after the external magnetic field is removed, confirms the spontaneous magnetization in compound **1, below T_C**. This memory effect becomes almost negligible when **1** is exposed to air, which reinforce the idea of a change in magnetic behavior when V^{IV} is formed.

Surprisingly, RM is higher in **1**, suggesting that the presence of ligand enhances the memory effect in this material, making it a harder magnet. Field dependence of the magnetization (Figure 4.2.10) was measured at 2K. Magnetization at saturation (M_s) reaches 0.650 μ_b/mol, and a coercive field of 350 Oe was found. A very low remnant magnetization (M_r= 0.135 μ_B/mol) was also observed.
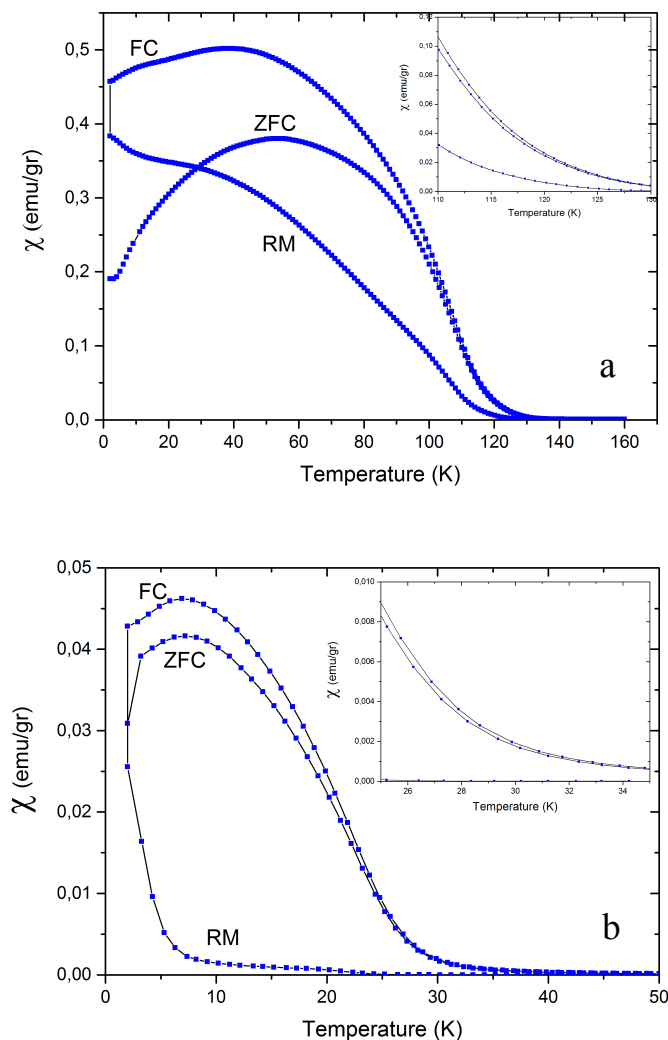
Figure 4.2.8 *Thermal dependence of magnetic susceptibility in field-cooled (FC), zero field-cooled (ZFC) and remmanent magnetization (RM) at 50 Oe applied field (H) in **1** as prepared (a) and **1** exposed to air (b).*
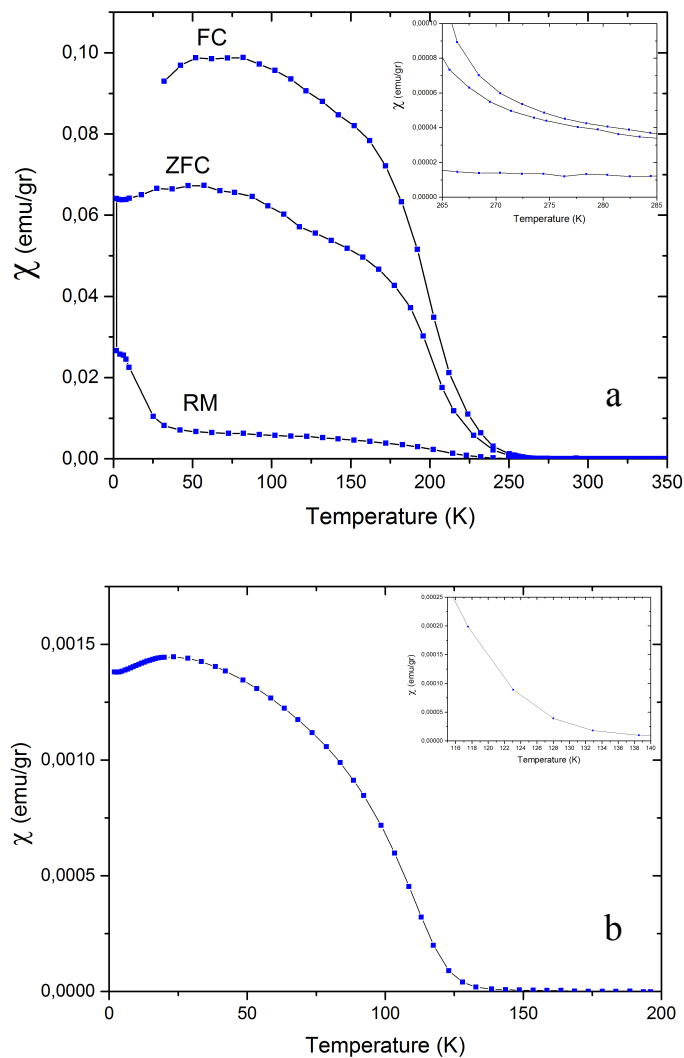
*Figure 4.2.9 Thermal dependence of magnetic susceptibility in field-cooled (FC), zero field-cooled (ZFC) and remmant magnetization (RM) at 25 Oe applied field (H) and in **zero** as prepared (a) and magnetic susceptibility in field-cooled (FC) at 1000 Oe in **zero** exposed to air (b).*
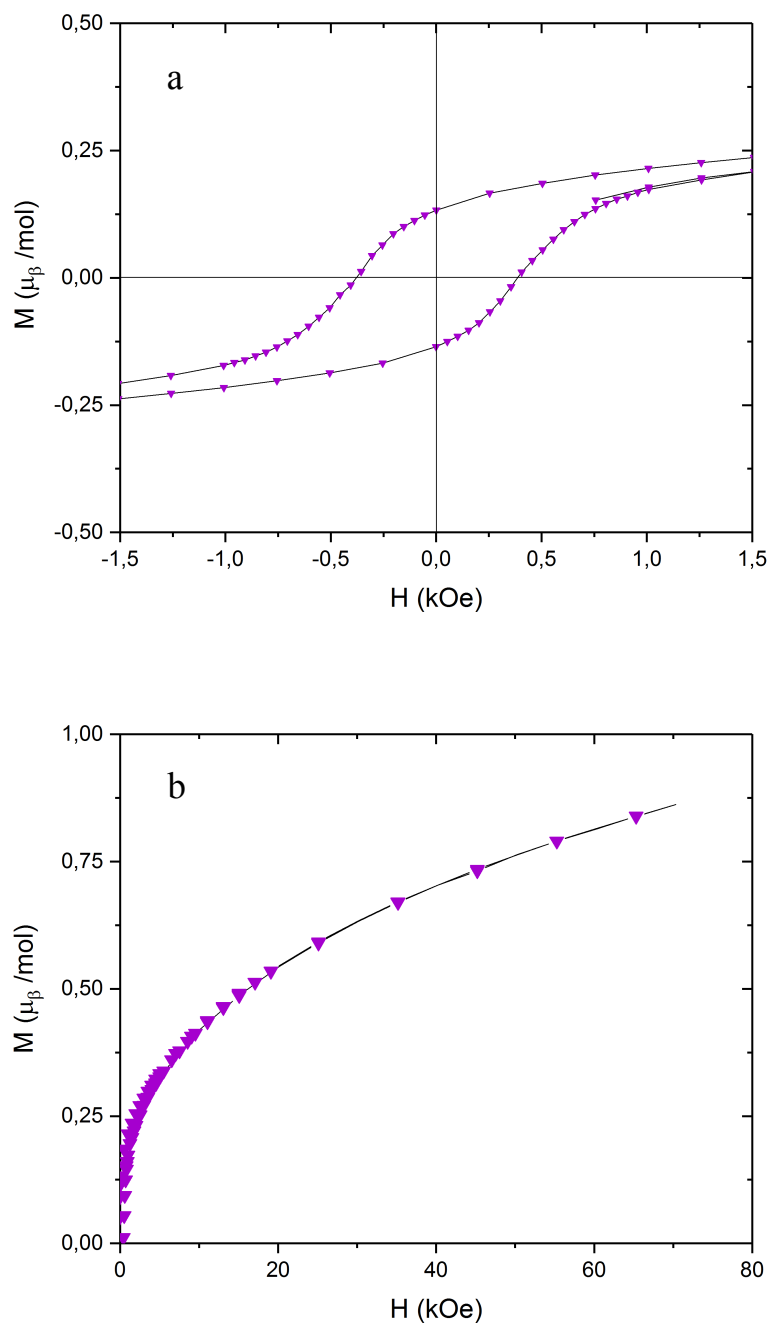
Figure 4.2.10 *Magnetization vs field up to 30k Oe (a) Hysteresis loops between -1,5 KOe to 1,5 KOe (b) at T=2K in compound 1 as prepared*

Optical activity

UV-vis spectra were recorded in the solid state. Three bands were revealed, a charge transfer band centered at 375 nm, a weak band centered at 475 nm, and a wide band centered around 700 mn (Figure 4.2.11 black line).

Circular dichroism spectra were recorded for L-**1** and also for D-**1** (Figure 4.4.11b). Both enantiomers were obtained from the same procedure, and showed identical magnetic behavior, but using as starting material L-pro or D-pro, respectively. The CD signals from both enantiomers are specular images, showing maxima (and the corresponding minima) at 450 and 640 nm, in good agreement with the absorption bands.

This confirms that chirality has been transferred to the magnetic structure. It is worthy to mention that these absorption bands in the visible are participated by the metal centers, and do not belong exclusively to the proline ligand, that only absorbs in the UV region (Figure 4.1.6).
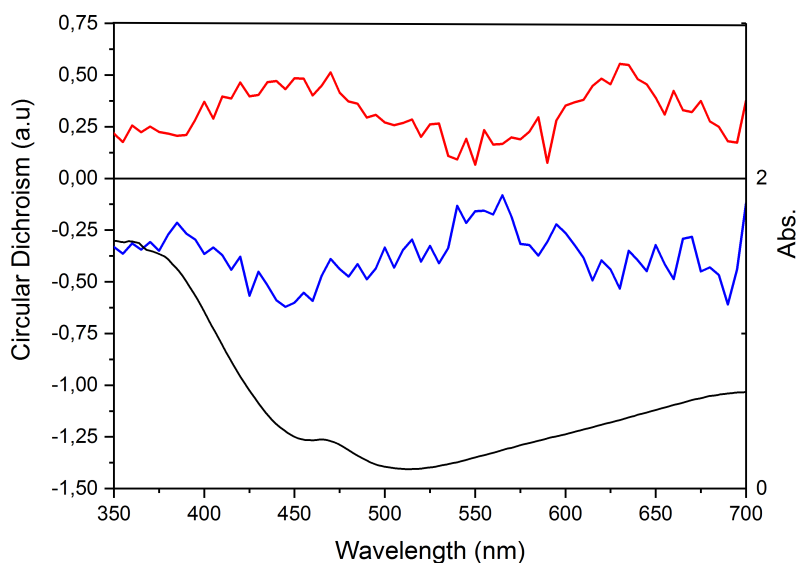
Figure 4.2.11 *Solid state UV-vis spectra (black line) Circular dichroism compound **1**: D enantiomer (red line), L enantiomer (blue line)*

4.2.3. Higher T_C chiral V-Cr Prussian blue coordination magnets.

Less proline means higher ordering temperature?

I.   Synthesis and characterization

The same synthetic procedure was carried out but, in this case, with a 1:1 V/pro ratio in solution. Addition of an aqueous solution of tetrabutilamonium hexacyanochromate (TBA-Cr(CN)$_6$) to this solution immediately yielded a deep blue powder (**2**), that was purified following the same procedure. For compound **2**, the stoichiometry was (TBA)$_{0.55}$V(O)$_{4.2}$[Cr(CN)$_6$]$_{0.77}$(L-pro)$_{1.83}$Cl$_3$ 30H$_2$O, after air exposition. Again, vanadium chloride impurities were detected.

Spectroscopic characterization of vanadium/proline "1:1" (2)

Once more, the presence of proline in **2** was confirmed by a band at 2964 cm^{-1} (Figure 4.2.12, orange box). The 2010 cm^{-1} peak corresponds to V^{II}-Cr^{III} pairs, and the weak 2170 cm^{-1} peak reflects the presence of a V^{IV}-Cr^{III} units, as confirmed by a weak V-O double bond peak centered in 978 cm^{-1}. It is highly remarkable that the V^{II}-Cr^{III} peak is not significantly affected even when compound **2** is exposed to air (24 h). This suggests that this V-Cr material is somehow more redox stable.
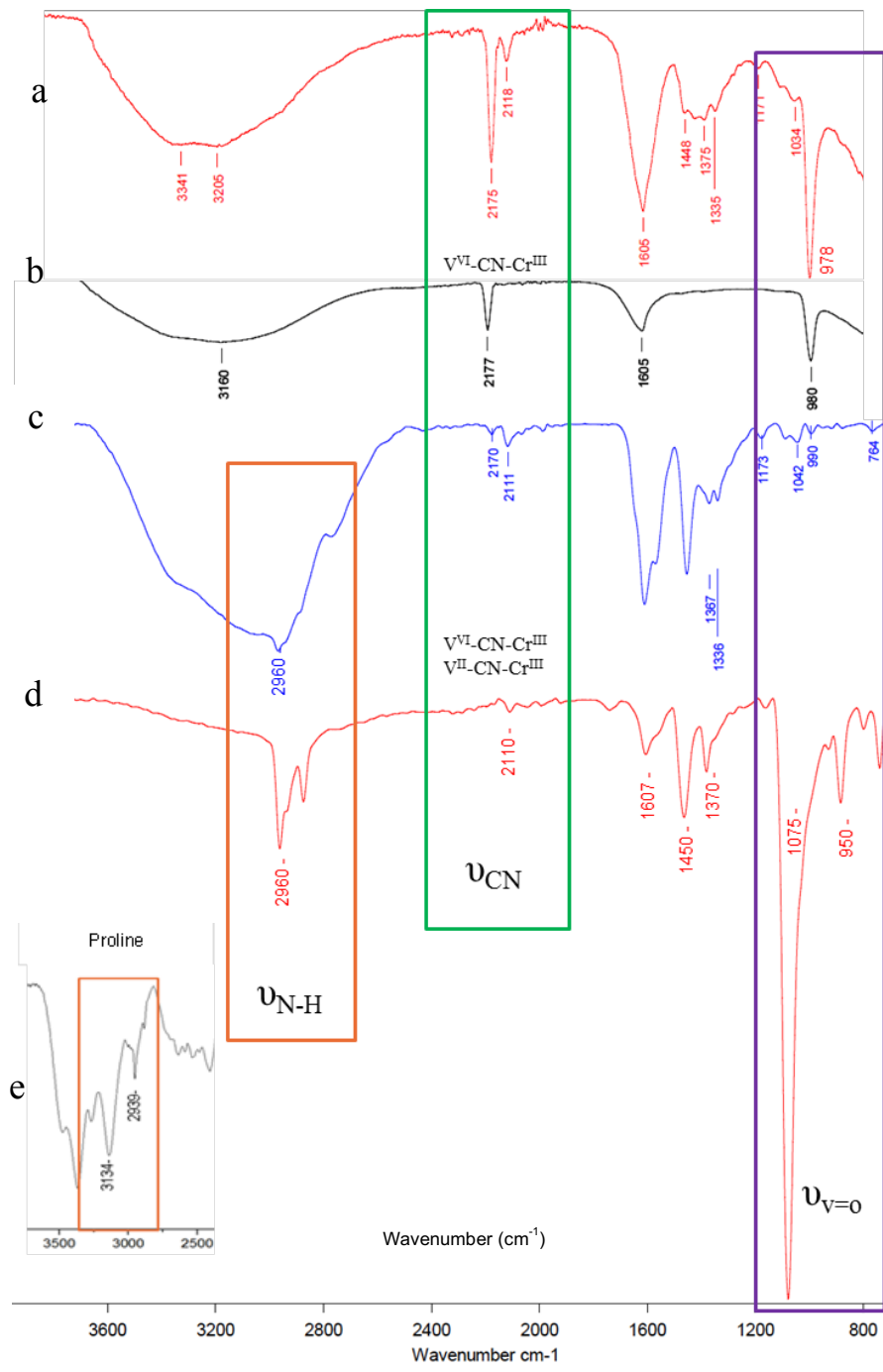
Figure 4.2.12 FT-IR spectra of *2* as prepared (a), *2* after 24h
exposed to air (b), *zero* in as prepared (c) and *zero* after 24h exposed
to air (d).

Magnetic properties

Compound **2** orders magnetically below 265K (Figure 4.2.12), a tremendous increase in T_C when compared with compound **1**. This must be due, at least in part, to the higher dimensionality, and connectivity, as expected in this material. But we cannot neglect the participation of a higher number of V^{II}-Cr^{III} pairs, due to the apparent higher redox stability. Higher V^{II} content typically yields higher T_C. After 24 h exposed to air, T_C drops only by 30K, down to 235K.

This is in good agreement with the IR data, and supports the higher stability of this material, compared with previous compounds. It is particularly surprising that the "oxidized" form of **2** still shows magnetic ordering at higher temperatures than **zero**, the pure and "perfect" 3D analog we obtained in the same conditions. Memory effect drops after oxidation, as suggests by the difference between ZF and ZFC plots, and the comparison between RM.

The field dependence of the magnetization and the corresponding hysteresis cycles were measured at 2K for **2** (Figure 4.2.13). Magnetization at saturation (M_s) reaches 3 μ_b/mol and drops to 2,15 μ_b/mol after air oxidation. The coercive field, H_C=180 Oe, drops to just 55Oe after air exposition. However, remnant magnetization (M_r) is identical for both compounds (0.796 μ_b/mol). If compared with **1**, we found in this case a higher M_s (3 vs 0.65 μ_b/mol); and higher remnant magnetization (M_r (**1**) = 0.135 *vs* M_r (**2**) = 0.796 μ_B/mol); but narrower hysteresis (H_C (**1**) = 350 *vs* H_C (**2**) = 180 Oe) (Figure 4.2.14).
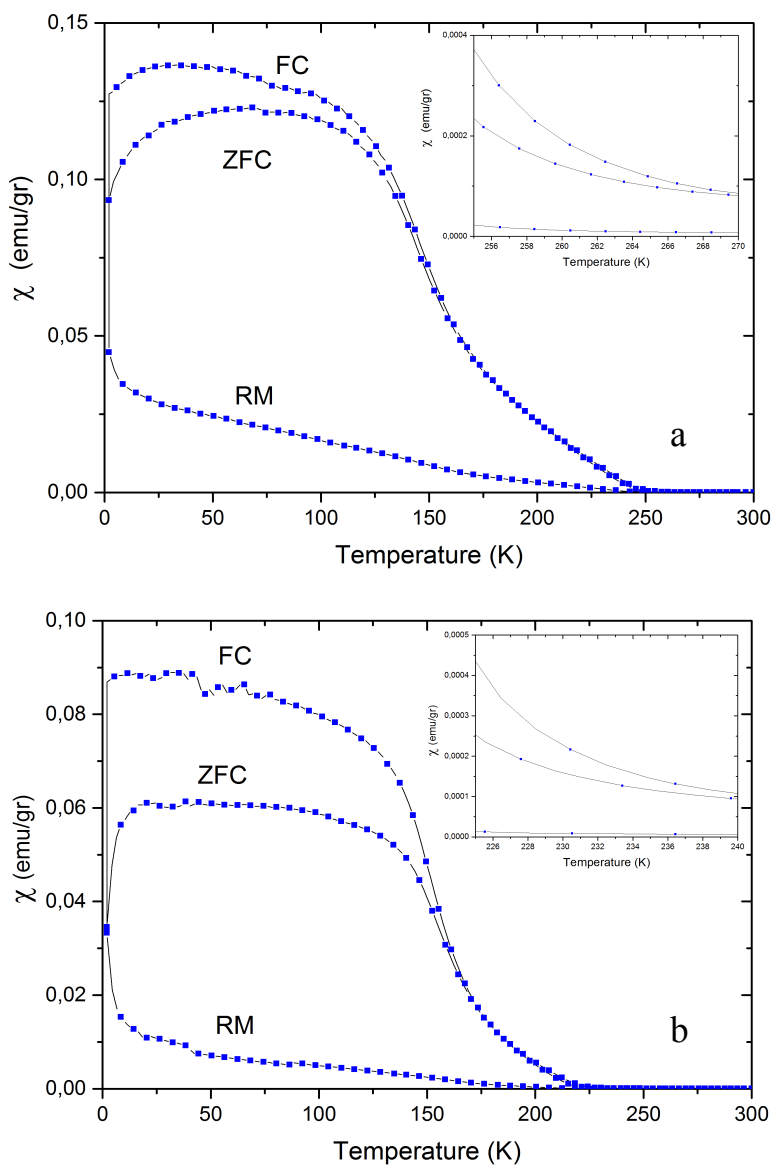
Figure 4.2.12 *Thermal dependence of magnetic susceptibility in field-cooled (FC), zero field-cooled (ZFC); Remnant magnetization (RM) at 25 Oe applied field (H) in **2** as prepared (a) and **2** exposed to air (b).*
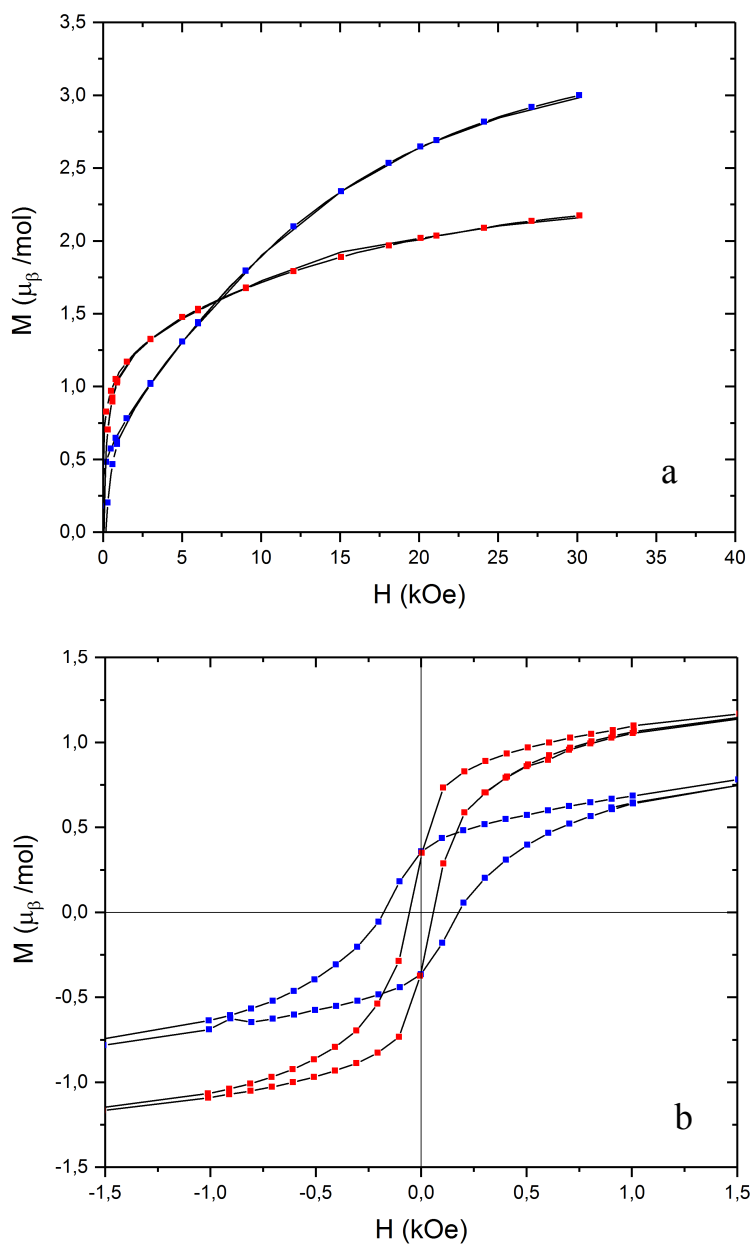
Figure 4.2.13 *Magnetization vs field up to 30k Oe (a) Hysteresis loops between -1,5 KOe to 1,5 KOe (b) at T=2K in compound **2** as prepared (blue) and **2** exposed to air (red).*
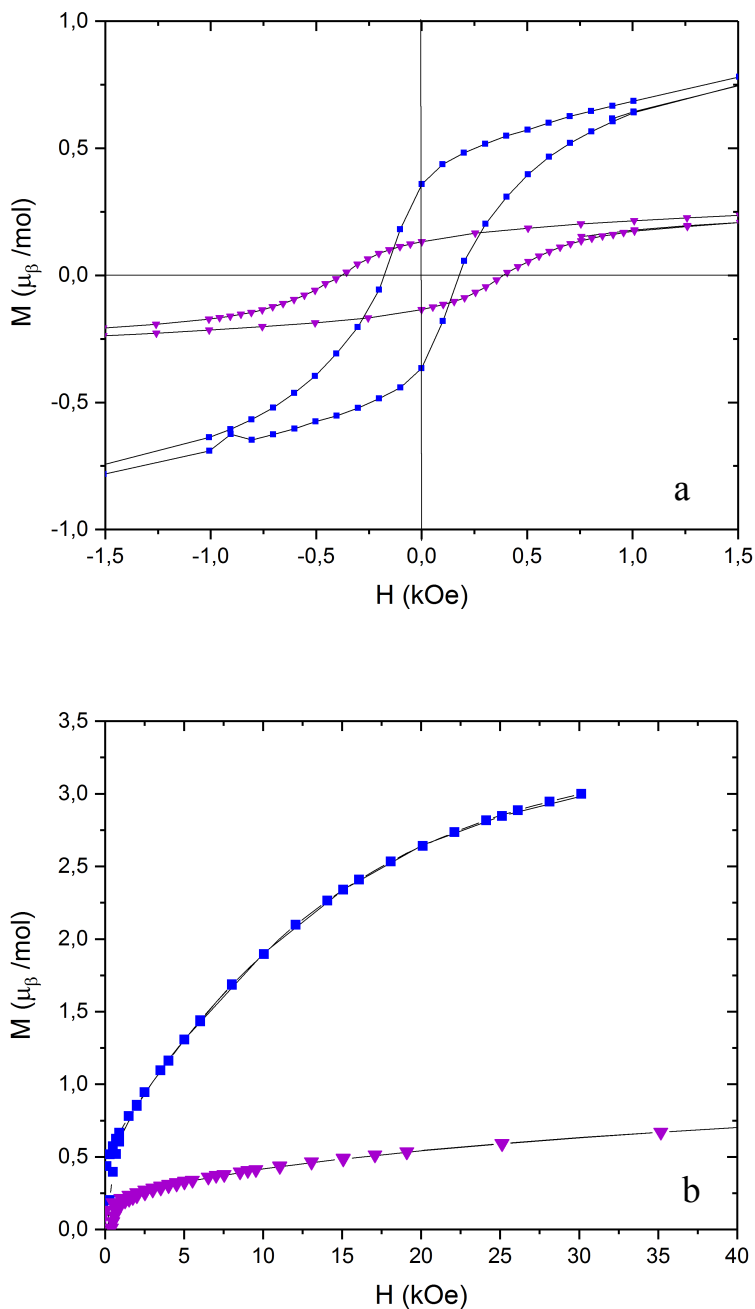
Figure 4.2.14. *Magnetization vs field up to 40k Oe (a) Hysteresis loops between -1,5 KOe to 1,5 KOe (b) at T=2K in compound **2** as prepared (blue) and **1** as prepared (purple).*

Optical activity

The UV-vis spectra for **2** in the solid state shows analogous bands to **1**, but relatively less intense (Figure 4.2.15a). The CD data confirms optical activity has been transferred to the magnetic network, showing specular images for each enantiomer in the visible region (Figure 4.2.15b). In this case the maxima/minima for each enantiomer appear at 300 and 550 nm.
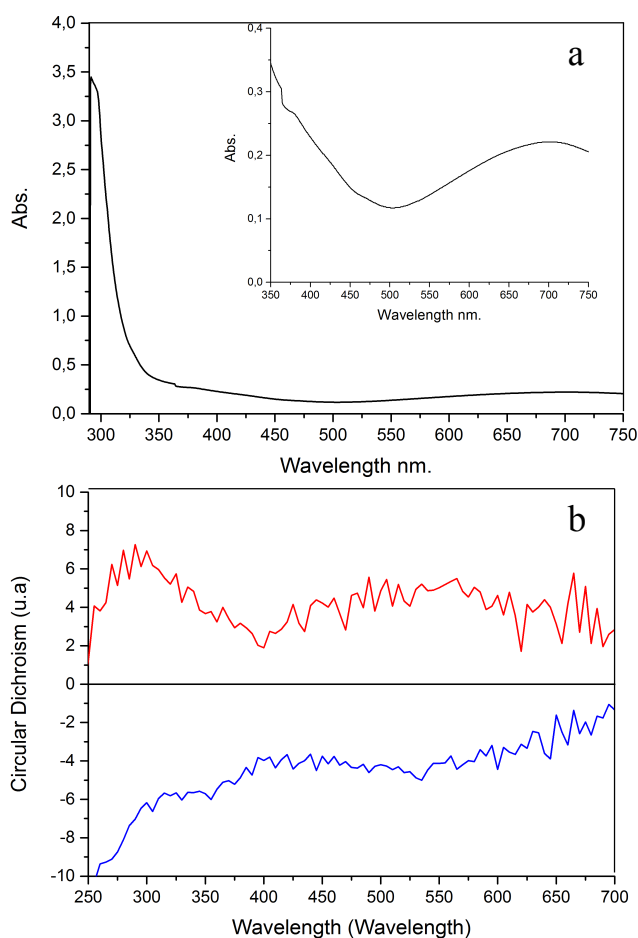
Figure 4.2.15 *Solid state UV-vis spectra (a) and circular dichroism (b) compound **2**: D enantiomer (red line), L enantiomer (blue line)*

Vibrational circular dichroism
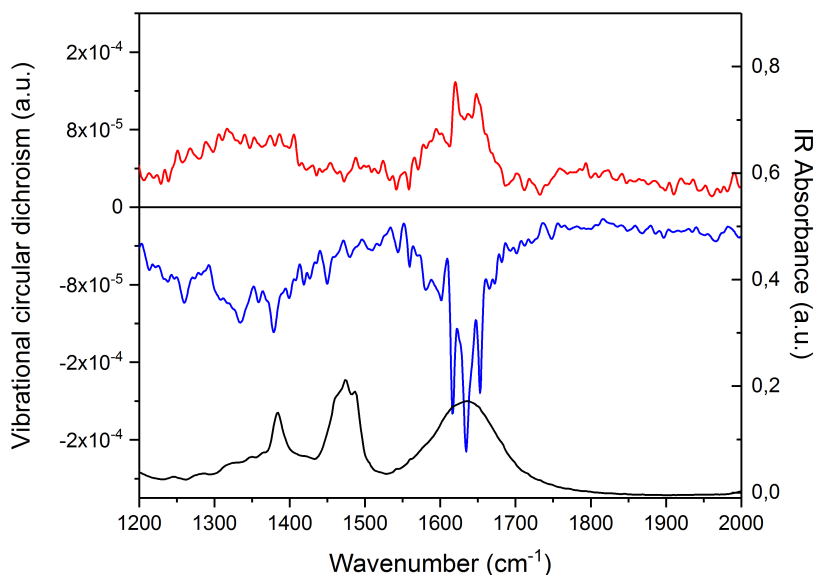
Figure 4.2.16 *VCD spectra of compound **2**: D enantiomer (red line), L enantiomer (blue line) at 1500 cm^{-1}. Infrared spectra of compound **2** (black line)*

In this case, looking for additional experimental evidence of the intrinsic chirality in this material, we also obtained CD data in the infrared region: the vibrational circular dichroism (VCD) spectra. UV-vis CD gives information about the electronic structure (electronic transitions, and charge-tranfer fenomena) whereas VCD provides direct information from molecular bonds[71]. Due to technical difficulties, and low intensity of the bands, we could only get successful VCD data in the 1200-2000 cm^{-1} (Figure 4.2.16). We found both enantiomers exhibit specular images, apparently composed by three signals, centered at 1640 cm^{-1}. This is the characteristic absorbance of the water bending frecuency. This demonstrates that even the non-chiral water molecules, present in the material as solvent, are showing optical activity and , thus, we can confirm this is a true genuine chiral magnet.

II.   Conclusions

To sum up briefly this section, we have been able to obtain a chiral magnet with very high ordering temperature, close to room temperature (265 K), optimizing the metal to chiral ligand (L-/D-proline) content during the synthesis to a 1:1 ratio. We demonstrated that incorporation of the chiral proline ligands transfers optical activity to the whole solid, even solvent molecules occupying the holes left in the structure by the coordination network. The presence of the ligand also confers higher redox stability to the material, that is not significantly oxidized in air for some days.

4.2.4. Vanadium/ proline "1:0.5" and "1:0.1"

How ligand ratio affects to chirality and magnetism?

In light of these results, we decided to reduce the proline content in our original synthesis. Our target was to further increase the ordering temperature of the material, and to determine the minimun ligand content at which chirality is transferred to the magnetic network.

I. Synthesis and characterization

Following the same procedure, VCl_2 was dispersed in enantiopure proline aqueous solutions in 1:0.5 and 1:0.1 ratios (compounds **3** and **4** respectively). Both compounds were precipitated by addition of an aqueous solution of TBA-$Cr(CN)_6$, purified by centrifugation, and washed with water and methanol. Unfortunately, we could not get complete analyses for these materials at the time of writing this thesis, so we cannot give the stoichiometry of these products.

Spectroscopic characterization of vanadium/proline "1:0.5" (3), "1:0.1" (4)

The IR spectra confirmed the presence of proline for both, **3** and **4**. The signature bands centered at 2963 and 2961 cm^{-1}, respectively, correspond to the hydrogen nitrogen stretching frequency (Figure 4.2.17)

Single symmetric v_{CN} stretching wide bands are observed between 2100-2140cm^{-1} (Figure 4.2.18), green and orange lines), that correspond to V^{II}-Cr^{III} pairs. For as prepared **3** and **4**, the absence of vanadyl groups is confirmed by the completely absence of $v_{v=o}$ bands.

After standing in air for 24 h, the v_{CN} stretching bands shifted to higher frequencies for both, 2173cm^{-1}, confirming that both compounds get oxidized in air to $V^{IV}O$/Cr^{III}. The vanadyl signature band is also intense (985-990 cm^{-1}),

appearing at higher frequencies than in compound **zero** (Table 4.2.1). In zero, the 2115 cm^{-1} band (V^{II}/Cr^{III}) does not disappear completely, indicating mix-valence character.

Table 4.2.1 *Sumary of main infrared peaks of all compounds synthesized.*

Compound	Proline/V Ratio*	$v_{(CN)}$ (cm^{-1}) Fresh-N$_2$	$v_{(CN)}$ (cm^{-1}) 24h-Air	$v_{(vo)}$ (cm^{-1}) Fresh-N$_2$	$v_{(vo)}$ (cm^{-1}) 24h-Air
Zero	**0**	2115	2113$_{(w)}$ 2166$_{(s)}$	940$_{(vw)}$	940$_{(w)}$
1	2	2162	2176	950$_{(vw)}$ 975$_{(vw)}$	950$_{(vw)}$ 975$_{(s)}$
2	1	2112$_{(w)}$ 2163$_{(s)}$	2172	-	970
3	0.5	2108$_{(w)}$ 2119$_{(s)}$	2173	-	985 950
4	0.1	2116	2173	-	990$_{(s)}$

*During synthesis.

In comparison with the proline-containing compounds presented previously (**1** and **2**, purple and blue lines respectably), **3** seems to have higher V^{II}/V^{IV} ratios, but only initially, before air exposition.
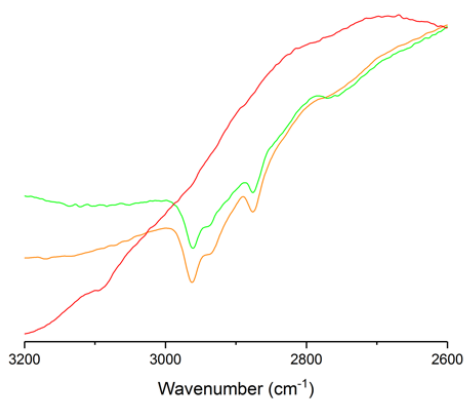
Figure 4.2.17 *Infrared spectra in H-N stretching region in proline for*
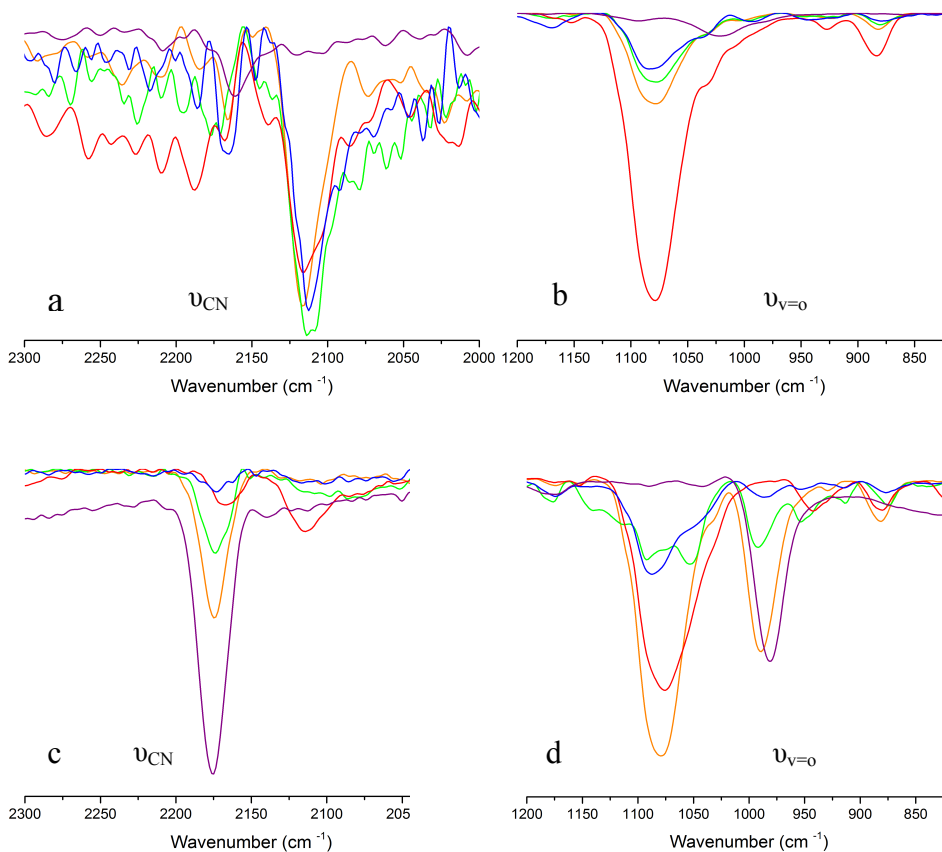
Figure 4.2.18 *FT-IR spectra of compounds **zero** (red), **2** (blue), **3** (green) and **4** (orange) as prepared (a,b) and 24h exposed to air (c,d) in υ_{CN} (a,c) and $\upsilon_{v=o}$ region (b,d)*

Magnetic properties

The magnetic behavior of **3** and **4** is almost identical. Both are magnetically ordered below 240 K. This critical temperature is in between that of **1** and **2**, suggesting that the 1:1 V/proline ratio is close to the optimum value, regarding T_C. Additionally, both materials are apparently less stable when exposed to air, with the corresponding T_C decreasing down to 90 and 70 K, respectively. This is in good agreement with the infrared data (Figure 4.2.18, b and d) indicates that most vanadium centers are oxidized to V^{IV}. Thus, the 1:1 ratio looks also appropriate regarding the extra-redox stability.

Table 4.2.2 *T_C values of compounds with different ligand concentrations*

Compound	Proline/V Ratio	T_c (K) Fresh-N_2	T_c (K) 48h-Air	Difference
Zero	0	260	120	140
1	2	135	30	105
2	1	270	240	30
3	0,5	240	90	150
4	0,1	240	70	170
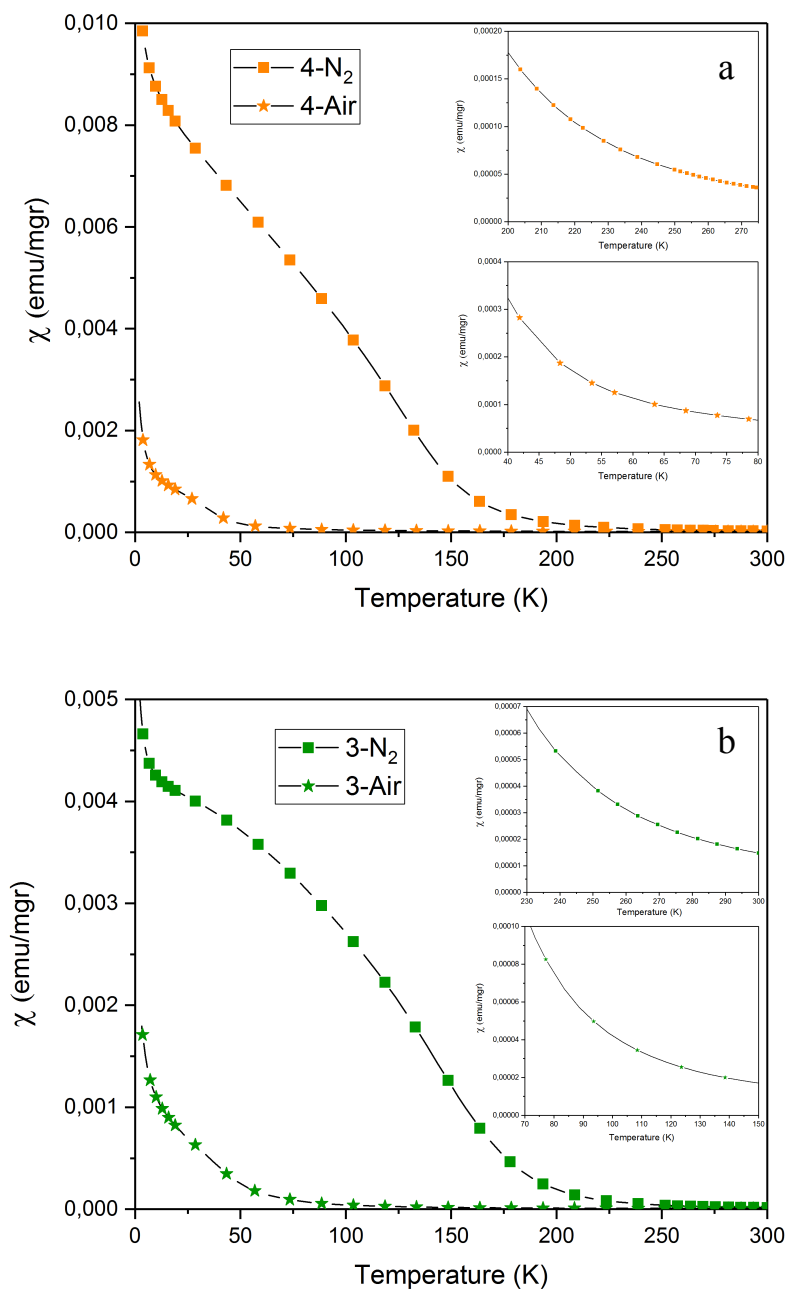
Figure 4.2.19 *Thermal dependence of magnetic susceptibility in field-cooled (FC) at 1000 Oe applied field (H) in **4** (a) and **3** (b) as prepared (square) and exposed to air (stars).*
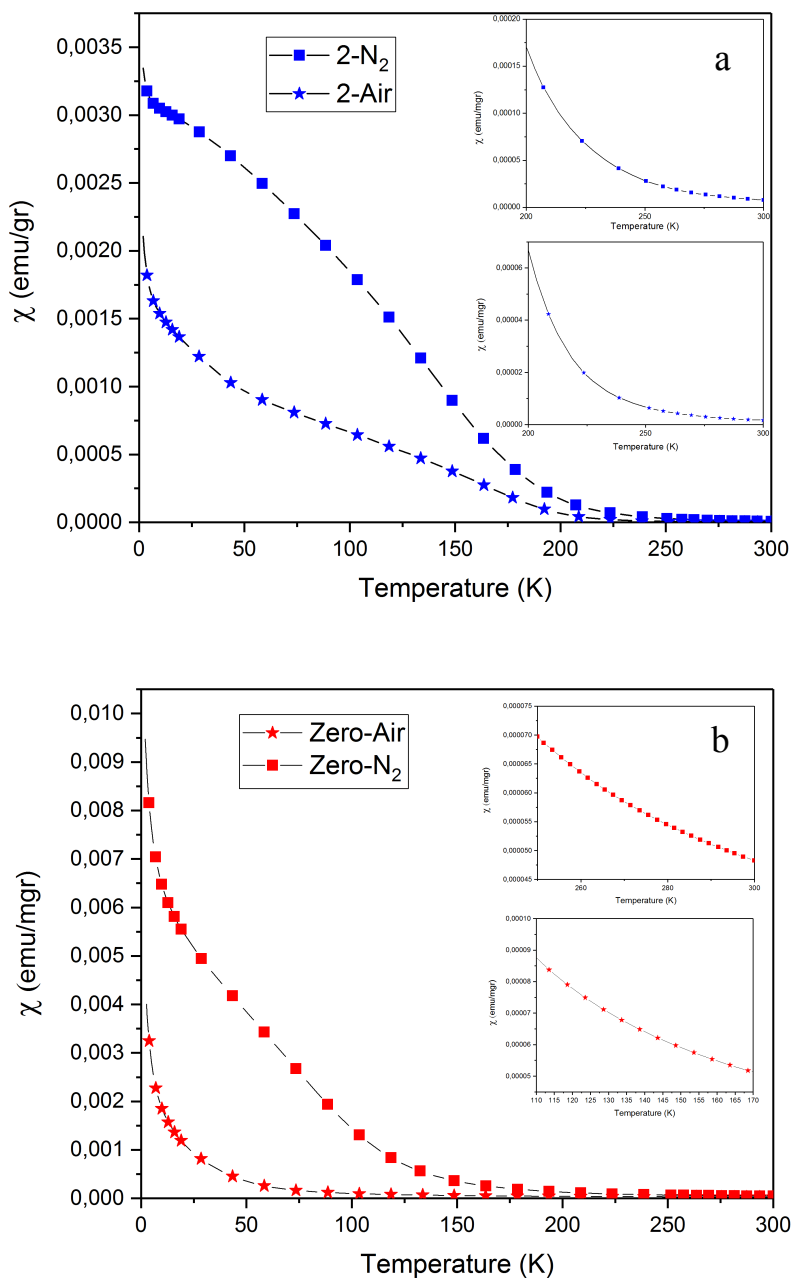
Figure 4.2.20 *Thermal dependence of magnetic susceptibility in field-cooled (FC) at 1000 Oe applied field (H) in **2** (a) and **3** (b) as prepared (square) and exposed to air (stars).*

Optical activity

No optical activity in UV-vis in solid was observed neither for **3** nor **4** (Figure 4.2.21). The CD spectra are almost flat, and the weak features that appear are not specula images for each enantiomer. So, we assign them to an artifact of the measurement. The absence of chirality in the visible region suggests that the proline content is too low in these cases to transfer chirality to the material, since the presence of proline was confirmed by infrared spectra and elemental analyses.
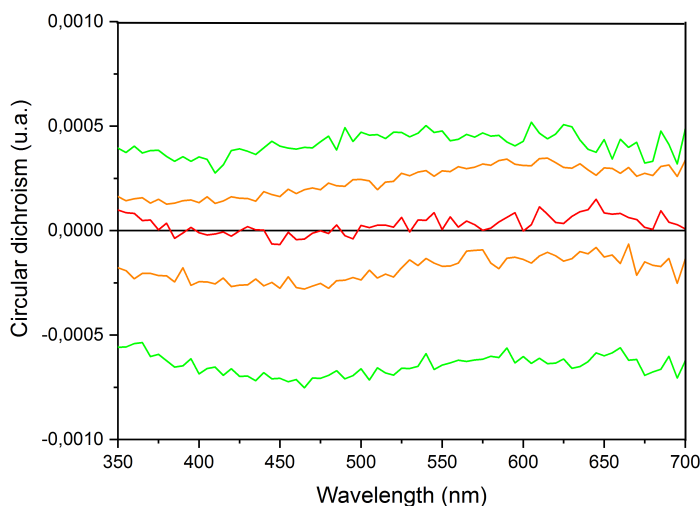
Figure 4.2.21 *Circular dichroism compound **3** (green), compound **4** (orange) and compound **zero** (red) for D enantiomers (up), L enantiomer (down). (Only one line, no isomers, for **zero** compound)*

4.3. <u>Conclusions</u>

In this chapter, we have presented our successful strategy to obtain chiral magnets based on the series of V/Cr cyanide-bridged materials. The key ingredient was the use of chelating chiral ligands with low basicity, allowing mildly acidic conditions. Introducing the natural amino acid proline in the synthesis of the V/Cr cyanide-bridged magnets, we obtained a series of chiral magnets, reaching the highest ordering temperature for the ratio V/proline/Cr 2:2:1. This chiral magnet exhibits a record-high critical temperature of 265K. Optical activity was confirmed by CD measurements in the UV-vis and IR range, confirming chirality is transferred from the ligand to the magnetic nertwork.

Furthermore, we found that the presence of proline increases the redox stability of this materials for 24h. It is remarkable that the transformation of V^{II}/V^{III} to vanadyl under air oxidation is partially avoided in compound **2**. After 24 h air exposure, its T_C decreases only down to 220 K. This is in contrast to the original V/Cr series, where the materials are oxidized to the corresponding vanadyl derivative in few hours. Therefore, introduction of chiral proline ligands did not only bring multifunctionality, but also higher stability. Both features could have important technological interest.

4.4. Experimental

4.4.1. Electrosyntesis.

Into a 100mL of 0.1M KCl solution reactants were added: 5mM $K_3Cr(CN)_6$, 5mM of 1,2-diaminocyclohexane and 5mM VCl_3. The pH was adjusted to 5.8 with HCl (0.1M). 30ml of this solution was transfer into a small electrochemistry glass and three electrodes were immerse in, Ag/AgCl (3,5M) as reference, Pt wire as a counter electrode and $1.5cm^2$ of FTO glass as a working electrode. Afterwards, glass was sealed and bubbled with nitrogen during 30 min. and -1,2V were later applied during 20 min.

4.4.2. Synthesis.

All reactions were done under inert atmosphere in to a nitrogen filled glove box. Reagents were obtained from commercial sources and used without further purification

TBA-Cr(CN)_6. was prepared keeping stirring overnight a solution of potassium hexacyanochromate (1M) and tetrabutylammonium chloride (TBA-Cl) (3,1M) in ethanol. Afterwards, yellow solution was filtered to remove KCl, and rotaevaporate the solvent to obtain a fine yellow powder.

I.   Compounds 1,2,3 and 4.

0,9 mmol of **VCl_2** was dispersed in a 5 ml of pure racemic proline aqueous solution (1,8 mmol) and left it stirring 20h . By that time, the initial green dispersion became a brown solution. Therefore, we followed the reaction by adding dropwise 5 mL of an aqueous solution of 0,3 mmol of **TBA-Cr(CN)_6**. Immediately, a deep blue precipitate formed (**1**). The solid was centrifugated and washed with water and methanol. **2**, **3** and **4** were prepared with same procedure but with 0,9, 0,45 and 0,09 mmol respectively.

Compound zero.

The same reaction with exactly the same procedure for compound **1** was carried out in absence of proline.

4.4.3. Characterization.

All magnetic measurements were done in a MPMS3 SQUID magnetometer by Quantum design.

Zero-field cool field cool measurements (ZFC-FC). To measure compounds in nitrogen, powder sample was secured to a gel capsule inside the glove box, sealed with kapton and inserted into a straw. This is later introduced into SQUID quickly, to keep the inert atmosphere. Sample was centered and started to measure. First we lowered the temperature from 300K to 2K without applying field. Once the temperature is stable, we apply the corresponding field and begin to lower the temperature to 2 K/min by recording the magnetization (**FC**). Once the ambient temperature is reached, same operation is carried out, but decreasing temperature to 1K/min (**ZFC**) up to 2K again. Finally, magnetic field is removed and temperature is increased up to room temperature (**RM**). Same measurements were done for samples exposed to air, without the necessity of inert atmosphere.

Hysteresis and magnetization curves sample preparation was the same than in the ZFC-FC measurements. Firstly temperature was set at 2K from 290K at 10K/min. Then we started to applied a magnetic field from 0 to 100 Oe in 25 Oe increment, from 200 to 1000 Oe in 100 Oe increments and then up to 30000 Oe in 1000 Oe increments. This first cicle is not take into account in hysteresis cycle, because it starts at 0 Oe field and do not carry relevant information. Afterwards, we move down the field from 30000 Oe to 5000 Oe in -5000 Oe increments, then down to 1000 Oe in -500 Oe, down to -1000 Oe in -100 Oe

increments to -10000 in -1000 Oe increments and down to -30000 Oe in -5000 Oe. Same pattern was followed from -30000 Oe up to 30000 Oe.

FT-IR spectra were taken of the compounds to avoid the oxidation as far as possible, the sample is transported in a sealed Eppendorf, the powder is placed on top of the ATR, and rapidly a piece of greasy glass was placed on top of the sample, so that, powder get surrounded by sealed grass. Meanwhile, the glass was pressed to remove the air as fast as possible and then take the spectrum.

Solid UV-vis spectra were recorded in a UV-Vis measurements were carried out on a Shimadzu UV-2401PC spectrophotometer equipped with a ISR-240A Integrating Sphere Attachment (Angle of incident light: 0°) in the 240 to 800 nm wavelength an a photomultiplier detector, double beam optics and D2 and W light sources.

Circular dichroism in solid state measurements were carried out on an Applied Photophysics Chirascan Circular Dichroism spectrometer equipped with a photomultiplier detector, dual polarising prism design monochromator, photo-elastic modulator (PEM) and 150W Xenon light source. A KBr pellet was place into an in-house made support to keep it perpendicular to light beam. Time per point: 0.5, bandwidth: 4nm.

Vibrational circular dichroism experiments were carry out with an external accessory PMA 50 has been specially developed for Polarization Modulation measurements coupled to a Bruker FT-IR spectrometer de sample was dilute and measured in KBr pellet in transmission mode.

4.5. <u>References</u>

[1] Fowler, M. *Recuperado el* **1997**, *23*, 2012.

[2] White, R.M. *Science*., **1985**, 229, 4807.

[3] www.futuremarketinsights.com/reports/magnetic-materials-market

[4] Jiles, D. *Introduction to Magnetism and Magnetic Materials*. CRC press: **2015**.

[5] Kreines, N.; Kholin, D.; Demokritov, S. *Low Temperature Physics* **2012**, *38*, 826.

[6] Martín, J. I.; Nogués, J.; Liu, K.; Vicent, J. L.; Schuller, I. K. *Journal of Magnetism and Magnetic Materials* **2003**, *256*, 449.

[7] Leslie-Pelecky, D. L.; Rieke, R. D. *Chemistry of Materials* **1996**, *8*, 1770.

[8] Jiles, D. C. *Acta Materialia* **2003**, *51*, 5907.

[9] Wang, X. F.; Zhang, Y.; Qiao, Y.; Chen, G. L. *Intermetallics* **2007**, *15*, 357.

[10] Zhang, K. B.; Fu, Z. Y.; Zhang, J. Y.; Shi, J.; Wang, W. M.; Wang, H.; Wang, Y. C.; Zhang, Q. J. *Journal of Alloys and Compounds* **2010**, *502*, 295.

[11] Zhang, Y.; Zuo, T.; Cheng, Y.; Liaw, P. K. **2013**, *3*, 1455.

[12] Lucas, M. S.; Mauger, L.; Muñoz, J. A.; Xiao, Y.; Sheets, A. O.; Semiatin, S. L.; Horwath, J.; Turgut, Z. *Journal of Applied Physics* **2011**, *109*, 07E307.

[13] Yang, X.; Zhou, Z.; Nan, T.; Gao, Y.; Yang, G. M.; Liu, M.; Sun, N. X. *Journal of Materials Chemistry C* **2016**, *4*, 234.

[14] Shen, Y.; Sun, J.; Li, L.; Yao, Y.; Zhou, C.; Su, R.; Yang, Y. *Journal of Materials Chemistry C* **2014**, *2*, 2545.

[15] Fusil, S.; Garcia, V.; Barthélémy, A.; Bibes, M. *Annual Review of Materials Research* **2014**, *44*, 91.

[16] Miller, J.S. and Epstein, A.J. *MRS Bulletin*., **2000,** *25*, 21.

[17] Ferrando-Soria, J.; Vallejo, J.; Castellano, M.; Martínez-Lillo, J.; Pardo, E.; Cano, J.; Castro, I.; Lloret, F.; Ruiz-García, R.; Julve, M. *Coordination Chemistry Reviews* **2017**, *339*, 17.

[18] Ortega, N.; Kumar, A.; Scott, J. F.; Katiyar, R. S. *Journal of Physics-Condensed Matter* **2015**, *27*.

[19] Rikken, G.; Raupach, E. *Nature* **1997**, *390*, 493.

[20] Anastasiadis, N. C.; Granadeiro, C. M.; Klouras, N.; Cunha-Silva, L.; Raptopoulou, C. P.; Psycharis, V.; Bekiari, V.; Balula, S. S.; Escuer, A.; Perlepes, S. P. *Inorg. Chem.* **2013**, *52*, 4145.

[21] Wang, X. Y.; Wang, L.; Wang, Z. M.; Su, G.; Gao, S. *Chemistry of Materials* **2005**, *17*, 6369.

[22] Coronado, E.; Galán- Mascarós, J. R.; Gómez- García, C. J.; Martínez- Agudo, J. M. *Advanced Materials* **1999**, *11*, 558.

[23] Coronado, E.; Galán-Mascarós, J.; Gómez-García, C.; Martínez-Agudo, J. *Inorganic chemistry* **2001**, *40*, 113.

[24] Miyasaka, H.; Takayama, K.; Saitoh, A.; Furukawa, S.; Yamashita, M.; Clerac, R. *Chemistry- a European Journal* **2010**, *16*, 3656.

[25] Gao, S.; Affronte, M. *Molecular Nanomagnets and Related Phenomena*. Springer: **2015**; Vol. *164*.

[26] Chaudhuri, P. *Coordination Chemistry Reviews* **2003**, *243*, 143.

[27] Ouellette, W.; Galan-Mascaros, J. R.; Dunbar, K. R.; Zubieta, J. *Inorganic Chemistry* **2006**, *45*, 1909.

[28] Rittenberg, D. K.; Sugiura, K.-i.; Sakata, Y.; Mikami, S.; Epstein, A. J.; Miller, J. S. *Advanced Materials* **2000**, *12*, 126.

[29] Buschmann, W. E.; Paulson, S. C.; Wynn, C. M.; Girtu, M. A.; Epstein, A. J.; White, H. S.; Miller, J. S. *Chemistry of Materials* **1998**, *10*, 1386.

[30] Griebler, W. D.; Babel, D. *ZEITSCHRIFT FUR NATURFORSCHUNG SECTION BA JOURNAL OF CHEMICAL SCIENCES* **1982**, *37*, 832.

[31] Entley, W. R.; Girolami, G. S. *Science* **1995**, *268*, 397.

[32] Mallah, T.; Thiébaut, S.; Verdaguer, M.; Veillet, P. *Science* **1993**, *262*, 1554.

[33] Buschmann, W. E.; Paulson, S. C.; Wynn, C. M.; Girtu, M. A.; Epstein, A. J.; White, H. S.; Miller, J. S. *Advanced Materials* **1997**, *9*, 645.

[34] Ferlay, S.; Mallah, T.; Ouahès, R.; Veillet, P.; Verdaguer, M. *Nature* **1995**, *378*, 701.

[35] Hatlevik, Ø.; Buschmann, W. E.; Zhang, J.; Manson, J. L.; Miller, J. S. *Advanced Materials* **1999**, *11*, 914.

[36] Coronado, E.; Galan-Mascaros, J. R.; Gomez-Garcia, C. J.; Laukhin, V. *Nature* **2000**, *408*, 447.

[37] Verdaguer, M.; Bleuzen, A.; Marvaud, V.; Vaissermann, J.; Seuleiman, M.; Desplanches, C.; Sciuller, A.; Train, C.; Garde, R.; Gelly, G. *Coordination Chemistry Reviews* **1999**, *190*, 1023.

[38] Garde, R.; Villain, F.; Verdaguer, M. *Journal of the American Chemical Society* **2002**, *124*, 10531.

[39] Ferlay, S.; Mallah, T.; Ouahe, R.; Veillet, P.; Verdaguer, M.; Curie, M. **1999**, 229.

[40] Hozumi, T.; Hashimoto, K.; Ohkoshi, S. *Journal of the American Chemical Society* **2005**, *127*, 3864.

[41] Koo, Y. S.; Galan-Mascaros, J. R. *Advanced Materials* **2014**, *26*, 6785.

[42] Darago, L. E.; Aubrey, M. L.; Yu, C. J.; Gonzalez, M. I.; Long, J. R. *Journal of the American Chemical Society* **2015**, *137*, 15703.

[43] Boldog, I.; Gaspar, A. B.; Martinez, V.; Pardo-Ibanez, P.; Ksenofontov, V.; Bhattacharjee, A.; Gutlich, P.; Real, J. A. *Angewandte Chemie-International Edition* **2008**, *47*, 6433.

[44] Day, P.; Kurmoo, M. *Journal of Materials Chemistry* **1997**, *7*, 1291.

[45] Ramshaw, B. J.; Sebastian, S. E.; McDonald, R. D.; Day, J.; Tan, B. S.; Zhu, Z.; Betts, J. B.; Liang, R. X.; Bonn, D. A.; Hardy, W. N.; Harrison, N. *Science* **2015**, *348*, 317.

[46] Uji, S.; Shinagawa, H.; Terashima, T.; Yakabe, T.; Terai, Y.; Tokumoto, M.; Kobayashi, A.; Tanaka, H.; Kobayashi, H. *Nature* **2001**, *410*, 908.

[47] Ojima, E.; Fujiwara, H.; Kato, K.; Kobayashi, H.; Tanaka, H.; Kobayashi, A.; Tokumoto, M.; Cassoux, P. *Journal of the American Chemical Society* **1999**, *121*, 5581.

[48] Galán-Mascarós, J. R.; Coronado, E.; Goddard, P. A.; Singleton, J.; Coldea, A. I.; Wallis, J. D.; Coles, S. J.; Alberola, A. *Journal of the American Chemical Society* **2010**, *132*, 9271.

[49] Rikken, G.; Raupach, E. *Nature* **1997**, *390*, 493.

[50] Train, C.; Gheorghe, R.; Krstic, V.; Chamoreau, L.-M.; Ovanesyan, N. S.; Rikken, G. L. J. A.; Gruselle, M.; Verdaguer, M. *Nat Mater* **2008**, *7*, 729.

[51] Bellouard, F.; Clemente- León, M.; Coronado, E.; Galán- Mascarós, J. R.; Gómez- García, C. J.; Romero, F.; Dunbar, K. R. *European Journal of Inorganic Chemistry* **2002**, *2002*, 1603.

[52] Langenberg, K. V.; Batten, S. R.; Berry, K. J.; Hockless, D. C.; Moubaraki, B.; Murray, K. S. *Inorganic Chemistry-Washington* **1997**, *36*, 5006.

[53] Berlinguette, C. P.; Vaughn, D.; Cañada- Vilalta, C.; Galán- Mascarós, J. R.; Dunbar, K. R. *Angewandte Chemie* **2003**, *115*, 1561.

[54] Colacio, E.; Dominguez-vera, J.-M.; Ghazi, M.; Kivekas, R.; Lloret, F.; Moreno, J.-M.; Stoeckli-evans, H. *Molecular Crystals and Liquid Crystals* **1999**, *335*, 283.

[55] Kou, H.-Z.; Zhou, B. C.; Gao, S.; Liao, D.-Z.; Wang, R.-J. *Inorganic chemistry* **2003**, *42*, 5604.

[56] Colacio, E.; Ghazi, M.; Stoeckli-Evans, H.; Lloret, F.; Moreno, J. M.; Pérez, C. *Inorganic chemistry* **2001**, *40*, 4876.

[57] Coronado, E.; Giménez- Saiz, C.; Nuez, A.; Sánchez, V.; Romero, F. M. *European Journal of Inorganic Chemistry* **2003**, *2003*, 4289.

[58] Shen, X.-P.; Gao, S.; Yin, G.; Yu, K.-B.; Xu, Z. *New journal of chemistry* **2004**, *28*, 996.

[59] El Fallah, M. S.; Rentschler, E.; Caneschi, A.; Sessoli, R.; Gatteschi, D. *Angewandte Chemie International Edition in English* **1996**, *35*, 1947.

[60] Ohba, M.; Ōkawa, H.; Fukita, N.; Hashimoto, Y. *Journal of the American Chemical Society* **1997**, *119*, 1011.

[61] Inoue, K.; Imai, H.; Ghalsasi, P. S.; Kikuchi, K.; Ohba, M.; Ōkawa, H.; Yakhmi, J. *Angewandte Chemie International Edition* **2001**, *40*, 4242.

[62] Coronado, E.; Gómez-García, C. J.; Nuez, A.; Romero, F. M.; Waerenborgh, J. C. *Chemistry of Materials* **2006**, *18*, 2670.

[63] Ohkoshi, S.-i.; Mizuno, M.; Hung, G.-j.; Hashimoto, K. *The Journal of Physical Chemistry B* **2000**, *104*, 9365.

[64] Coronado, E.; Makarewicz, M.; Prieto- Ruiz, J. P.; Prima- García, H.; Romero, F. M. *Advanced Materials* **2011**, *23*, 4323.

[65] Sato, O.; Iyoda, T.; Fujishima, a.; Hashimoto, K. *Science* **1996**, *271*, 49.

[66] Holt, D. G.; Larkworthy, L. F.; Povey, D. C.; Smith, G. W.; Leigh, G. J. *Inorganica chimica acta* **1990**, *169*, 201.

[67] Holmes, S. M.; Girolami, G. S. *Journal of the American Chemical Society* **1999**, *121*, 5593.

[68] Goberna-Ferrón, S.; Lillo, V.; Galán-Mascarós, J. R. *Catalysis Communications* **2012**, *23*, 30.

[69] Yasui, T. *Bulletin of the Chemical Society of Japan* **1965**, *38*, 1746.

[71] Duan, Y.; Han, L.; Zhang, J.; Asahina, S.; Huang, Z.; Shi, L.; Wang, B.; Cao, Y.; Yao, Y.; Ma, L. *Angewandte Chemie International Edition* **2015**, *54*, 15170.

Prussian blue coordination polymers as biocompatible multimodal contrast agent

Chapter 5

5.1   Introduction

Nowadays, tumor processes are one of the most common diseases in humans. Being cancer one of the most frequent causes of death in our societies[1]. Improving the diagnosis and motorization of the disease is essential for the well recovery and the quality of life of the patients, making image tests a key element for the early, fast and efficient diagnosis in tumor pathologies[2,3]. Among the most common medical imaging techniques are magnetic resonance imaging (MRI), X-ray imaging, ultrasound, radionuclide examination or computed tomography (CT). However, each technology has its own limitations, and on many occasions, it is difficult to clearly and accurately distinguish normal and ab-normal tissue. Hence, it have been wide developed hybrid or multimodal imaging techniques in the management of tumor diseases, in order to take advantage of the complementary advantages of the individual imaging modalities, and also, in the development of contrast agents for multimodal imagine[4,5]. Two of the techniques that are most interesting to combine, both for their complementarity and their frequency of use, are magnetic resonance imaging and computed tomography.

MRI is a non-invasive imaging technology with no radiation. It provides a range of information of the body, including anatomy, physiology and molecular information. This technique is based on excitation of hydrogen atom (single proton) in water molecules from human tissues, with a high intensity magnetic field producing a detectable signal that can be translate into images of the soft tissue. The two main issues of this technique are, on one hand, the difficulty in

seeing osseous tissues, due to the low water concentration, and, on the order hand, its low sensitivity, which is overcome with the use of contrast agents (CAs). The most common CAs are based on gadolinium complexes to enhance the imaging effect. Unfortunately, some surveys have shown Ga^{+3} could provoke adverse side reactions [6, 7], as nephrogenic systemic fibrosis (NFS)[8].

CT imaging is, in general, based on the attenuation of an X-ray beam that is transmitted differently through the body tissues to get an image from cuts or sections of anatomical objects for diagnostic purpose. In CT, X-rays must be blocked by some form of dense tissue to create an image, so the image quality in soft tissues will be poor. By using computer-processed combinations of many X-ray cross-sectional images is possible to get a complete image of the interior of an object without invasive procedures. Instead of obtaining a projection image, such as with conventional radiography, the CT computes multiple images from concerted rotational movements of the X-ray source and detector around the body. The final representation of the tomographic image is a complete tridimensional image. Remarkable biomedical engineering and technological advances in X-ray computed tomography, including manufacturing of recent generations of high-end multi-source multi-detector CT scanners for dual-energy computed tomographic (DECT) measurements, have been made in the past decades[9,10]. Development of X-ray contrast agents (XCAs), on the other hand, has been somewhat limited.

Conventionally, XCAs are small molecules containing iodine (Z = 53) for it exhibits high X-ray attenuation with its K-edge energy at 33 keV [11]. Iodine-containing compounds have shortcomings such as short

imaging time, high renal toxicity and allergic reactions [12, 13]. Only recently, other biocompatible XCAs, such as gold (Z = 79) and bismuth (Z = 83) nanoparticles (AuNP and BiNP, respectively), have been explored [14, 15, 16]. However, the gold and bismuth nano-XCAs are conventional metal or inorganic nanomaterials with offering few variations for adjustment and fine-tuning of their physical properties [19]. In terms of multimodal activity, they are not promising frameworks.

During this work, our aim was to enhance the X-ray CT contrast capabilities of nano-scale Prussian blue analogs, already promising contrast agents for MRI. These nanoscale coordination polymers are attractive candidates for multimodal molecular imaging, owning to their unique intrinsic physical and chemical properties [17,18]. Depending on their composition, several derivatives have shown contrast activity for several diagnostic techniques, including MRI [19], optical imaging [20], and photoacoustic imaging [28]. We note that application of these PBAs to X-ray computed tomography (CT) has not been studied, where these materials possess great potential. We rationalized that the nanoscale PBAs could also be attractive XCAs, particularly "soluble type" Prussian blue analogs $A^I_x M^{II}[M^{III}(CN)_6]_{(x+2)/3}$, the presence of alkali counter cations (A^I) with high X-ray attenuation factors. Indeed, PBAs are proven to sequestrate Cs^I atoms from solutions [21, 22, 23, 24]. The interstitial position of these cations does not alter the electronic properties of these materials, preserving their MRI activity. While their presence would enhance CT activity, promoting multimodal MRI/CT capabilities. Manganese iron based Prussian blue analogs are intriguing versatile materials with a wide range of applications. Due to their intrinsic biocompatibility, as well as low toxicity [25], these nanoscale coordination polymers have been successfully studied as biomedical

contrast agents for multiple imaging techniques, opening remarkable possibilities for the development of multimodal agents[26,27,28]

In this chapter, we demonstrate that manganese Prussian blue coordination polymers can be tailored to achieve enhanced X-ray contrast by incorporating heavy alkaline metal cations into their porous structures, while maintaining other intrinsic imaging possibilities, such as magnetic resonance and optical imaging.

5.2   Results and discusion

5.2.1. Synthesis and characterization of PB contrast agents.

Four Prussian blue analogs, namely, $K_{0.1}Mn[Co(CN)_6]_{0.67}$ (**1**), $K_{0.1}Mn[Fe(CN)_6]_{0.70}$ (**2**), $Rb_{0.5}Mn[Fe(CN)_6]_{0.84}$ (**3**), and $Cs_{1.2}Mn[Fe(CN)_6]_{0.93}$ (**4**) were prepared by direct synthesis from the precursor hexacyanoferrate or hexacyanocobaltate and $MnCl_2$ in a solution in excess of the desired alkali cation in water.

Metal stoichiometry was determined by microanalysis (EDX) (see experimental section 5.4.2). The same reaction conditions yielded materials with variable alkali cation contents, due to the higher affinity of larger alkalis to be trapped in the Prussian blue network. The alkali content increased according to the following tendency: $K^+ \approx 0.1 < Rb^+ \approx 0.5 < Cs^+ \approx 1.2$.

X-ray powder diffraction (Figure 5.2.1) confirmed the isostructural face center cubic structures (space group: $Fm\overline{3}m$) for PBAs **1-3**[29], as expected. **4** revealed a different pattern as expected for PBAs with heavy alkaline metal cations periodically inserted in the tetrahedral sites[30].
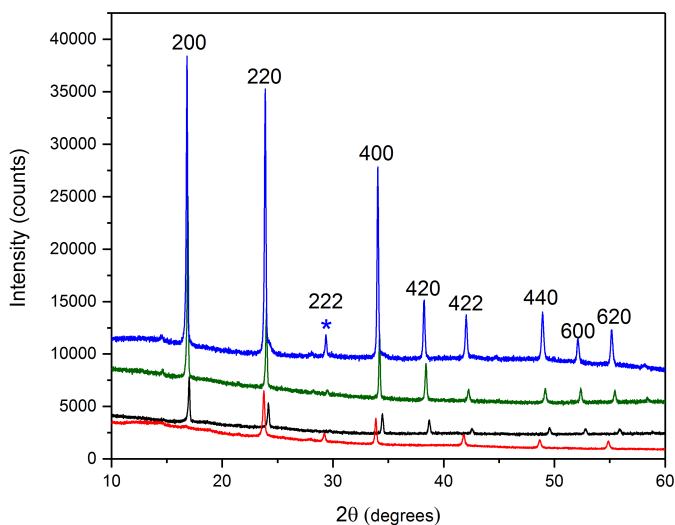
Figure 5.2.1 *X-ray diffraction pattern of compound **1** (black), **2** (green), **3** (blue) and **4** (red)*

All samples showed negative zeta potentials above 15 mV allowing for low aggregation in solution. Suspensions of these nanoparticles in water are relatively transparent. Particle size was measured by dynamic light scattering (DLS) analysis and confirmed by electron microscopy (Figure 5.2.2). Size distribution ranged from 479±100 nm (**2**) to 137±46 nm (**4**) (Table 5.2.1). Larger alkaline cations typically promote faster precipitation and smaller particles[31]. In agreement with this, **4** shows the smallest particles, containing the highest concentration of the largest alkaline. This was also confirmed by SEM images (Figure 5.2.2)

Table 5.2.1 *Z-potencial and particle diameter values for **1, 2, 3** and **4***

Compound	1	2	3	4
Z-potencial (mV)	-23.3	-19.2	-21.0	-15.6
Particle size (d.nm)	268±146	479±100	159±25	137±46
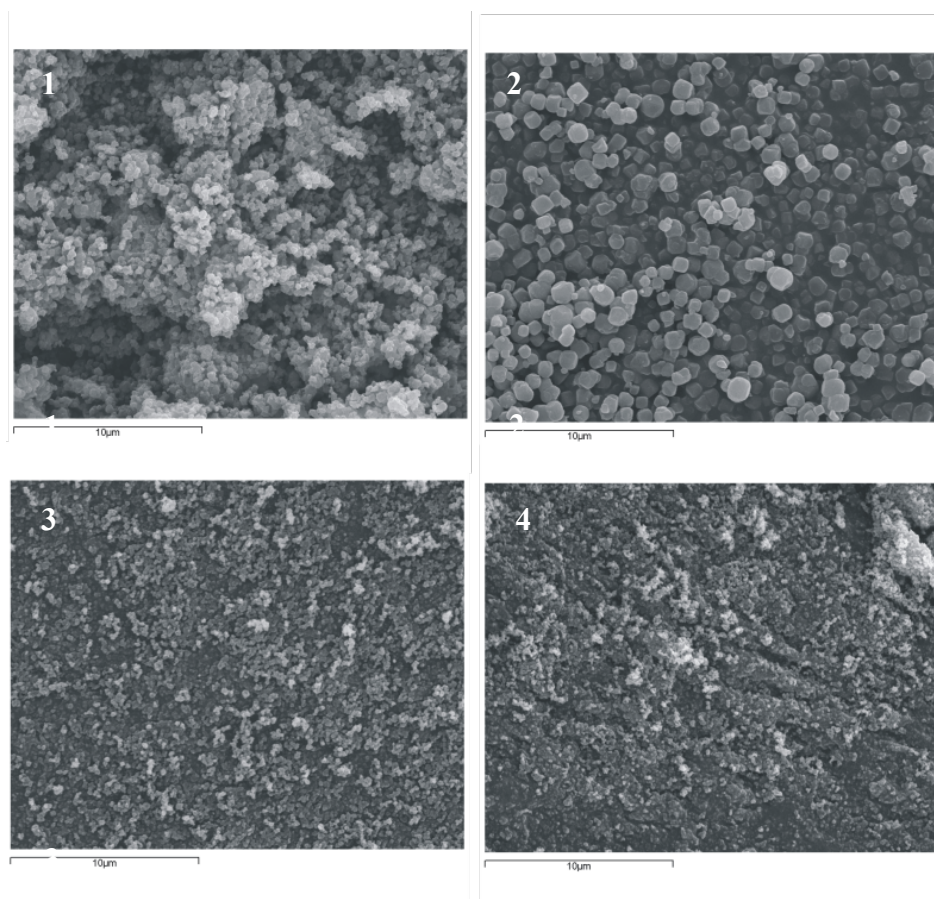
Figure 5.2.2 *SEM images of compounds **1** to **4***

FT-IR spectra (Figure 5.2.3) shows one CN stretching band at 2148-2152 cm^{-1} (strong) that can be assigned to the Fe^{III}-CN-Mn^{II}. As the alkali content increased, a second band appeared at 2075-2077 cm^{-1} (medium) corresponding to the Fe^{II}-CN-Mn^{II} pair, as previously reported for these non-stoichiometric materials[32]. This is due to the spontaneous reduction of the Fe^{III} centers, stabilized by the presence of the positive charges. Afterwards, attenuation experiments were done to evaluate the real capability of this material as X-ray CA.
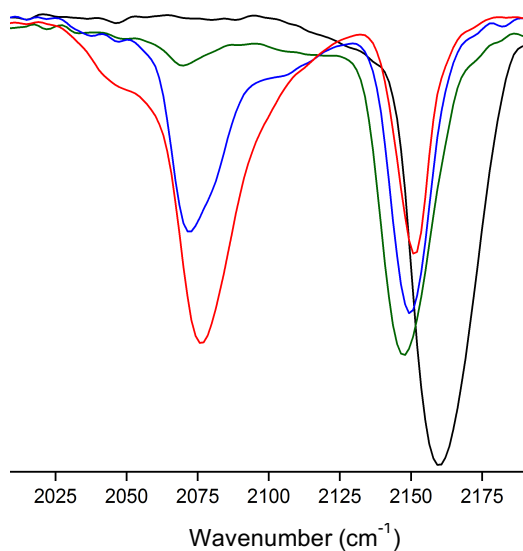
Figure 5.2.3 *FT-IR spectra of compound 1 (black), 2 (green), 3 (blue) and 4 (red)*

5.2.2. Imaging studies of PBAs as potential CT and Dual energy CT contrast agents.

First of all, we checked if the incorporation of heavy alkali metal cations in tha PBA structure resulted in enhanced X-ray attenuation. As reference molecule for x-ray attenuation, iohexol was used. It is one of the most extended iodine sources currently used as contrast agent in CT and x-ray related techniques[33].
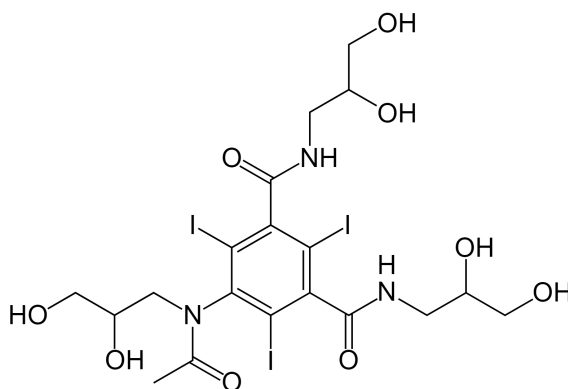
Figure 5.2.4. Iohexol molecule

1-4 were prepared as suspensions in agarose gel at various concentrations and X-ray attenuation measurements were performed. The attenuation rates in Hounsfield units per concentration unit (Hm/M) (See AnnexIII for further information) are summarized in Table 5.2.1. We also measured the dual energy ratio (DER)[*]. DER is an important parameter, in order to evaluate the relationship between voltage and attenuation coefficients.

---

[*] The dual-energy ratio (DER) denotes the ratio between the AC value at low X-ray voltage to the AC value at high X-ray voltage.

Our data clearly show that for MnHFe PBA attenuation increase with the atomic number of the alkali cation.

Table 5.2.1 *X-ray attenuation coeficients(AC) and dual energy (DE) ratios for Prussian blue analogs 1-4 and standar iohexol*

| X-CA | X-ray Tube voltage (kV) | | | | | |
| | 25 | | 30 | | 40 | |
	AC HU•mM^{-1}	DER	AC HU•mM^{-1}	DER	AC HU•mM^{-1}	DER
1	4.32	-	3.08	1.42	2.26	1.91
2	3.44	-	2.82	1.22	1.90	1.81
3	7.94	-	6.55	1.21	4.89	1.62
4	9.00	-	8.78	1.03	7.34	1.23
Iohexol	7.27		5.71	1.27	4.46	1.63

Plots of the X-ray attenuation as a function of concentrations at 40-kV scanning voltage revealed a linear relationship as expected (Figure 5.2.5), suggesting a direct dependence of X-ray attenuation on XCA concentrations.

Compared to iodine, **3** showed comparable attenuation coefficient while **4** exhibited substantially higher attenuation coefficient, especially at lower scanning X-ray tube voltages practically in-line with the corresponding mass attenuation coefficients reported for alkaline atoms[34] (Figure 5.2.6).
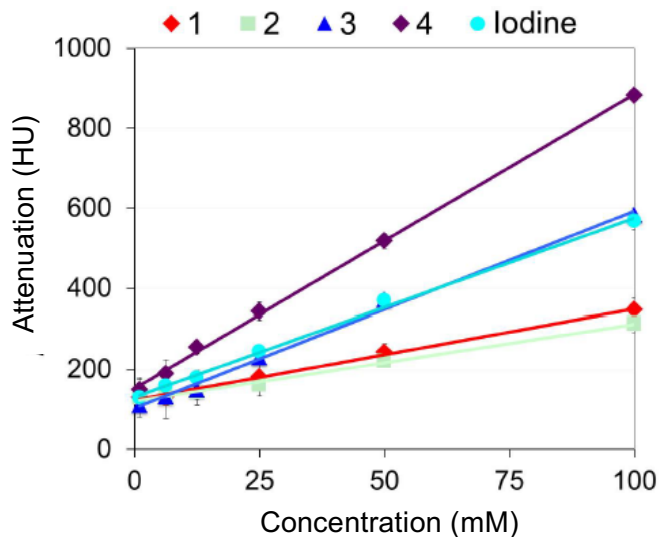
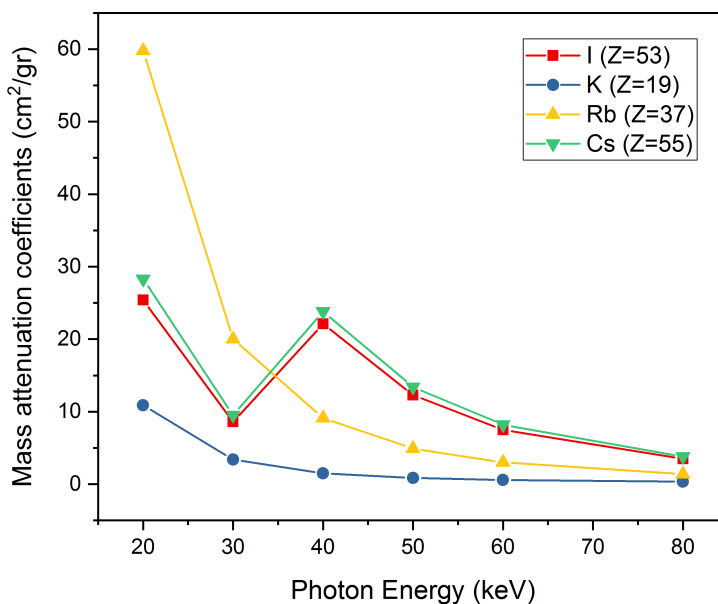***Figure 5.2.5*** *X-ray attenuation plot for iohexol and PBAs at 40kV*

Figure 5.2.6 *Mass attenuation coefficients for the elements I (Z=53)(red squares),K (Z=19) (blue dots), Rb (Z=37) (yellow triangles), and Cs (Z=55) as a function of photon energy (data from ref. 34)*

For instance, the attenuation rates for the opaquest PBA samples and the control at the 25-kV voltage are 7.94, 9.00, and 7.27 Hum/M for **3**, **4**, and iohexol, respectively. While studies performed by others suggested steady trends in attenuation for other metal containing XCAs, such as bismuth nanoparticles and ions[35], our measurements showed that the trends in attenuation coefficients increased as the X-ray tube voltages decreased, consistent with those for the iodine standards previously observed[36]. This suggests that the PBAs are potential candidates for dual-energy XCAs, since they exhibit varying opaqueness dependent upon X-ray tube voltages.

Systematically, our high-resolution X-ray CT scans revealed that the attenuation coefficients increased upon increasing occupation and atomic number of the alkali counter cations. For example, **4** which contained Cs^+ in 1.2 stoichiometry, exhibited the highest X-ray attenuation at all scanning X-ray tube voltages, followed by PBA **3**, with Rb^+ (at 0.5). PBAs **1** and **2**, containing just negligible amounts of K^+, only exhibited moderate X-ray attenuation. In this case, we associate this attenuation to the pure PBA structure, which is greatly enhanced by addition of Rb^+ or Cs^+.

We also noted that, although Rb has higher mass attenuation coefficients (Figure 5.2.6) when compared with Cs^+, the higher Cs^+ loading yields the highest attenuation values for **4**, implicating that the attenuation properties of this family of PBAs could be effectively modulated based on careful selection of the counter cation (A^I) as well as its content.

5.2.3. *Imaging studies of the PBAs as potential DECT-XCAs*

A previous report by Krissak and co-workers examined at the scanning X-ray tube voltages of 80, 100, 120, and 140 kV (applicable in clinical settings) for compact bone and muscle[37]. The corresponding DERs with the range of 1.20-1.45 and 1.01-1.08 for compact bone and muscle, respectively, were relatively constant. By comparing these DERs to those of gold and iodine XCAs, it was determined that the iodine XCA was a better DECT contrast for muscle due to a larger difference in their DERs than the gold XCA, which was a better DECT contrast for compact bone due to a similar reason.

We inspected the use of our nanoscale PBAs as potential candidates for DECT XCAs compared to iohexol. We used the aforementioned three scanning voltages and evaluated the attenuation ratios at two DER settings, namely at 25kV/30kV and 25kV/40kV (Table 5.2.1). Extrapolating these results to the X-ray tube voltages at which our scans were collected, we derived comparisons of their DER features (Table 5.2.2). Our results indicate that **3** would be a better XCA for muscle, akin to iohexol and the literature-reported iodine. PBA **4** would be a more suitable XCA for compact bone. This comparison also suggested that, depending on the presence of the alkali counter ions, these PBAs would indeed be versatile XCAs for different types of biological tissues and biomedical protocols.

Table 5.2.3 *X-ray attenuation (µ) and dual-energy ratios for various tissue samples.*

| Tissue | X-ray tube voltage (kV) | | | | | |
| | 25 | | 30 | | 40 | |
	AT[†](HU)	DER	AT (HU)	DER (20kV/30kV)	AT (HU)	DER (20kV/40kV)
Muscle	7.37×10^1	-	6.66×10^1	1.11	6.19×10^1	1.19
Soft tissue	7.37×10^1	-	6.86×10^1	1.12	6.32×10^1	1.22
Bone	7.37×10^3	-	5.21×10^3	1.47	3.35×10^3	2.29

5.2.4. In vitro biological studies of the PBAs as potential XCAs.

We evaluated *in vitro* imaging of the glioblastoma U87-Luc. Glioblastoma is the most aggressive cancer that begins within the brain. The name gioblastoma was given because it grows in glia cells. Glia cells are non-neuronal cells that maintain homeostasis, form myelin, and provide support and protection for neurons in the central and peripheral nervous systems. Glioblastoma U87-Luc are a specific cancer cells used as a standard, amongst other reason, because its DNA sequence is well known[38]. In this experiments cells labeled with PBAs **1-4**, using X-ray micro-CT to demonstrate the cancer cells labeling with the nanoscale coordination polymers have enhanced contrast.

Figure 5.2.7a shows the *µ*-CT images of the cells treated with and without PBAs scanned at 25 kV. X-ray CT images of the collected cells showed considerable contrasts for PBAs **1**, **3**, and **4**, compared to the

---

[†] The x-ray attenuation in HU were calculate based on the mass attenuation coefficients (µ/ρ) from: http://physics.nist.gov/PhysRefData/XrayMassCoef/tab4.html

control in which the cells were not treated with the nanoscale coordination polymers.
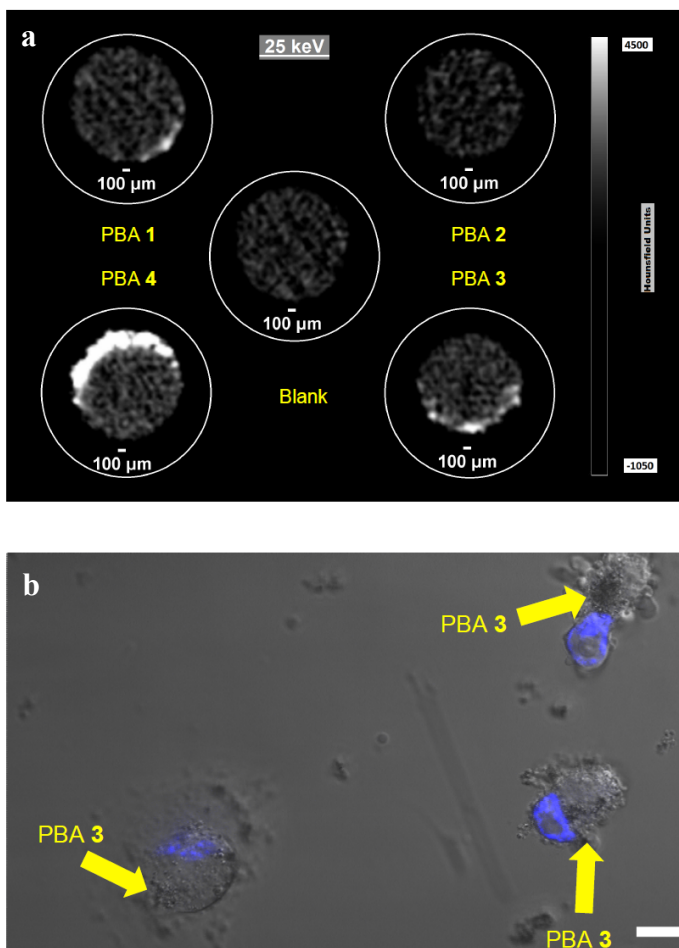
Figure 5.2.7 *Uptake of Prussian blue XCAs by U87-Luc studied by μCT imaging technique. U87-Luc cells were treated with PBAs **1**, **2**, **3**, and **4** for 24 h, after which the cells were detached, washed, and analyzed by the μCT scanner. Blank images correspond to those of cells without PBA treatment. (a) μCT images of PBAs **1**, **2**, **3**, and 4 scanned at 25 keV and 5-μm resolution. (b) Transmitted microscopic image with the 10-μm scale bar showing uptake and internalization of PBA **3** in U87-Luc cells. The blue areas are nuclei stained with the nuclear dye Hoechst 33342. Uptake of Prussian blue XCAs by U87-Luc studied by μCT imaging technique.*

As expected, based on the phantom studies, the cells labeled with PBA **3** and **4** exhibited the highest enhanced contrast, particularly at lower scanning X-ray tube voltages (25 and 30 kV). Internalization of PBAs **1-4** were also studied in U87-Luc cells by transmitted microscopy as demonstrated by the corresponding bright-field image of the U87-Luc treated with **3** (Figure 5.2.7a). The arrows in Figure 5.2.7b indicated the location of **3** and the blue domains designated the nuclei stained with Hoechst 33342. These images obtained from transmitted microscopy are in-line with the in vitro μ-CT images, suggesting cell labeling of the U87-Luc cells with PBAs and their potential cellular uptake.

We also carried out *in vitro* viability assays on U87-Luc cells treated with various PBA concentrations (up to $3.0\times10\text{-}3$ M in Mn^{2+} concentration). These assays revealed that all PBAs were relatively non-toxic compared to the clinically approved anticancer drug irinotecan (Figure 5.28) which yielded the viability of less than 50% at all concentrations studied (Figure 5.2.9).
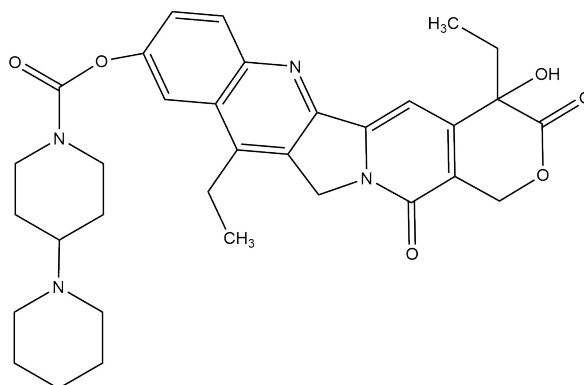
Figure 5.2.8 *Irinotecan molecule*
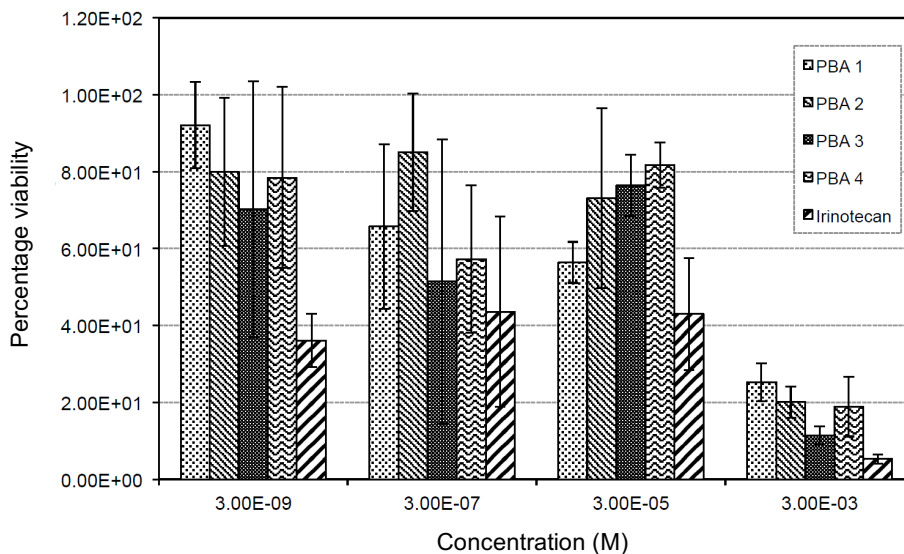
Figure 5.2.9 *Percent viability assays of the glioblastoma U87-Luc after 24h treatment with PBA and anti-cancer irinotecan measured by bioluminescence technique.*

The cytotoxic effect on U87-Luc cells became drastically apparent with the cell viability below 30% only at concentration higher than 30 mM for all PBAs with PBA **1** being the least toxic. These results suggested that the PBAs were essentially biocompatible with the U87-Luc cells.

5.3 <u>Conclusions</u>

We showcased a new class of XCAs based on the nanoscale mixed-valence Prussian blue coordination polymers that were prepared with different interstitial alkali metal ions. By varying the alkali metal ions (K^+, Rb^+, and Cs^+) and their chemical composition ratio present in each PBA, we were able to demonstrate that selected PBAs, containing the high-atomic number alkali metals Rb or Cs, exhibited comparable attenuation rates to those of clinically used iohexol, if not higher. Similar observations were made with these PBAs for in vitro μ-CT studies using the glioblastoma U87-Luc cells. In addition, all PBAs studied at various scanning X-ray tube voltages for the dual-energy CT technique gave significant variations in their DER values, making them potentially applicable as DECT XCAs. Cell viability assays of U87-Luc cells treated with PBAs conveyed their biocompatibility up to 30 µM. For the first time, we demonstrated that the manganese PBAs could be designed and prepared as potential XCAs for preclinical μ-CT as well as DECT.

We anticipate that this work would provide a foundation for further development of PBAs as true multimodal contrast agents since their MRI activity is still present due to the paramagnetic nature of their constituent metal centers (Mn and Fe).

5.4   Experimental

5.4.1. Synthesis

1. **K$_{0.1}$Mn[Co(CN)$_6$]$_{0.67}$**

This compound was prepared by mixing an aqueous solution of MnCl$_2$ (0,1M) and with another solution of K$_3$Co(CN)$_6$ (0,1M). The reaction mixture was keeping under stirring for 1h. Finally, the compound was separate from de solution by centrifugation, washing the powder three times with 30 mL of water.

2. **K$_{0.1}$Mn [Fe (CN) $_6$]$_{0.7}$**

This compound was prepared by mixing an aqueous solution of MnCl$_2$ (0.1M) with another solution of K$_3$Fe(CN)$_6$ (0.1M). The reaction mixture was keeping stirring for 1h. Finally, the compound was separate from de solution by centrifugation, washing the powder three times with 30 mL of water.

3. **Cs$_{1.2}$Mn [Fe (CN) $_6$]$_{0.93}$**

This compound was prepared by mixing an aqueous solution of MnCl$_2$ (0,3M) and CsCl (1M) with another solution of K$_3$Fe(CN)$_6$ (0,1M) and CsCl (1M).

The reaction mixture was keeping stirring for 1h. Finally, the compound was separate from de solution by filtering, washing the powder with 120 mL of water.

4. **$Rb_{0.5}Mn [Fe (CN)_6]_{0.84}$**

This compound was prepared by mixing a very cold (solution on ice) aqueous solution of $MnCl_2$ (0,1M) with another cold solution of $K_3Fe(CN)_6$ (0,1M). The reaction mixture was keeping stirring for 1h. Finally, the compound was separate from de solution by centrifugation, washing the powder three times with 30 mL of water.

5.4.2. Characterization

Size distribution and zeta potentials were determined by dynamic light scattering with a NanoSZ (Malvern). Measurements were done in a 1mgr/ml water dispersion.

Scanning electron microscopy was carried out with a JEOL-JMS6400 environmental scanning electron microscope.

Energy dispersive X-ray spectroscopy was used to analyze metal content of PBA with scanning electron microscope JEOL-JMS400 equipped with an Oxford EDX analyzer (Oxford Instruments).

Table 5.4.1 Elemental abundance for the constituent atoms of the compounds 1, 2, 3 and 4 as prepared, estimated for the EDX analysis.

% Atomic	1	2	3	4
Cation	4.5 (K^+)	5.6 (K^+)	21.9 (Rb^+)	37.7 (Cs^+)
Mn	54.9	54.7	42.4	31.9
Fe	-	39.7	35.7	29.1
Co	37.2	-	-	-

Infrared spectroctroscopy data were collected in the 3600-600 cm-1 range with Bruker Optics FTIR Alpha spectrometer equipped with Attenuated Total Reflectance (ATR) sample holder.

Powder X-ray diffraction data were collected on a D8 Advanced series $2\theta/\theta$ powder diffractometer at room temperature in transmission mode or in Bragg-Brentano configuration using a PANAlytical X'pert diffractometer, equipped with a hybrid monochromator, operating with CuKα radiation ($\lambda = 1.541$ Å).

X-ray attenuation measurements were performed using a single-slice or whole-volume quantification with high-resolution volumetric scanning method in suspension at various concentration of 1-4 n 2.5% agarose gel (1.00, 6.25, 12.50, 25.00, 50.00, and 100.00 mM)

High resolution X-ray μCT image of iohexol and PBAs suspended in 2.5% agarose phantoms at 25kV. Blank does not contain any contrats agent.

Micro-computed tomography, imaging measurement and analysis: _Phantom studies_.

Solutions of five samples (iohexol and PBAs 1-4) with six different concentrations (1.00, 6.25, 12.5, 25.0, 50.0 and 100 mM) each were prepared in triplicates in 0.5-mL microcentrifuge tubes. The tubes were mounted vertically on a 45-mm stage in diameter filled at the bottom with a 5-mm layer of clay. Each scan included a set of 5 samples of the same concentration, oriented radially with a blank tube positioned at the center of the stage. A wood handle was also placed between two of the samples to serve as a reference point. All scans

were set for acquisition at 140 mA with varying X-ray tube voltages (25 kV, 30 kV, 40 kV).

All samples were scanned with SkyScan 1172 micro-CT scanner (Bruker Corporation) at standard resolution of 26.74 μm/pixel, with an image matrix of 100 × 575 pixels. No filters were used, the angular position of acquisition was set at 1° rotational steps, and an average of 2 frames were taken at each angular position. The field of view was increased horizontally with the offset camera mode to encompass all of the tubes within each scan. Post-processing was completed with Bruker software NRecon for reconstruction and CT-Analyser for quantification. The hounsfield unit (HU) scale (-1050 to 4500) was chosen with regards to the histogram displaying the data dynamic range calculated by NRecon before reconstruction. The top and lower ends of the scale were chosen around the region of the peak and tail ends of the histogram. All data were reconstructed and analyzed within this dynamic range. The attenuation value resulted from the mean brightness intensity calculated from this HU scale. The total reconstructed output was 600 slices per tube. The volume of interest was further narrowed down for quantification to the middle 201 slices, with each slice of interest being the exact middle slice of the VOI.

Micro-computed tomography (μ-CT) imaging measurement and analysis: *In-vitro studies*

The U87-Luc cells, well studied in our laboratory and chosen as the model cell line in this study, were dispersed in culture media and treated with 1-4 (25 mg/mL) at 37 °C for 24h. The cells were incubated in an 8-well culture plate at 37°C for 24h, after which their viability

assays were evaluated using the bioluminescence technique in triplicate. Quantification of the bioluminescence signals from the cells treated with PBAs could be correlated to cell viability[39].

The glioblastoma U87-Luc cells were treated with PBAs **1-4** for 24 h. The samples containing U87-Luc treated with PBAs **1-4** in centrifuge tubes were mounted vertically onto a styrofoam platform. All acquisitions and reconstruction parameters were similar to those previously described in the phantom studies. The cells were washed thoroughly after treatment and collected by centrifugation in 0.5-mL centrifuge tubes. The quantification region was selected from the bottom 151 slices of the stack starting from the first bottom slice that showed signals, and each slice of interest is the middle slice of their respective stacks.

5.5 <u>References</u>

[1]Organization, W. H. *Cancer Control: A Global Snapshot in 2015*; 2015; p 6.

[2] Weissleder, R. *Science* **2006**, *312*, 1168.

[3] Weissleder, R.; Pittet, M. J. *Nature* **2008**, *452*, 580.

[4] Townsend, D. W. *Journal of Nuclear Medicine* **2008**, *49*, 938.

[5] Judenhofer, M. S.; Wehrl, H. F.; Newport, D. F.; Catana, C.; Siegel, S. B.; Becker, M.; Thielscher, A.; Kneilling, M.; Lichy, M. P.; Eichner, M. *Nature medicine* **2008**, *14*, 459.

[6] Scarabelli, S.; Cripps, P.; Rioja, E.; Alderson, B. *Vet. Anaesth. Analg.* **2016**, *43*, 502.

[7] Idée, J. M.; Port, M.; Raynal, I.; Schaefer, M.; Le Greneur, S.; Corot, C. *Fundamental & clinical pharmacology* **2006**, *20*, 563.

[8] Stratta, P.; Canavese, C.; Aime, S. *Curr. Med. Chem.* **2008**, *15*, 1229.

[9] Li, H.; Zhang, H.; Tang, Z.; Hu, G. *Progress in natural science* **2008**, *18*, 513.

[10] Chen, H.; Rogalski, M. M.; Anker, J. N. *Physical Chemistry Chemical Physics* **2012**, *14*, 13469.

[11] http://physics.nist.gov/PhysRefData/XrayMassCoef/ElemTab/z53.html

[12] Katayama, H.; Yamaguchi, K.; Kozuka, T.; Takashima, T.; Seez, P.; Matsuura, K. *Radiology* **1990**, *175*, 621.

[13] Caschera, L.; Lazzara, A.; Piergallini, L.; Ricci, D.; Tuscano, B.; Vanzulli, A. *Pharmacological Research* **2016**, *110*, 65.

[14] Mieszawska, A. J.; Mulder, W. J.; Fayad, Z. A.; Cormode, D. P. *Molecular pharmaceutics* **2013**, *10*, 831.

[15] Brown, A. L.; Naha, P. C.; Benavides-Montes, V.; Litt, H. I.; Goforth, A. M.; Cormode, D. P. *Chem. Mat.* **2014**, *26*, 2266.

[16] Perera, V. S.; Hao, J.; Gao, M.; Gough, M.; Zavalij, P. Y.; Flask, C.; Basilion, J. P.; Huang, S. D. *Inorganic chemistry* **2011**, *50*, 7910.

[17] Dumont, M. F.; Risset, O. N.; Knowles, E. S.; Yamamoto, T.; Pajerowski, D. M.; Meisel, M. W.; Talham, D. R. *Inorganic Chemistry* **2013**, *52*, 4494.

[18] Dumont, M. F.; Yadavilli, S.; Sze, R.; Nazarian, J.; Fernandes, R. *International journal of nanomedicine* **2014**, *9*.

[19] Shokouhimehr, M.; Soehnlen, E. S.; Hao, J.; Griswold, M.; Flask, C.; Fan, X.; Basilion, J. P.; Basu, S.; Huang, S. D. *J. Mater. Chem.* **2010**, *20*, 5251.

[20] Huang, Y.; Hu, L.; Zhang, T.; Zhong, H.; Zhou, J.; Liu, Z.; Wang, H.; Guo, Z.; Chen, Q. *Scientific reports* **2013**, *3*, 2647.

[21] Kitajima, A.; Tanaka, H.; Minami, N.; Yoshino, K.; Kawamoto, T. *Chemistry Letters* **2012**, *41*, 1473.

[22] Ding, D.; Zhao, Y.; Yang, S.; Shi, W.; Zhang, Z.; Lei, Z.; Yang, Y. *Water research* **2013**, *47*, 2563.

[23] Delchet, C.; Tokarev, A.; Dumail, X.; Toquer, G.; Barré, Y.; Guari, Y.; Guerin, C.; Larionova, J.; Grandjean, A. *RSC Advances* **2012**, *2*, 5707.

[24] Torad, N. L.; Hu, M.; Imura, M.; Naito, M.; Yamauchi, Y. *J. Mater. Chem.* **2012**, *22*, 18261.

[25] Department of Health and Human Services. *FPL for approved NDA-21-626,* Approval letter. U.S. Food and Drugs Administration**,** (2003)

[26] Shokouhimehr, M.; Soehnlen, E. S.; Hao, J.; Griswold, M.; Flask, C.; Fan, X.; Basilion, J. P.; Basu, S.; Huang, S. D. *J. Mater. Chem.* **2010**, *20*, 5251.

[27] Huang, Y.; Hu, L.; Zhang, T.; Zhong, H.; Zhou, J.; Liu, Z.; Wang, H.; Guo, Z.; Chen, Q. *Scientific reports* **2013**, *3*, 2647.

[28] Liang, X.; Deng, Z.; Jing, L.; Li, X.; Dai, Z.; Li, C.; Huang, M. *Chemical communications (Cambridge, England)* **2013**, *49*, 11029.

[29] Tokoro, H.; Ohkoshi, S.-i. *Applied Physics Letters* **2008**, *93*, 021906.

[30] Matsuda, T.; Kim, J.; Moritomo, Y. *Dalton Transactions* **2012**, *41*, 7620.

[31] Catala, L.; Mallah, T. *Coordination Chemistry Reviews* **2017**.

[32] Ohkoshi, S. I.; Saito, S.; Matsuda, T.; Nuida, T.; Tokoro, H. *Journal of Physical Chemistry C* **2008**, *112*, 13095.

[33] http://apps.who.int/medicinedocs/documents/s16879e/s16879e.pdf

[35] Brown, A. L.; Naha, P. C.; Benavides-Montes, V.; Litt, H. I.; Goforth, A. M.; Cormode, D. P. *Chem. Mat.* **2014**, *26*, 2266.

[36] Kandanapitiye, M. S.; Gao, M.; Molter, J.; Flask, C. A.; Huang, S. D. *Inorganic chemistry* **2014**, *53*, 10189.

[37] Krissak, R.; Elgert, M.; Kusch, B.; Hünerbein, R. *Advances in Molecular Imaging* **2013**, *3*, 37.

[38] Clark, M. J.; Homer, N.; O'Connor, B. D.; Chen, Z.; Eskin, A.; Lee, H.; Merriman, B.; Nelson, S. F. *PLOS Genetics* **2010**, *6*, e1000832.

[39] Blumenfeld, C. M.; Sadtler, B. F.; Fernandez, G. E.; Dara, L.; Nguyen, C.; Alonso-Valenteen, F.; Medina-Kauwe, L.; Moats, R. A.; Lewis, N. S.; Grubbs, R. H. *Journal of inorganic biochemistry* **2014**, *140*, 39.

Annexes

Annex I

Tafel equation and tafel plots.

Tafel equation governs the irreversible behavior of an electrode. Considering the general mechanism of electron transfer to an electrode[*]:

$$O + ne^- \leftrightarrow R \qquad\qquad \text{(Eq. An I.1)}$$

Where O is oxidized and R is reduced species present in equilibrium and stable in the solution

The equilibrium for an electrode reaction is characterized by the Nerst equation, which relates the electrode potential to the bulk concentrations of the components:

$$E = E^o + \frac{RT}{nF} \ln \left. C_o^* \middle/ C_R^* \right. \qquad\qquad \text{(Eq. An I.2)}$$

· C_o^* and C_R^* are O and R concentrations respectively[†].
· E^o is the formal potential.
· **R** is the universal gas constant (8.3144472 J/K mol).
· **T** is the absolute temperature (K).
· **F** is the faraday constant ($9.64853399 \times 10^{-4}$ C/mol).
· **n** is the number of electrons involve in the electrode reaction.

The equilibrium mentioned above is dynamic. Although no net current flows across the electrodes the electrodes, both reduction and oxidation takes place

---

[*] Bard, A. J.; Faulkner, L. R.; Leddy, J.; Zoski, C. G. *Electrochemical Methods: Fundamentals and Applications*. Wiley New York: 1980; Vol. 2.

[†] both very low

at equal rate, so that the composition of the electrolyte does not change. The exchange current density, i_o is defined as dynamic flow of electrons or charge in both directions per unit area when an electrode reaction is at equilibrium.

Following butler-voltmer equation:

$$i = i_o exp \frac{(\alpha n F \eta_A)}{RT} + exp \frac{(-\alpha n F \eta_C)}{RT}$$
(Eq. An I.3)

- $\cdot$ **η** is the overpotencial, is the difference between the potencial at equilibrium and that applied by the driving power source.
- $\cdot$ **α** is the charge transfer barrier (symmetry coefficient)

The previous form of Butler-Volmer equation is valid when the electrode reaction is controlled by electrical charge transfer at the electrode (and not by the mass transfer to or from the electrode surface from or to the bulk electrolyte). This is for a well-stirred solution or with currents so low that the surface concentrations do not differ appreciably from the bulk values.

By applying a high positive overpotencial the anodic current density increase whaile cathodic current density becomes negligible. Therefore, the second term in Eq. An I.3 becomes negligible. The equation can be written as:

$$i = i_o exp \frac{(\alpha n F \eta)}{RT}$$
(Eq. An I.4)

$$log i = log i_o + \frac{(\alpha n F \eta_C)}{2.303 RT}$$
(Eq. An I.5.)

The lattes is called the **anodic Tafel ecuation**.

In the same way at the negative overpotentials, cathodic current density is much higher than anodic and so that anodic current density becomes negligible:

$$logi = logi_o - \frac{(\alpha nF\eta_C)}{2.303RT}$$ (Eq. An I.6)

This ecuation is called cathodic Tafel equation.

The usual form to write tafel´s ecuation is $\eta = a + b \, logi$ where:

$$b = \frac{2.303RT}{\alpha nF}$$ (Eq. AnI.7)

$$a = -\frac{2.303RT}{\alpha nF} \log i_o$$ (Eq. AnI.8)

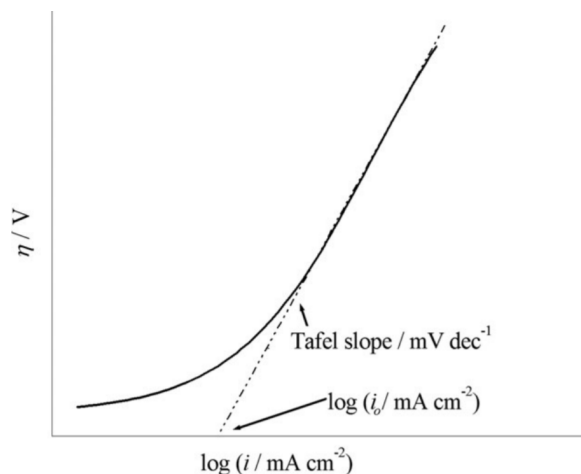Log i values are plotted against overpotencial to get Tafel plot (figure AnI.1).

Figure AnI.1 *A typical Tafel plot for an electrode reaction, from which exchenge current density and tafel slope ca be determined. Ref ‡*

While $\mathbf{i_o}$ is useful parameters for comparing different catalyst, an electrode material must possess a high $\mathbf{i_o}$ in addition to low Tafel slope (so high I at low over potentials) in order to be useful at the operational current densities required for a given energy storage application. Virtually any current can be obtained with any catalyst material is a sufficiently large electrode is used. For this reason, usually current densities are normalize to geometric surface area. Even with this normalization, the performance of a catalyst is enhanced by using a high surface area substrates or catalyst.

The Tafel slope, $\boldsymbol{b}$ (mV/decade) is an important experimental parameter commonly used to probe the mechanism of an electrode reaction and

---

‡ Zhao, F.; Slade, R. C.; Varcoe, J. R. *Chemical Society Reviews* **2009**, *38*, 1926.

identify the rate-determining step of the overall reaction. In electrochemical water oxidation it has been reported that[§,**]

---

§ Gerken, J. B.; McAlpin, J. G.; Chen, J. Y.; Rigsby, M. L.; Casey, W. H.; Britt, R. D.; Stahl, S. S. *Journal of the American Chemical Society* **2011**, *133*, 14431.

** Surendranath, Y.; Kanan, M. W.; Nocera, D. G. *Journal of the American Chemical Society* **2010**, *132*, 16501.

Annex II

Structural Data: Scherrer equation

$$\tau = \frac{K\lambda}{\beta cos\theta}$$
(Eq. An II.1)

· **τ** is the mean size of the ordered (crystalline) domains, which may be smaller or equal to the grain size.

· **K** is a dimensionless shape factor, with a value close to unity. The shape factor has a typical value of about 0.9, but varies with the actual shape of the crystallite.

· **λ** is the X-ray wavelength.

· **β** is the line broadening at half the maximum intensity (FWHM), after subtracting the instrumental line broadening, in radians. This quantity is also sometimes denoted as Δ (2θ)

· **θ** is the Bragg angle (in degrees).

Cell parameter equation for face cubic structure

$$a = \frac{\sqrt{h^2+k^2+l^2}}{\frac{\lambda}{2sin\theta}}$$
(Eq. An II.2)

Annex III

Dual-energy computed tomography (DECT)

Is a relatively new imaging technique to enhance visualization of different organ systems, relying upon the difference between the dual energy ratios (DER) of the materials exposed to the X-ray beams determined by the separation of the high- and low-energy spectra given in Eq. AnIII.1.

$$DE_{ratio} = \frac{HU_{low_{kV}}}{HU_{high_{kV}}} \qquad \text{(Eq. An III.1)}$$

Hounsfield unit (HU) is the result of the transformation of the scale of X-ray linear attenuation coefficients into a new scale in which the attenuation value of the distilled water in Normal Conditions of Pressure and Temperature (CNPT) is defined as 0 units of Hounsfield (HU), while the air radiodensity in CNPT is defined as -1000 HU, extending beyond the 1000 HUs assigned to the absorption rate of the compact bone, it is calculate according with the following equation:

$$H = \frac{1000(\mu - \mu_{water})}{(\mu_{water} - \mu_{air})} \qquad \text{(Eq. An III.2)}$$